Visualization and Analysis of Nanoscale Microstructure Evolution of *In situ* Metal Matrix Composites

by

Aaron Gladstein

A dissertation submitted in partial fulfillment
of the requirements for the degree of
Doctor of Philosophy
(Materials Science and Engineering)
in the University of Michigan
2022

Doctoral Committee:

Professor Alan Taub, Chair
Professor John Allison
Professor Bart Bartlett
Professor Ashwin Shahani

Aaron T. Gladstein

gladaaro@umich.edu

ORCID iD: 0000-0002-4625-6824

DEDICATION

This dissertation is dedicated to all the people who have supported me along my educational journey. Thank you for sticking with me all this time and lifting me so I could see the forest for the trees.

ACKNOWLEDGEMENTS

I am extremely grateful for all who helped me through my PhD program, there are so many who offered support, gave me advice, picked me up when I was down, and helped guide my research and progress as a scientist. I would like to start by thanking my advisor Professor Alan Taub and my nearly co-advisor Professor Ashwin Shahani; the two of you approach both research and mentorship in a similar manner and have shaped both the way I approach research and continued to inspire enthusiasm for probing into deeper scientific questions. You were forever interested in jumping into new research directions without faltering, and were always supportive through the highs and lows of research. Your guidance, encouragement, and support were imperative to me finishing this degree and I am eternally thankful for your patience and for seeing me as an individual and including me in your research labs. I would also like to thank my other committee members, Professor Bart Bartlett and Professor John Allison. Thank you for your insight, critical feedback, and guidance throughout this research.

I am extremely thankful to all of the staff and scientists at the University of Michigan that were integral for the smooth operations of so much of my work and so many others. Thank you to the Department of Materials Science staff: Keith McIntyre, Dr. Tim Chambers, Ying Qi, Dr. Sahar Farjami, Kevin Worth, Chris Cristian, Debbie Johnson, Renee Hilgendorf, Shelley Fellers, and Patti Vogel, Lourdes Jorgensen. I could not have finished my degree without your advice, training, equipment trouble-shooting, materials ordering, and so much more. I am happy to say as of writing this dissertation I have not broken any of Keith's rules for using the band saw. It was a pleasure getting to know all of you and I wish you the best in the future

Thank you to the Michigan Center of Materials Characterization staff – Bobby Kerns, Dr. Allen Hunter, Dr. Nancy Muyanja, Dr. Haiping Sun, Dr. Kai Sun, and Deanna Wendel, and Dr. Tao Ma – for your expertise, patience, and assistance with materials preparation and characterization, and for giving me the opportunity to use and enjoy some of the coolest equipment I have ever known.

I am grateful for the help from multiple national lab beam line scientists. Thank you to Dr. Vincent De Andrade, Dr. Francesco De Carlo and Pavel Shevchenko at the Advanced Photon Source at Argonne National Laboratory, and to Dr. Xianghui Xiao and Dr. Wah-Keat Lee at the National Synchrotron Light Source II at Brookhaven National Lab. Your assistance and expertise were critical for my synchrotron X-ray experiments found in this dissertation.

Thank you to the many, many collaborators and research professionals who I had the privilege of working with throughout my time at the University of Michigan. Dave Weiss at Eck Industries, Steve Udvardy at NADCA, Dr. Anil Sachdev at General Motors, and Dr. Andrew Bobel at General Motors you brought an incredible amount of metallurgical knowledge, industrial common sense, and were so helpful during our collaborative calls. Steve I would like to thank you in particular for showing what an industrial aluminum casting plant looks like and giving me the chance to run experiments at in your lab. I would also like to thank our many academic collaborators and colleagues at different universities – Professor Alan Lou at the University of Ohio, Professor Xun Liu at the Ohio State University and a Taub lab alum, Professor Xiaochun Li at the University of California Los Angeles, Professor Brajendra Mishra at Worcester Polytechnic Institute, and all of your fantastic post-docs and graduate students – your thoughtful discussions, varied perspectives, and expertise brought my research into otherwise unachievable heights. Thank you as well to Michael Moodispaw, Dr. Jiashi Miao, Dr.

Jianyue Zhang, and Dr. Renhai Shi from Professor Lou's group for your expertise and allowing me to run a few experiments in your lab.

I am also thankful to a number of groups at the University of Michigan who allowed me to use their equipment and offered me support and academic discussion. From the Materials Science and Engineering Department I want to thank Professor John Allison's research lab group and in particular Dr. Tracy Berman; Professor Ferdinand Poudeu's lab group and in particular Dr. Juan Lopez and Yixuan Chen, and Yiqiao Huang; Professor Richard Laine's lab group, including Dr. Jun Guan; Professor Amit Misra's lab group, in particular Dr. Mohsen Taheri, Dr. Bibhu Sahu, Dr. Ben Derby, Dr. Huai-Hsun (Burt) Lien, and Dr. Max Powers. All of your friendship, readiness to help, and offers to train and use your lab's equipment made graduate school far more interesting and more bearable than it otherwise would have been.

Thank you as well to Professor Adam Matzger's lab group in the Chemistry and Macromolecular Science and Engineering departments, including Michael Bellas and Dr. Derek Frank. Thank you to Professor Andrew Boehman in the Mechanical Engineering department for letting me use your TGA-DSC for so long, and thank you to Dr. Fengchao Liu in the Naval Architecture and Marine Engineering department for assisting with the friction stir processing experiments found in this dissertation.

I am extremely grateful to the members of Professor Ashwin Shahani's lab: Dr. Saman Moniri, Dr. Ning Lu, Insung Han, and special thanks to Jiwoong Kang, Yeqing Wang, Geordie Lindemann, Paul Chao, and Dr. Shanmukha Kiran. Your collaboration, help with coding and in particular data reconstruction and image processing, sample preparation tips, and friendship were invaluable. I look forward to our next tricycle ride at the beamline, although I can do without another COVID scare.

Thank you so much to the members of the Taub group, I am indebted to how great you made my graduate school experience. I am so impressed by the comradery and warm environment you all maintain and have never once regretted joining the group. Thank you to everyone I had the pleasure of working with, including Dr. Caleb Reese, Dr. Avi Bregman, Dr. Maya Nath, Dr. Wesley Chapkin, Dr. Yipeng He, Dr. Xun Liu, Randy Cheng, Anshul Singhal, Daney Zhang, Kanat Anurakparadorn, Anita Luong, Amy Langhorst, and Jonathan Goettsch. I am especially thankful to the metals group for your helpful insight, experimental tips and assistance, and commiseration, Caleb and Jon you two were particularly pivotal to my success, thank you so much. Randy, its because of you I joined the group so I guess a lot of this is your fault.

I want to give a special thank you to Professor C.B. Carter, Professor Harold Brody, and Professor Seok-woo Lee at my undergraduate institution, the University of Connecticut. You all believed in me for so long and encouraged my academic pursuit into graduate school. I will always be grateful for your presence in my life.

I would like to acknowledge financial support from the National Science Foundation (award # 1762657), the University of Michigan, and the Lightweight Innovations for Tomorrow (LIFT) institute.

To my friends both locally and located around the world, you have been fantastic and so supportive. I'm so lucky to have such a wide range of friends to lean on and laugh with. Thank you as well to all who served with me on the MSE Graduate Student Council, your leadership and care always impressed and inspired me. Special thanks to the University of Michigan Hillel and its staff, you brought me community, warm food, and helped fund a variety of Jewish activities and holidays I hosted.

To my family, including my siblings: Mindy, Scott, Zeke, David, Mark, Benjamin; my parents: Eric, Michelle, Alison, and Ed; and to all the extended members of the Gladstein, Bodian, Demarest, Brisman, and Perreault clans, thank you for your patience, advice, infinite well of encouragement and love. You always gave me broader perspective and helped me work through the many challenges throughout my academic career and life in general.

Most importantly, I am so immensely grateful and thankful to my amazing fiancé Rebecca. I still can't believe you followed me out to Michigan, accepted the fact I got a pet snake, and pushed us to get a puppy. You are my number one friend, and source for love, inspiration, and wisdom. Without you I never would have known to flour the blueberries. Thank you for sticking with me through all the hard times and celebrating the good times. You made graduate school, and life, more manageable. I would not be where I am without you. I am so happy to have you in my life, I love you so much and am excited for our wedding and the next chapter of our lives together.

Table of Contents

LIST OF TABLES

LIST OF FIGURES

ABSTRACT

Creating new, light-weight materials is a critical engineering problem required to meet the ever-increasing demands for improved fuel economy and electric vehicle range in the automotive, aerospace, and defense industries. Aluminum and its alloys have gained increased usage due to their high strength-to-weight ratio, low cost, and machinability. However, Al alloys suffer from poor thermal stability of mechanical properties, thus limiting their usage for components that operate in elevated temperatures. Therefore, there is much interest in methods for improving mechanical performance of Al-based materials at both ambient and elevated temperatures to expand the use of lightweight materials into new applications. One possible solution to this problem is the use of Al-based metal matrix nanocomposites (MMNCs), a mixture of aluminum and nanoscale reinforcement, as they have improved mechanical properties at both ambient and elevated temperatures over base Al alloys, without sacrificing the lightweight benefits of Al.

MMNCs are typically made via *ex situ* processing, where pre-manufactured reinforcing particles are incorporated into the Al matrix. These routes of MMNC production have a few main issues including the cost of the reinforcing nanopowders, reinforcement contamination, and undesirable particle-matrix interface reactions, which make particle incorporation and large-scale processing difficult. In contrast, *in situ* MMNC processing methods generate particles directly in the melt via a reaction between precursors and have shown improved particle-matrix interface stability and easier particle incorporation with the matrix. However, there is much work to be

done to reliably control key particle characteristics, such as particle size, dispersion, and volume fraction, when creating *in situ* MMNCs.

The research for this dissertation is focused on studying of the formation mechanisms of particles and controlling the resulting microstructure of *in situ* MMNCs. In this work we explore the processing-microstructure-properties relationships for two *in situ* processing methods, metal-based polymer pyrolysis (MBPP) and salt-flux reaction synthesis (SFRS), used to generate Al-based MMNCs. We find that there are multiple commercially available precursor polymers that can be used for generating MMNCs via MBPP and study their thermal degradation behavior to inform the best processing parameters for MMNC production. We report on successful MBPP processing to generate Al powder-based MMNCs that show improved mechanical properties. The results of the MBPP experiments demonstrate it as a potential method for *in situ* MMNC production.

We find that SFSR is a facile technique for generating Al/TiC MMNCs that has the possibility of scaling into industrial production. We use 2D and 3D microstructural analysis techniques to perform a detailed investigation of the MMNCs generated *via* SFRS and investigate the formation mechanisms of reinforcing TiC particles and intermetallic Al_3Ti. We find that the TiC particles are formed first and directly by the SFRS reaction, not through an indirect reaction using Al_3Ti, and that their presence in the melt affects the intermetallic morphology in multiple modes. We also investigate the effect of increasing Si content in the Al matrix on the microstructure and properties of the MMNCs. We find that Si affects the microstructure in multiple ways, changing both the intermetallics and the carbides which form, and discuss possible methods which its presence causes these changes. Our analysis and results

will assist in forming a more rational approach to processing *in situ* SFRS MMNCs and is an important step towards scaling up *in situ* processing methods.

CHAPTER 1
Introduction

1.1 Motivation

Creating new, light-weight materials is a critical engineering problem required to meet the ever-increasing demands for improved electric vehicle range and fuel economy in the automotive, aerospace, and defense industries. Lightweighting is an automotive term that describes the process of using lighter materials in production, such as carbon fiber, plastics, or light metals, to reduce total product weight and therefore improve fuel efficiency and handling. To do so without sacrificing the safety and functionality of the final product requires the use of materials with high strength-to-weight ratios [1]. The trend towards lightweighting has led to an increased use of and interest in aluminum alloys due to their high strength-to-weight ratio, low cost, machinability, and ability to be work- or precipitation-hardened [2-5]. However, Al alloys suffer from poor thermal stability of mechanical properties, thus limiting their usage for components that operate in elevated temperatures (e.g. automotive engine blocks can be made out of Al but require iron cylinder sleeves, and Al turbochargers have to operate at lower temperatures thereby reducing efficiency). Therefore, there is much interest for improving the mechanical performance of Al-based materials at both ambient and elevated temperatures, in order to increase its applicability through multiple sectors.

There are many ways to increase the mechanical properties of Al including solid solution strengthening [6], precipitation hardening [7], work hardening [8], and intermetallic strengthening [9]. While each of these has their benefits, they also have their downsides. Work

hardening increases mechanical strength by increasing the dislocation density at the expense of material ductility. Precipitation hardening, also called age hardening, strengthens materials through the generation of nanoscale precipitates (e.g. Guinier-Preston zones in Al-Cu alloys) via specific heat treatments, but if done incorrectly the material can be over-aged and the precipitates can coarsen in elevated temperature applications, both of which lead to inferior properties [10, 11]. Another strengthening approach involves the incorporation of hard reinforcing nanoparticles (10^{-9} m), often ceramics, into the metal matrix thus creating metal matrix nanocomposites (MMNCs). MMNCs are attractive due to their ability to leverage the high strength and stiffness of the ceramic reinforcement particles, while still retaining the ductility of the metal matrix at low volume percentages of reinforcement, thereby overall improving mechanical properties [2, 3, 5, 12-15]. Due to the chemical and thermal inertness of the ceramic reinforcement at elevated temperatures (e.g. 200 – 350 °C), their inclusion in the MMNCs offers the potential of improving mechanical properties at elevated temperatures, making them ideal materials for applications requiring high temperature operation [10, 12, 15-22]. Therefore, Al-based MMNCs have the promise of being a low-weight and high-strength structural material with higher temperature-stability than base alloys.

MMNCs are typically made via *ex situ* processing, where pre-manufactured materials such as carbides, silicides, nitrides, and oxides are obtained in powder form and incorporated into the Al matrix through a variety of methods [23]. Incorporation of carbon nanotubes (CNT), tungstides??, and borides have also been demonstrated [22, 24]. While *ex situ* production of MMNCs offers a diverse repertoire of usable reinforcements and processing procedures, *ex situ* processes suffer from the high cost of nano-sized material, poor wetting between reinforcement particles and the matrix, and contamination of reinforcement powders [25]. Much research has

been done to find alternative methods that create reinforcing particles *in situ* in the melt, thereby avoiding many of the pitfalls common in *ex situ* MMNCs. MMNCs created via *in situ* methods offer potential lower costs, fewer processing steps, smaller particles, better particle-matrix bonding, and improvements to mechanical properties [22]. The process for producing *in situ* MMNCs is not well developed which means that much work still needs to be done to fully understand the reaction pathways, kinetics of particle formation, and how to optimize processing parameters. The primary goal of this research was to investigate *in situ* MMNC processing methods which are feasible options for commercial scale production and understand the corresponding formation mechanisms and the processing-microstructure-property relationships needed to inform the design and production of the MMNCs.

1.2 Organization and overview of dissertation

The remainder of this dissertation is organized into four chapters. Chapter 2 presents an overview of the relevant literature for MMNC production, with a focus on *in situ* approaches of production. We will compare the advantages and disadvantages of *ex situ* and *in situ* processing methods and cover various MMNC processing approaches with particular detail for *in situ* methods studied in the proceeding chapters, namely metal-based polymer pyrolysis (MBPP) and salt-flux reaction synthesis (SFRS). This chapter will also cover relevant strengthening mechanisms of MMNCs and their related microstructure-mechanical property relationships, in order to identify the relevant reinforcement and microstructural characteristics.

Chapter 3 is a more detailed investigation into understanding the processing-properties relationships of MMNCs made via MBPP. This chapter starts with an in-depth analysis of commercially available polymers used as precursor material to Al-MMNCs, and their thermal degradation and pyrolysis. After this analysis the chapter transitions into how MBPP processing

was used to generate Al-based MMNCs, and their related microstructure and mechanical analysis. We demonstrated that MBPP can generate Al-based MMNCs with improved mechanical properties, although further work needs to be done to fine-tune the process for significant MMNC production.

Chapter 4 is a more detailed investigation of SFRS and its processing-microstructure relationships using 2D and 3D microstructural analysis. The insights found narrow down the reaction pathways of TiC formation in Al via SFRS and find a size distribution of the TiC particles. There is also significant discussion on how the intermetallic Al3Ti is affected by processing parameters, as well as a novel morphology of Al3Ti found by it nucleating on *in situ* TiC.

Chapter 5 builds on the work from Chapter 4, with a focus on how the presence of silicon at different weight percentages affects the microstructure and mechanical properties of the Al-TiC MMNCs generated via SFRS. Once more the microstructure is studied in both 2D and 3D. We find that Si leads to significant changes in both the carbide and the intermetallics which are formed, and therefore impacts the mechanical properties of the MMNCs.

Chapter 6 is a summary of the findings of this dissertation as well as some suggestions for future work based on the findings in Chapters 3, 4, and 5. We also discuss the need for improved understanding of the interactions between the metal solidification front and ceramic reinforcing particles, and go into some preliminary experiments conducted at Brookhaven National Laboratory on watching the particle and solidification front interactions in real time using Synchrotron-based X-ray radiography.

The Appendix includes helpful MATLAB functions that were used often for this work.

CHAPTER 2
Background Information

2.1 Production and processing of metal matrix nanocomposites

2.1.1 In situ vs ex situ processing methods

MMNCs can be produced in a variety of methods, but manufacturing procedures can broadly be split into *ex situ* and *in situ* processes. *Ex situ* processes involve the insertion or dispersion of pre-manufactured reinforcing particles into a metal matrix. For *ex situ* processes there are typically no interactions with or within the melt, and if possible reactions are avoided. *Ex situ* methods consist of both solid state and liquid state processing, some examples of which can be found in **Table 2.1** [17, 26-29]. *Ex situ* methods allow for large amounts of reinforcement to be added to the matrix, and for creating MMNCs which are otherwise not attainable, such as when individual elements of a ceramic particle are highly unstable or would alloy with a melt instead of forming a ceramic.

Table 2.1 Summary of selected *ex situ* metal matrix composite processing methods.

***Ex situ* methods**	
Solid-state Process	**Liquid-state process**
Powder Metallurgy	Stir Casting
Mechanical Alloying	Ultrasonic-assisted Cavitation
Equal Channel Angular Pressing	Melt Infiltration
Friction Stir Processing	Disintegrated Melt Deposition
Microwave Sintering	High Pressure Die-casting

There are some common issues with *ex situ* MMNC production. Since the reinforcing particles are premanufactured, oxidation and contamination tend to be a major issue for *ex situ* MMNC formation and prevent particles from forming clean interfaces and strong interfacial bonds with the matrix [12, 17, 28]. Contamination of the reinforcement can also lead to porosity of the final microstructure [17] and de-bonding of the particle-matrix interfaces [22, 25, 28, 30]. Furthermore, there is often poor wetting of the ceramic nanoparticles by the melt during conventional casting processes [17, 31]. Due to poor wetting and high surface energies between the nanoparticles and the melt, particles tend to agglomerate or cluster [14, 17, 22, 32, 33]. The poor wettability of the nanoparticles with the melt can also lead to rejection of the nanoparticles by the solidification front during solidification, resulting in particle agglomerates and interdendritic particle trapping [33-36]. The many issues with *ex situ* MMNCs often lead to lower-than-expected properties as the mechanical properties are directly related to how well the reinforcing phase is bonded with and dispersed throughout the material. On a production side, *ex situ* MMNC production suffer due to the high cost of micrometer or sub-micrometer sized ceramic particles used as reinforcements. Alternative processing methods are necessary for

producing low cost, high strength MMNCs which have superior high temperature mechanical properties.

In situ methods of producing MMNCs offer the potential to create nanocomposites while avoiding the pitfalls of *ex situ* methods. *In situ* methods differ from their *ex situ* counterparts in that the reinforcing phases are not premanufactured, but are instead made within the metal matrix. Historically, *in situ* Al composites were made by unidirectionally solidifying a eutectic alloy to create two-phase regions where intermetallics acted to reinforce lamellar [26]. Modern *in situ* methods create metal-ceramic composites where the reinforcing phases are created directly inside the Al melt during production via chemical reaction (solid-solid, liquid-liquid, solid-liquid, or gas-liquid) or morphological methods (See **Table 2.2** for a summary of processing methods) [17, 29, 37-39]. Some *in situ* processes follow similar steps to *ex situ* ones (e.g. powder metallurgy and mechanochemical synthesis are similar processes) but the key difference is that *in situ* processing generates reinforcing particles in the matrix, while *ex situ* processing is solely focused on dispersing premade particles.

Table 2.2 Summary of selected *in situ* metal matrix composite processing methods

***In situ* methods**				
Solid-solid Processes	**Liquid-solid Processes**	**Gas-liquid Processes**	**Liquid-liquid Processes**	**Morphological**
Mechanochemical Synthesis (Mechanical Alloying)	Self-propagating High-temperature Synthesis	*In situ* Gas Liquid Reaction Synthesis	Metal-based Polymer Pyrolysis	Rapid Solidification
Friction Stir Processing	Metal-based Polymer Pyrolysis	Direct Metal Oxidation (DIMOX)	MixAlloy™ (Mixing molten alloys)	Severe Plastic Deformation
Reaction Milling	Salt-flux Reaction Synthesis			
	Exothermic Dispersion			
	Additive Manufacturing (AM)			

In situ processing methods for manufacturing MMNCS offer several advantages over *ex situ* methods. Since the nanoparticles are made inside of the melt, they are thermodynamically

stable with the matrix, and their surfaces are free from contaminants or oxidation [22, 29, 35, 40-44]. Both factors lead to stronger interfacial bonds and less degradation with thermal cycling [45-48]. Particles formed *in situ* tend to be smaller than those added *via ex situ* methods and are more homogeneously dispersed [44, 49]. It has also been shown that some *in situ* methods lead to dispersion of ceramic particles at a nano-level via nano and micro-indentation tests [50]. Importantly, *in situ* methods do not rely on premanufactured powders so the material costs are typically less than *ex situ* methods when creating MMNCs, and some *in situ* methods promise single-stage MMNC production [17, 47]. The benefits of particle bonding, dispersion, and size reduction translate to stronger mechanical properties as compared with *ex situ* MMNCs, thus making *in situ* processing of MMNCs an attractive and cost-effective manner of forming high strength and high temperature material.

More in-depth information of the various MMNC processing methods are available at [2, 12, 13, 17, 22, 29, 48, 51-61]. Of the many *in situ* production methods, two will be the primary focus of this project: metal-based polymer pyrolysis (MBPP) and salt-flux reaction synthesis (SRFS). MBPP is an attractive *in situ* process as it can occur at temperatures lower than other *in situ* methods, such as self-propagating high-temperature synthesis. More details on MBPP can be found in Chapter 3. SFRS was identified as a promising processing method through our previous project with the Lightweight Innovations for Tomorrow (LIFT) Institute (Detroit, MI) along with our interactions with Professor Xiaochun Li's group at the University of California – Los Angeles, who had recent results with the process.

2.1.2 Metal-based polymer pyrolysis

The metal-Based polymer pyrolysis (MBPP) process can be either a liquid-liquid or solid-liquid reaction, depending on the state of the precursor polymer. MBPP uses specially

designed organic materials that turn into polymer-derived ceramics (PDC) upon pyrolysis. These materials have been used for protective coatings (e.g. anti-oxidation and corrosion, scratch-resistant, hydrophobic) [62-69], antimicrobial coatings [70, 71], additive manufacturing [72, 73], battery anode materials [74], and ceramic matrix composites [75, 76] but have only been used to create MMNCs recently with Mg and Cu matrices [77, 78]. Most PDC precursors have a Si-based backbone (as opposed to a C-based backbone, see **Fig. 2.1b**) and are designed so that all of the required chemicals for the ceramic are already present in the polymer structure: most breakdown into SiC, SiCN, or SICNO with yields ranging from 65-90 wt% [50, 65, 79, 80].

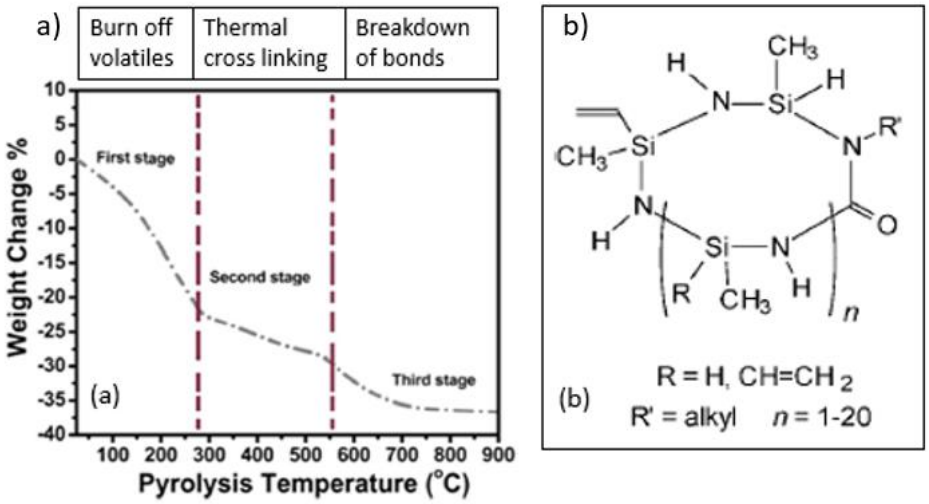

Figure 2.1 (a) Thermogravimetric analysis of a precursor polymer undergoing pyrolysis (adapted from [83]) (b) Simplified structure of the precurosro polymer Ceraset® by EMD Performance Materials [79]

Pyrolysis is the thermal decomposition of organic material in the absence of oxygen [81-83]. Pyrolysis occurs in four stages, each occurring at a different temperature regime (**Fig. 2.1a**): the first stage involves burning off volatiles and low molecular weight polymers, in the second stage the polymer undergoes thermal cross-linking, and the final stage is ceramization, or the breakdown of molecular bonds and restructuring into ionic bonds [79, 80, 84, 85]. The third stage is the most important for MBPP and occurs in a large temperature range (from 500 – 1200

°C) depending on the polymer in question. The fourth stage is crystallization of the polymer-derived ceramics, but for the purposes of this work this stage will be ignored as it requires exceedingly high temperatures (T > 1000 °C). Other methods of pyrolysis include irradiating precursor polymers with a laser or ion source to break the molecular bonds [80, 86-89].

Unlike other *in situ* methods, the ceramics derived through MBPP are not made by reacting with the matrix at all, it relies solely on the chemicals which are built into the polymer

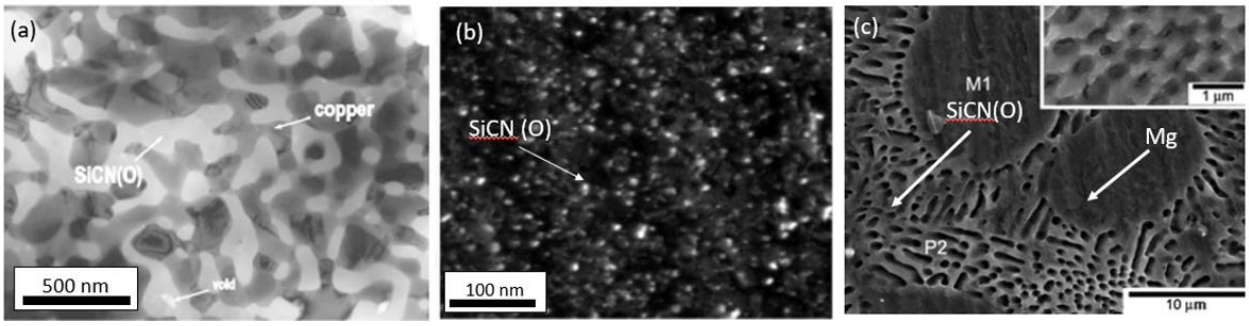

Figure 2.2 Example microstructure of composites made via metal-based polymer pyrolysis (a) TEM of 30 vol% SiCN(O)/Cu made via hot consolidation of polymer and Cu powders [94] (b) TEM of SiCN(O)/Cu made by friction stir processing polymer into the Cu matrix [93] (C) SEM of an SiCN(O)/Mg MMNC made by stir casting [96]

backbone and R groups. For the MBPP process, the metal matrix acts as a pseudo-inert environment for break-down of the polymer; the polymer may be added to the melt in its virgin liquid state or it can thermally cross-linked into a resin and ball milled into a powder then added in a with stir casting or with friction stir processing (FSP) [50, 84, 90, 91]. The matrix must be held at a relatively high temperature ($600 < T < 900\,^{o}C$) in order for the incorporated polymer to pyrolyze into ceramic, some porosity is created from the exuded gas and volatiles during the pyrolysis [84, 90, 92]. MBPP has been used to create Mg-MMNCs and Cu-MMNCs via stir casting, friction stir processing, and hot consolidation, their microstructure can be found in **Fig.**

2.2 [83, 91, 93-96]. MMNCs made via MBPP have shown increased mechanical properties and retention of strength at elevated temperatures (**Fig. 2.3**), which makes it worth pursuing with Al.

2.1.3 Salt-flux reaction synthesis

There is a strong history of using flux during metallurgical processing to create a protective layer over the melt and prevent excessive oxidation. *Ex situ* MMNCs can be produced the assistance of standard fluxes: mixing reinforcement with flux allows for improved particle incorporation due to the breakdown of the oxide skin on top of the melt and enhanced particle wetting by the metal matrix [97-99]. A similar process first discovered in the 1990's can be used to generate *in situ* MMNCs by carefully selecting a flux and adding elemental powders to react and form nanoparticles within the melt or the molten flux layer [53, 98, 100-103]. In salt-flux

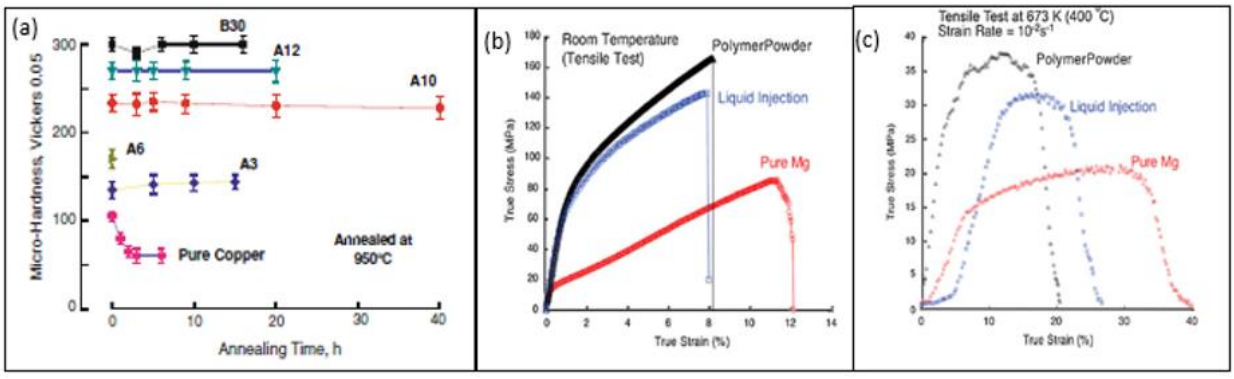

Figure 2.3 (a) Micro-hardness vs annealing time at 950 °C for Cu-MMNCs [94] (b) Room temperature stress-strain curves for pure Mg, Mg-MMNC made with liquid polymer injected into the matrix, and Mg-MMNC with polymer powder added to the matrix [96] (c) High temperature tensile test (T = 400 °C) for the same MMNCs as (a) [96]

reaction synthesis a salt-based flux is blended with elemental powders, then the mixture is added to the melt where the flux liquifies and breaks down from the heat and from reacting the oxide skin. As the flux breaks down it releases solute atoms (e.g. Ti or B) that either react with the

added elemental powders or directly with the melt. Salt-flux reaction synthesis has strong promise for scaling up MMNC production as surface fluxes are already a common practice in industry. As with other *in situ* methods MMNC processes the composites are limited by the available precursors, in this case known flux and elemental powder chemistries. Most studies of this type used K_2TiF_6 and KBF_4, either separate or together, to produce a variety of composites such as Al/TiC [4, 53, 100-102, 104-108], Al/carbon fiber [109], Al/TiB_2 [103, 110], Al/Al_3Ti [111, 112], and Al/AlB_2 [113]. Similarly K_2ZrF_6 has been used to generate Al_3Zr and ZrB *in situ* [4, 114, 115].

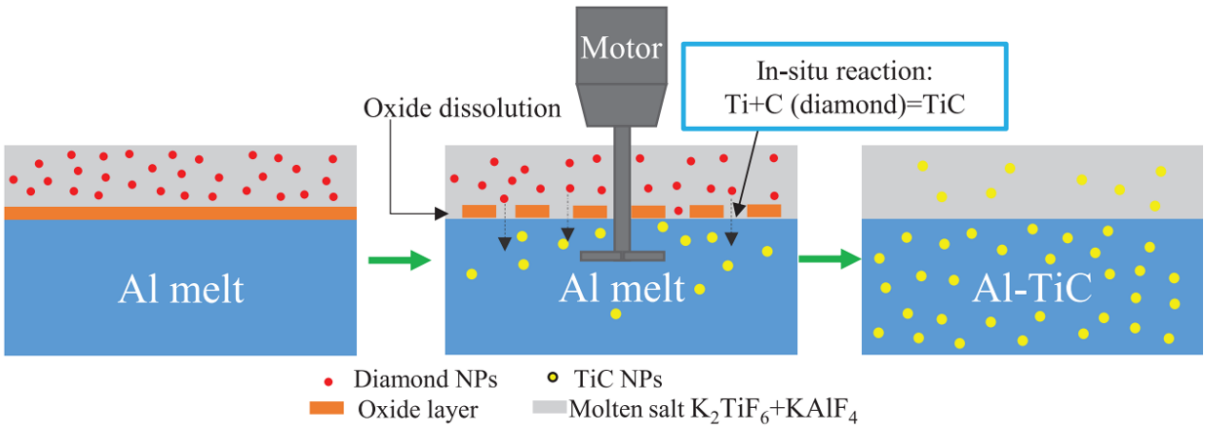

Figure 2.4 Schematic of the salt-flux reaction synthesis for generation of TiC in Al, adapted from [100]

The salt-flux reaction is typically combined with mechanical stirring. Electromagnetic stirring has been shown to decrease particle and grain size [104]. Since this technique only requires enough Al to reduce the flux components it is fairly easy to incorporate into Al processing, and it can be used in many Al alloys, and has been shown to work on A356, 2024, AA77075, and 6351 to name a few [105, 106, 114, 115]. Interestingly, changing the alloy composition can lower the reaction temperature of the salts down to as low as 720 °C [115]. On top of alloy flexibility, the salts used are fairly low cost, and can reliably make micrometer and sub-micrometer sized reinforcements [53, 116]. While most of salt-flux reactions occur between

800-900 °C, it has been found that higher temperatures can lead to smaller and better dispersed precipitates [4, 106]. A schematic of the salt-flux reaction synthesis is displayed in **Fig. 2.4**. Some examples of Al-MMNC microstructure made via salt-flux reaction synthesis can be found in **Fig. 2.5**.

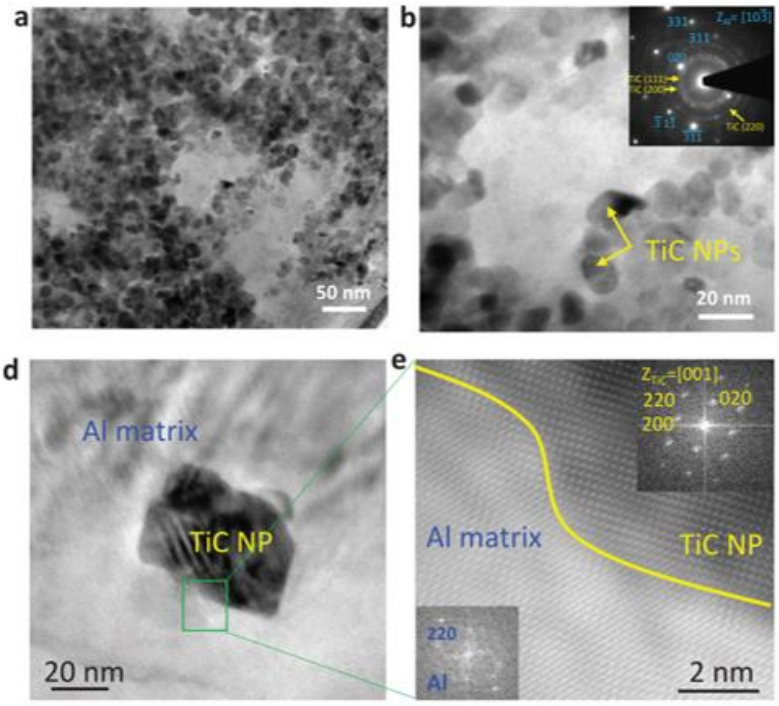

Figure 2.5 (a,b) TEM images of TiC nanoparticles in an Al matrix made via salt-flux reaction synthesis. Inset of (b) is the diffraction pattern of the nanoparticles [100]

Another important point is that TiC often forms in sub-stoichiometric Ti/C ratios when made via salt-flux reaction synthesis, primarily with C-vacancies, without changing the TiC structure [117-121]. The shape of the TiC is heavily influenced by the ratio of C/Ti: a perfect 1:1 C:Ti ratio leads to spherical shapes but reducing the amount of C increases the faceting of the

structure from ellipsoid (C/Ti < 1.0) to octahedral (C/Ti << 1.0), and can even become cuboids when there is more C than Ti present [122, 123]. Work by Dong *et al.* classified the different morphologies of TiC_x that form with varying C/Ti ratios, an overview of their findings can be seen in **Fig. 2.6** [122].

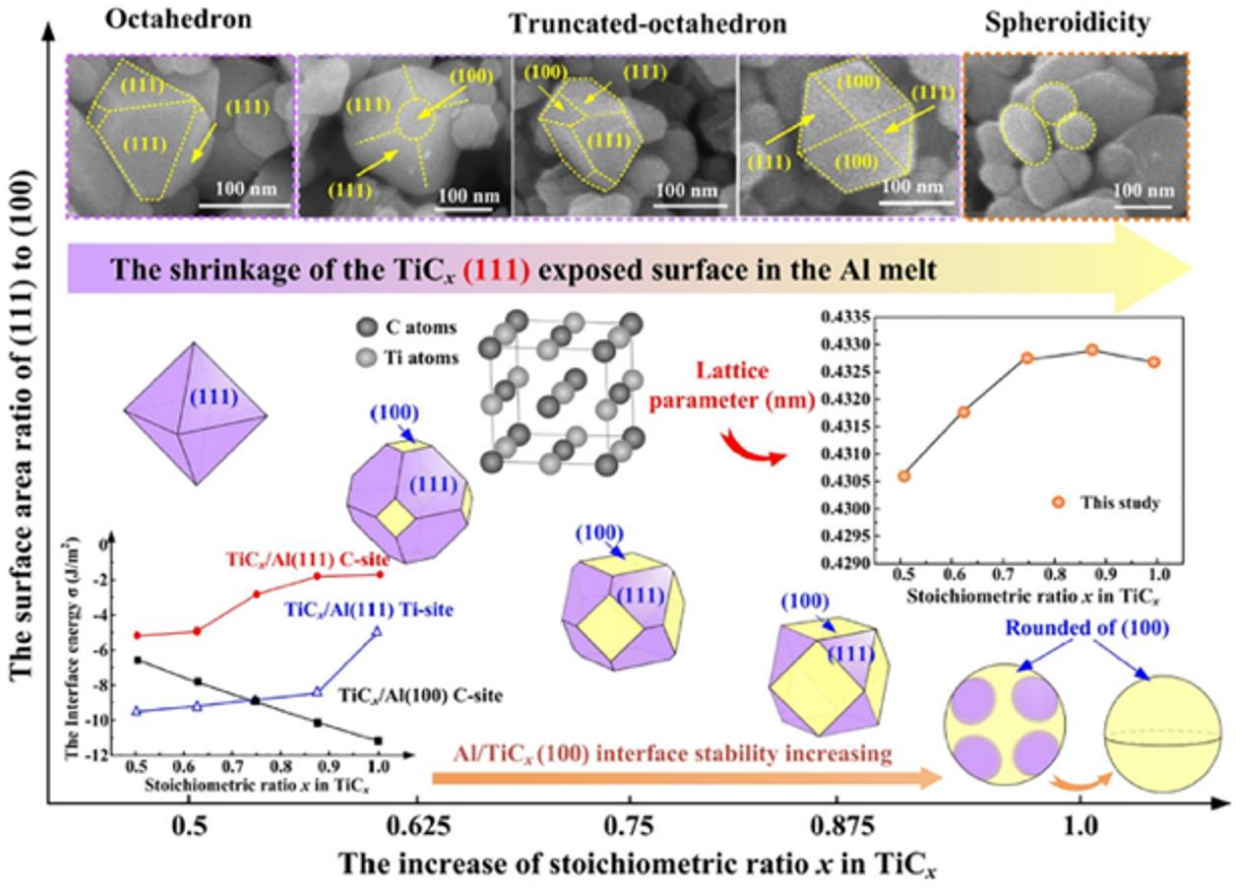

Figure 2.6 Schematic of the morphological evolution of TiC_x with increasing C/Ti ratios [122]

2.2 Microstructure-properties relationships of metal matrix nanocomposites

2.2.1 Strengthening mechanisms and theory

The key to improving mechanical properties of an MMNC is understanding how the reinforcing particles affect those properties and what can be done to optimize their effects. Crucial MMNC characteristics include the volume fraction (V_f), size distribution, homogeneity, and morphology of the reinforcing particles [22]. Mechanical properties of concern include the ultimate tensile strength (UTS), yield strength (YS), Vickers microhardness (VH), and fatigue strength. There is a significant amount of literature reviewing the strengthening mechanisms of MMNCs [15, 22, 124-129], the main mechanisms by which reinforcing particles affect the MMNC properties are outlined below.

- Coefficient of thermal expansion (and elastic modulus) mismatch strengthening: The density of dislocations in a metal (or metal-based composite) significantly affects its mechanical properties. There is a large difference in the coefficients of thermal expansion (CTE) for the nanoparticles and metal matrix, which leads to thermal stresses occurring at the nanoparticle/matrix interface during heating and cooling. Similarly, the two phases have different elastic moduli (EM), the mismatch of which leads to stress localized around the nanoparticle/matrix interface under applied loads. Both CTE and EM mismatches create localized zones of stress which can induce plastic deformation and generate dislocations around the nanoparticle/matrix interface which reinforces the microstructure [22]. The increase in dislocation density from CTE and EM mismatch are given by Eqns. (2.1) and (2.2), respectively [22]:

$$\rho_{CTE} = \frac{A\,\Delta\alpha\,\Delta T\,V_f}{b\,d_p\left(1 - V_f\right)} \tag{2.1}$$

$$\rho_{EM} = \frac{6\,V_f}{\pi\,d_p^3}\,\epsilon \tag{2.2}$$

A is a geometric factor dependent on particle geometry, *b* is the Burgers vector, V_f is the volume fraction of reinforcing particles, d_p is the average diameter of the particles, ΔT is the temperature difference between the MMNC processing and test temperatures, $\Delta\alpha$ is the difference in CTE between the matrix and nanoparticles, and ϵ is the uniform deformation. The combined strengthening contribution from CTE and EM mismatch can be related by [22, 126]:

$$\Delta\sigma_{CTE+EM} = (M\,\beta\,G_m\,b\,\sqrt{\rho_{CTE}}) + (\sqrt{3}\,\alpha\,G_m\,b\,\sqrt{\rho_{EM}}) \tag{2.3}$$

where *M* is the Taylor factor (~1), β is a strengthening coefficient (usually ~1.25), α is a strengthening coefficient (usually ~0.5), G_m is the shear modulus of the matrix, and *b* is the Burgers vector.

- Hall-Petch strengthening: Grain size has a significant effect on the mechanical properties of alloys as grain boundaries can hinder dislocation movement. Different grain orientation and the high level of lattice disorder in grain boundaries prevent dislocations from moving in a continuous slip plane [22, 130]. The Hall-Petch equation relates strength to average grain size (d_m):

$$\Delta\sigma_{H-P} = k_y\,(d_m)^{\frac{-1}{2}} \tag{2.4}$$

Where k_y is a material dependent strengthening coefficient. Within an MMNC, nanoparticles can act as grain nucleation sites, thereby increasing the number of and decreasing size of grains, and can also pin grain boundaries, stopping their growth [22]. Together, the increase in the volume fraction (*Vf*) of particles and the decrease in particle size (d_p) lead to a finer structure given theoretically by the Zener equation [126]:

$$d_m = \frac{4\ \alpha\ d_p}{3\ V_f} \tag{2.5}$$

Where α is a proportionality constant and V_f is the volume fraction of particles.

- Orowan strengthening: Orowan strengthening refers to the phenomenon where dislocations are pinned or trapped by closely spaced particles. Since the ceramic nanoparticles are non-shearable, the dislocations must loop around the particles in order to bypass them (Orowan bowing), which localizes them to the nanoparticle/matrix interface under load. While Orowan strengthening is minimal for micrometer-sized reinforcement, it becomes increasingly effective for MMNCs due to the small scale of the reinforcing particles [37]. Orowan strengthening can be expressed by Eqn 2.6a[22]:

$$\Delta\sigma_{OR} = \frac{0.13bG_m}{\lambda} * \ln\left(\frac{d_p}{2b}\right) \tag{2.6a}$$

Where G_m is the shear modulus of the matrix, b is the Burgers vector, d_p is the average particle size, and λ is defined in Eqn 2.6b.

$$\lambda = d_p\left[\left(\frac{1}{2}\ V_f\right)^{\frac{1}{3}} - 1\right] \tag{2.6b}$$

- Load Transfer: Load transfer is the most direct form of strengthening, where an applied load is transferred from the softer matrix material to the reinforcing particles. The effectiveness of load transfer is dependent on the aspect ratio and size of the reinforcement. The strengthening effects from this mechanism can be described by [22]:

$$\Delta\sigma_{LT} = V_f\ \sigma_m\left[\frac{(l+t)A}{4l}\right] \tag{2.7}$$

Where σ_m is the yield strength of the unreinforced matrix, l and t are the size of the particle parallel and perpendicular to the loading direction, respectively, A is the particle aspect ratio, and V_f is the volume fraction of particles. For spherical particles Eqn 2.7 reduces to Eqn 2.8,

$$\Delta\sigma_{\mathrm{LT}} = \frac{1}{2} V_f \sigma_m \tag{2.8}$$

The overall strength of the composite can be evaluated by summing the above contributions with the original yield strength of the unreinforced matrix, and several unified models of strengthening have been proposed in literature [15, 125-128, 131]. Few studies have focused on nano-sized particulates, most are optimized for micrometer-sized particles, but Casati and Vedani, as well as Santay-Zadeh have come up with models for strengthening mechanisms of MMNCs [22, 126]. Their approach assumes linear independence of each strengthening mechanism so the net strength enhancement is given by Eqn. 2.9.

$$\sigma_y(MMNC) = \sigma_m + \sqrt{(\Delta\sigma_{LT})^2 + (\sigma_{H-P})^2 + (\Delta\sigma_{CTE+EM})^2 + (\Delta\sigma_{OR})^2} \tag{2.9}$$

Where $\sigma_y(MMNC)$ is the enhanced yield strength of the nanocomposite, σ_m is the yield strength of the matrix, and $\Delta\sigma_i$ is the respective contribution to yield strength of each mechanism.

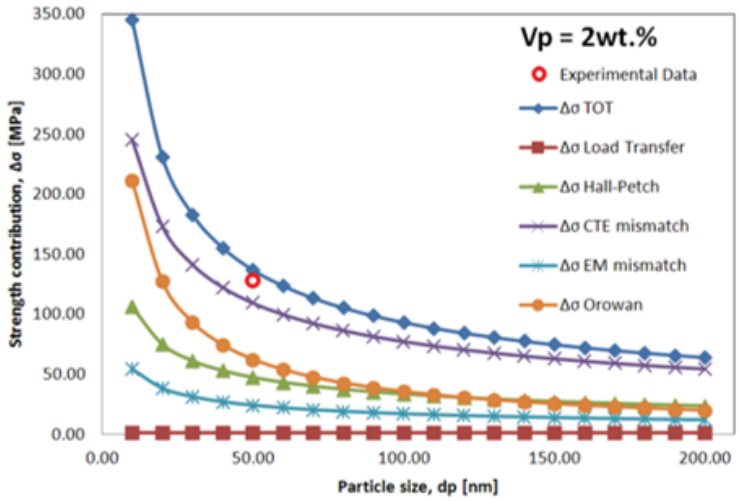

Figure 2.7 Simulated contributions from various strengthening mechanisms versus particle size for an Al/Al2O3 metal matrix composite [22]

Sanaty-Zadeh found that the enhancement of the mechanisms varies significantly based on the size of the reinforcing particle size, with a particularly strong effect on dislocation density,

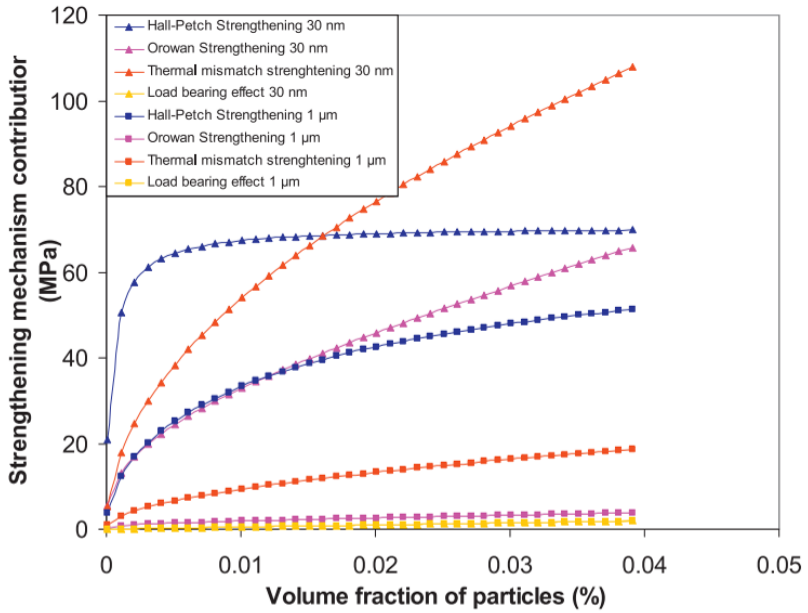

Figure 2.8 Simulated strengthening mechanism contributions as a function of volume fraction of particles, with a particle size of 10 nm [126]

grain refinement, and Orowan strengthening for nano-sized reinforcements. **Fig. 2.7** shows how the strengthening effects become increasingly impactful as the particle size decreases for Al strengthened with 2 wt% Al_2O_3. **Fig. 2.8** compares the effects of 30 nm particles to those of 1 μm particles. Note the small volume fraction of nanoparticles required to induce large increases in YS in **Fig. 2.8**.

Based on the theory reviewed in this chapter it is clear that the direct impact of an individual strengthening mechanism is difficult to separate from the overall enhancement seen by an MMNC. Luckily there are a few recurring terms in the enhancement equations, which point to particular reinforcement characteristics as the most important for strengthening, namely volume

fraction and reinforcement size. Both of these factors are expected to contribute to load transfer, enhanced dislocation density, Orowan strengthening, and grain refinement.

2.3 Background summary

This chapter reviewed several ways to create metal matrix nanocomposites, with a particular focus on *in situ* and *ex situ* MMNCs, as well as the theory and experimental literature relating to strengthening mechanisms for MMNCs. There is a clear need to control the properties of the particle reinforcement as the properties directly impact on the properties of the material as a whole. Volume fraction of reinforcement, reinforcement size, particle dispersion or agglomeration, and the strength of the particle/matrix interface are the key factors for getting the most improvement in mechanical properties for MMNCs.

In situ MMNCs offer great promise for the next stage of MMNC production as they offer inherently cleaner particle-matrix interfaces, more stable reinforcing particles, and sub-micrometer particles. These methods also seem the most promising for incorporating into bulk material generation due to their reduced cost and potentially one-step processes. Unfortunately, since the particles are made *in situ* there needs to be greater understanding on how processing parameters affect the produced particles and the subsequent mechanical properties of the generated MMNC. In the following chapters we will investigate two *in situ* MMNC processing techniques to better understand their processing-properties relationships and particle generation pathways.

CHAPTER 3
Exploring Metal-Based Polymer Pyrolysis in Al and Other Metals

Note: Portions of the work presented in this chapter have been adapted from A. Gladstein and A. Taub, submitted to the Journal of Composite Materials.

3.1 Introduction

There is continued push for Al-based metal matrix nanocomposites (MMNCs) for structural applications in transportation and aerospace sectors in order to leverage aluminum's natural high strength to weight ratio with the additional strengthening and stabilizing effects of the ceramic particles [23, 51]. Broadly speaking, MMNCs can be generated either with *ex situ* methods, where premade particles are mixed into the metal, or *in situ*, where particles are created directly in the matrix during the processing. *In situ* MMNCs are showing increasing promise for their potential of scalability and their promise to avoid the problems of *ex situ* MMNCs, mainly high particle cost, particle contamination, and poor particle wetting/incorporation [51, 52, 57, 60, 61, 132, 133]. Despite their promise, there is still significant amount of work to be done to optimize the production and properties of *in situ* MMNCs. Furthermore, there are a variety of *in situ* processes being researched, many of which require temperatures beyond the normal scope of Al-processing for the *in situ* processing to occur [18, 19, 48, 57, 100, 134, 135]. Consequently there is a need for a lower temperature *in situ* process for MMNC production.

The work done in this chapter sought to explore a new, potentially lower temperature *in situ* MMNC production method. The overall project objective was to investigate the feasibility of

using metal-based polymer pyrolysis (MBPP) to create Al-based MMNCs. First, multiple commercially available polymer precursors were identified and analyzed for their feasibility in MBPP. After this analysis a few polymers were selected for MBPP experiments, and a variety of experimental methods were done to create MBPP MMNCs. Finally, we discuss the viability of MBPP as a production method for MMNCs.

3.2 Polymer analysis

3.2.1 Reviewing potential polymer precursors

Multiple polymeric precursors were investigated as MBPP precursor material. The first material tested was a polysilazane named Durazane® 1800 produced by EMD Performance Materials, Merck KGaA (Darmstadt, Germany) [136]. In literature Durazane® 1800 has multiple names: most commonly it is called a polysilazane (PSZ) [63, 64, 72, 75, 81, 137, 138], although it is occasionally referred to as an oligosilazane [62, 69, 71] for individual or small molecule of the material, as an organosilazane or polyorganosilazane as its Si-C bonding makes it an organosilicon compound [70, 139, 140], or more specifically it is called a poly(vinyl)silazane (PVS) [74, 76], a poly(methylvinyl)silazane (PMVS) [73, 141, 142], or poly(ureamethylvinyl)silazane (PUMVS) [143] due to its various side groups.

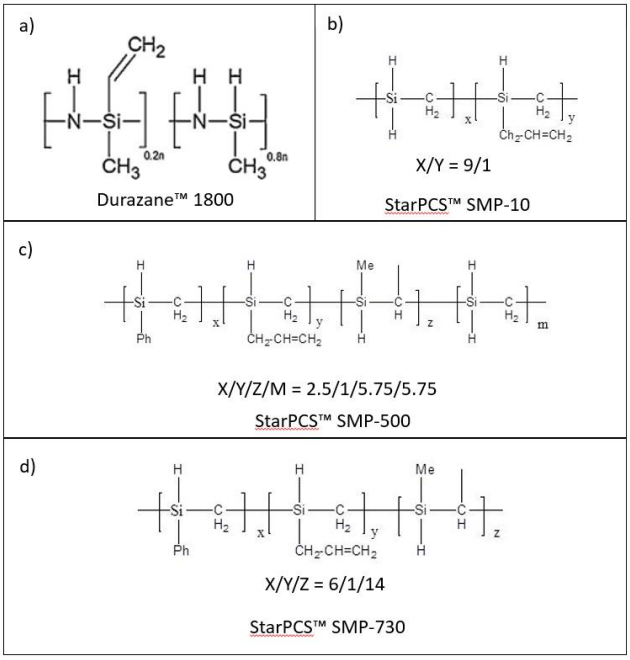

Figure 3.1 Simplified chemical structures for (a) Durazane 1800 [62], (b) StarPCS™ SMP-10, (c) StarPCS™ SMP-500, and (d) StarPCS™ SMP-730. (b-d) are from [144-146]

The next came three different polycarbosilane precursors made by Starfire Systems Inc. (New York, USA), named StarPCS™ SMP-10, StarPCS™ SMP-500, and StarPCS™ SMP-730 [144-146]. While the three SMP precursors are similar to one another there is some variation: SMP-10 is an allylhydridopolycarbosilane, while SMP-500 and SMP-730 are allylhydridophenylpolycarbosilanes, meaning that they both have a phenyl side group (C_6H_5), which is labeled with a, "Ph" in **Fig. 3.1** [144-146]. Another difference between these four is their chain length and subsequent amount of cross-linking in their structure, and how that affects their physical appearance. In the as-received state at room temperature DZ is a clear liquid, SMP-10 is a yellow-brown liquid, SMP-500 is an amber colored viscous liquid, and SMP-730 is an amber colored solid with a melting point of 30-100 °C [144-146]. Their exact viscosities and other information are shown in **Table 3.1**.

For the purposes of this chapter, I will refer to these polymers as DZ, SMP-10, SMP-500, and SMP-730, respectively. All of these polymers are designed specifically to create Si-based

carbide material after pyrolysis by including a large amount of Si in their backbone: DZ is sold as a precursor to create SiCN ceramics, while the SMP polymers are designed to generate SiC only. Their formulas can be found in **Fig. 3.1**. Their exact formula are proprietary so there is some amount unaccounted for items such as the exact side groups, stabilizers, and filler material used in these materials.

Table 3.1 Supplier information for precursor polymers [62, 144-146]

Material	**Type of Polymer**	**Expected Ceramic**	**Ceramic Yield [wt%]**	**Viscosity at 25 °C [cPs]**	**Density [g/cm^3]**
Durazane® 1800	Polysilazane	SiC, SiCN	80-90	10-40	0.95 - 1.05
StarPCS™ SMP-10	Allylhydridopolycarbosilane	SiC	72-78	40-100	0.998-1
StarPCS™ SMP-500	Allylhydridophenylpolycarbosilane	SiC	65-70	3,000-10,000	1
StarPCS™ SMP-730	Allylhydridophenylpolycarbosilane	SiC	65-67	N/A (Solid)	1-1.1
Genesis	15-40% Pentaerythritol Tetracrylate 15-40% Urethane Acrylate Ester 15-30% Urethane Acrylate	-	-	200-400	1.08
Flexalite	5-25% Pentaerythritol Tetracrylate 45-90% Acrylate Ester 5-25% Urethane Acrylate	-	-	-	-

The final two precursor materials that were explored were Genesis and Flexalite® which are photocurable resins made by the additive manufacturing company Tethon 3D. Both Genesis and Flexalite® are a mixture primarily of acrylate ester, urethane acrylate, and pentaerythritol tetraacrylate [147, 148]. Tethon 3D specializes in 3D printing ceramic materials, so we thought their material would be worth adding to this investigation. As it turns out, these polymers were not made as precursors to polymer-derived ceramics but were used in conjunction with premade ceramic particles that would be mixed in using their proprietary additive manufacturing apparatus. Since this study was concluded, Tethon 3D has developed other materials to additively manufacture with ceramics, but they consist of premade ceramics mixed in with a

polymeric, and thus making them unusable for the purposes of this research. The work done investigating these two polymers will still be reported here.

3.2.2 Initial thermogravimetric analysis work

The first step of analyzing the polymeric precursors for their feasibility in MBPP experiments was to find their ceramic yield and pyrolysis temperature regime using a thermogravimetric analysis coupled with differential scanning calorimetry (TGA-DSC). Initial experiments were conducted using a SDT 2960 Simultaneous DSC-TGA (TA Instruments, Delaware, USA) in Prof. Richard Laine's lab (University of Michigan – Materials Science and Engineering department), although at the time the machine was limited to TGA only. Tests in this machine were done with a ramp rate of 10 °C/min, a flow of 60 mL/min of N2, and a sampling rate of 0.5 s/pt unless otherwise stated. TGA results were recorded from 100 – 900 °C, with results from <100 °C being discarded due to potential effects of moisture in the sample or environment. Samples were all 20-50 mg and tested in their as-received state. All TGA-DSC data was analyzed and plotted using TA Instruments Universal Analysis 2000 software (V4.5A).

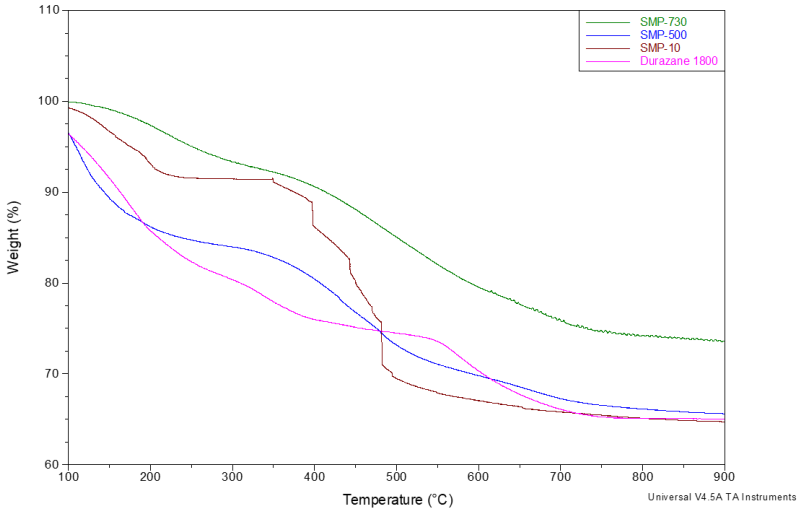

Figure 3.2 Initial thermogravimetric analysis results for polymers heated at 10 °C/minute

Results of these initial TGA tests are shown in **Fig. 3.2**, with the results of the Tethon 3D materials shown in **Fig. 3.3** and relevant information listed in **Table 3.2**. It is clear from these results that Flexalite and Genesis were not adequate materials for this project as they had essentially no ceramic yield, so no further experiments were conducted on them. The other polymer precursors showed better promise for MBPP experiments with a ceramic yield 65-75 wt%, which is similar to what is displayed in literature [136, 143-146, 149], along with pyrolysis temperatures near normal operating temperatures for molten Al (see **Table 3.2**). The TGA plots

Table 3.2 Significant information from initial thermogravimetric analysis

Material	**5 °C/min, Ar**		**10 °C/min, N2**		**20 °C/min, Ar**	
	Yield at 900 °C (wt%)	**Yield Temperature (°C)**	**Yield at 900 °C (wt%)**	**Yield Temperature (°C)**	**Yield at 900 °C (wt%)**	**Yield Temperature (°C)**
Durazane 1800	N/A	N/A	65	785	61	800
Durazane 1800 (Air)	N/A	N/A	79	670	N/A	N/A
SMP-10	69	660	65	700	53	750
SMP-500	N/A	N/A	65	850	73	850
SMP-730	N/A	N/A	74	800	71	850
Genesis	N/A	N/A	5	500	N/A	N/A
Flexalite	N/A	N/A	0	500	N/A	N/A

of these polymers each have a few regions of plateauing prior to pyrolysis, which is related to the stages of polymer decomposition: burning off of side-groups and smaller chains, thermal cross-linking, and finally pyrolysis. The TGA data was used to find the temperature regimes for these stages of degradation and helped inform some initial MBPP experiments, especially in regard to how the precursor polymers could or could not be thermally cross-linked prior to adding them to a metal melt.

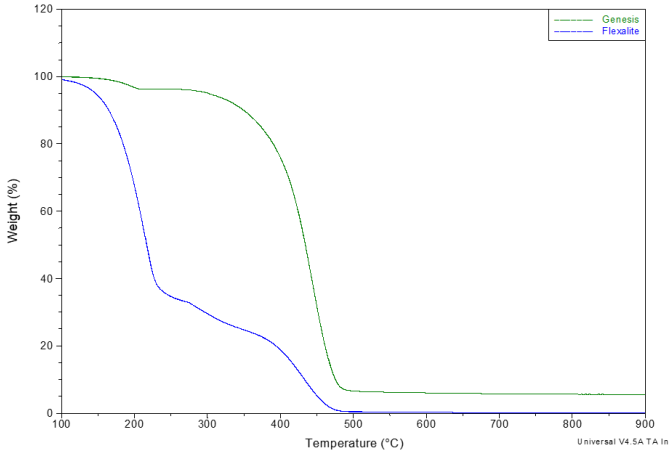

Figure 3.3 Thermogravimetric analysis of the Genesis and Flexalite polymers

A final test with Prof. Laine's equipment was done with the same testing method to compare the yield of DZ when heated in air versus in N_2. The results of this experiment are shown in **Fig. 3.4**, with the key findings in **Table 3.3**. The yield for DZ increased from 65 wt%

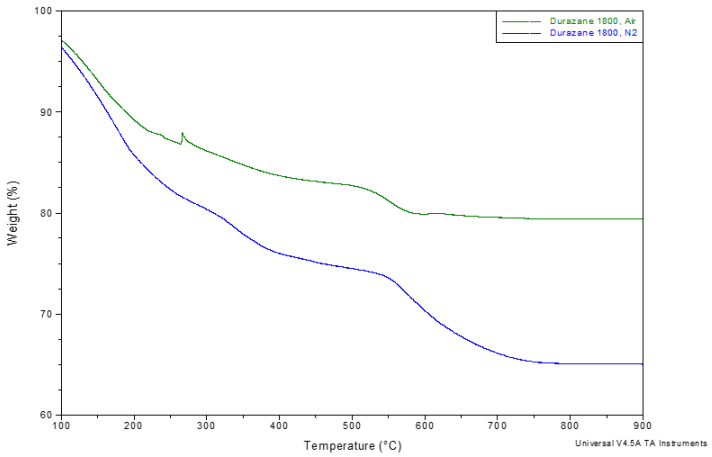

Figure 3.4 Thermogravimetric analysis of Durazane 1800 in air and in N_2

to 79 wt% in the presence of air, although this increase is likely due to the polymer absorbing a significant amount of oxygen during decomposition and not related to an increase in SiCN ceramic yield. The two plots follow similar trends, showing an initial large loss of material, followed by a slower loss 300-550 °C, and the start of pyrolysis around 550 °C, although the final weight loss in air occurs far faster likely due to oxidation and burning of the material

requiring less energy, and therefore lower temperatures, than true pyrolysis. After this analysis we concluded this test was not worth repeating with the SMP polymers because it was clear that the polymers would likely absorb significant oxygen and react strongly if pyrolyzed in air and because the pyrolysis for MBPP experiments should occur inside of a metal, thereby limiting the amount of oxygen present during pyrolysis.

Table 3.3 Weight loss and temperature range associated with each stage of pyrolysis for four precursor polymers

Material	**Stage I**		**Stage II**		**Stage III**	
	Weight loss (%)	**Temperature range (°C)**	**Weight loss (%)**	**Temperature range (°C)**	**Weight loss (%)**	**Temperature range (°C)**
DZ	23	25-340	6.5	340-500	10.5	500-940
SMP-10	7	25-225	19	225-490	5.5	490->900
SMP-500	16.5	25-444	10	444-840	0.5	>840
MP-730	11	25-440	17	440-775	1.5	>775

3.2.3 Thermogravimetric analysis and differential scanning calorimetry analysis of selected precursors

After initial TGA work done in Prof. Laine's lab it was clear that we needed to perform TGA-DSC experiments on the material to better understand their thermal decomposition process, as the heat flow information from the DSC results would better inform when reactions are occurring in the polymer degradation. To do these experiments we used a SDT Q600 simultaneous TGA/DSC (TA Instruments, Delaware, USA) in Prof. Andre Boehman's lab (University of Michigan – Mechanical Engineering department). Samples of the polymers were all tested from their as-received states and weighed to be 30-50 mg per instrument instructions. Tests with this machine were done initially with a ramp rate of 20 °C/min under a flow of 100 mL/min of Ar and a sampling rate of 0.5 s/pt. These samples were equilibrated at 100 °C, then heated from 100 to 1000 °C. The SMP-10 was later heated at a rate of 5 °C/min due to its

extreme drop in mass over a short temperature range, while keeping all other testing parameters. The TGA results alone are shown in **Fig. 3.5**, while the TGA-DSC results are shown in **Fig. 3.6**, and key findings in **Table 3.2**. The ceramic yield tended to decrease from these experiments when compared to the experiments with a slower heating rate, which is to be expected as the polymeric chains would have less time to cross-link and stabilize during faster heating procedures.

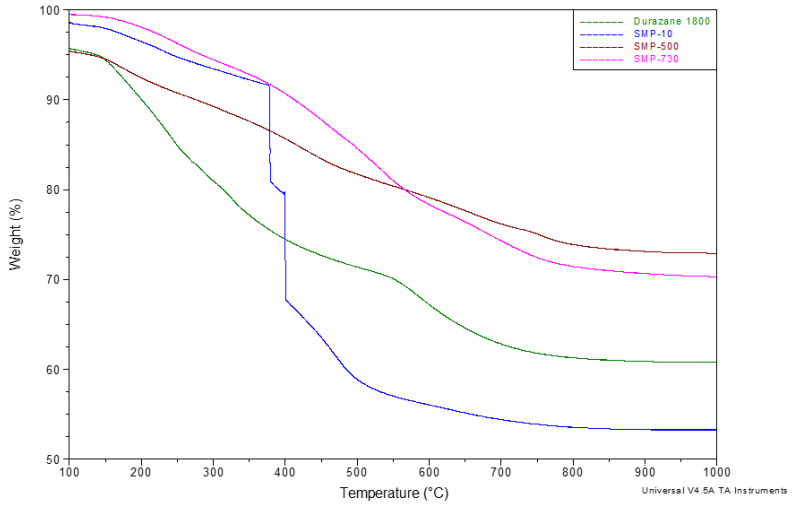

Figure 3.5 Thermogravimetric analysis for the selected precursor polymers heating at 20 C per minute under Ar

As shown in **Fig. 3.6** there are multiple steps to the polymer-to-ceramic conversion process which can broadly be broken up into four significant stages which are labelled with I, II, III, and IV on the figure. These regimes are typically found by matching curvature changes in the TGA data with peaks or troughs with the DSC data, as a peak in the DSC correlates with a large exothermic or endothermic reaction. The temperature range of each stage is polymer-dependent, but generally they each occur over a few hundred degrees.

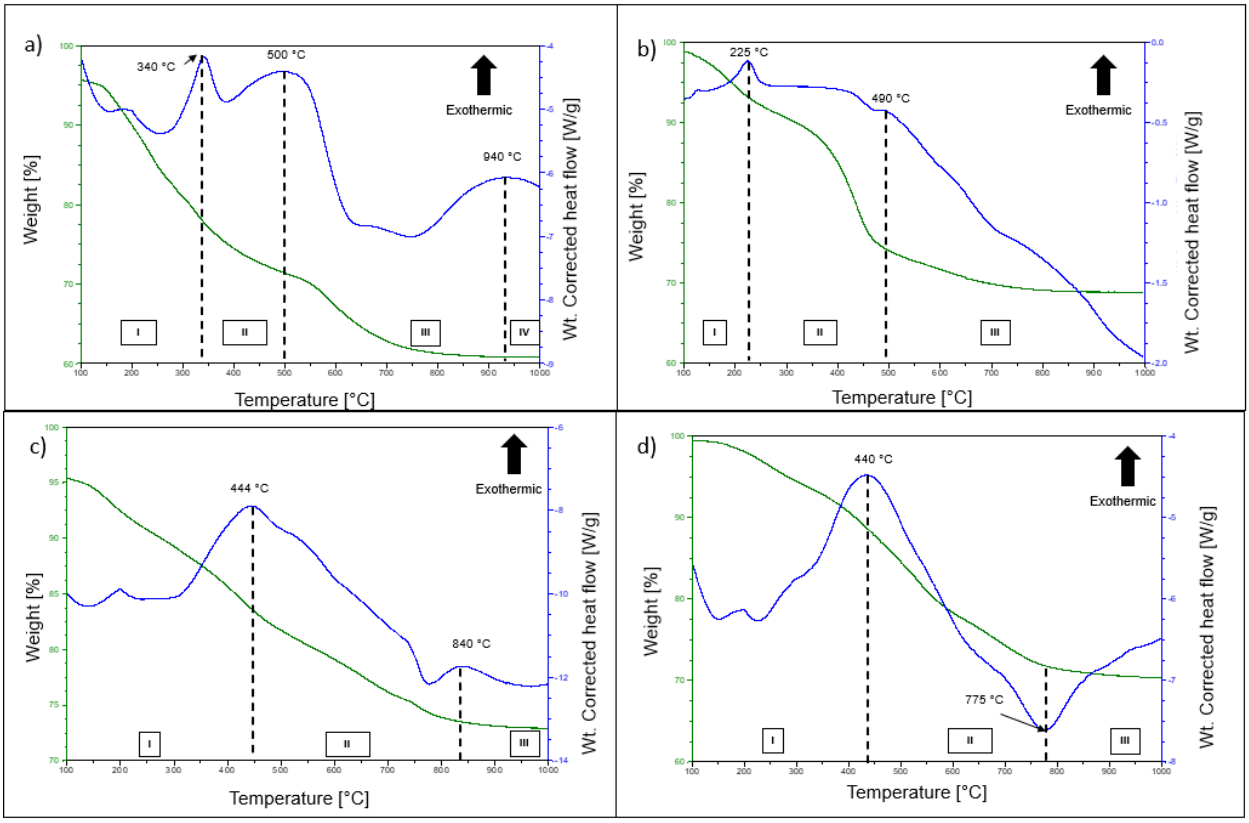

Figure 3.6 Thermogravimetric analysis coupled with differential scanning calorimetry results for (a) Durazane 1800, (b) SMP-10, (c) SMP-500, and (d) SMP-730. The stages of pyrolysis are marked for each polymer

The first stage occurs at low temperatures, up to a few hundred °C, and involves the burning off of side groups, volatiles, and low molecular weight oligomers [84, 143, 150]. In this stage gas is exuded from the polymer, commonly NH_3, H_2, and CH_4 are evolved, but other C_mH_n gasses are possible. Stage II involves thermal cross-linking, where the polymeric chains bond to each other primarily through hydrosilylation reactions, which describes the addition of Si-H bonds across unsaturated bonds, or polyaddition, where individual molecules or polymeric chains bond with each other via independent reactions between functional groups. Since the DZ has N-H bonding transamination, the transfer of α-NH_2, is also possible [84, 143]. At this stage of heating the liquid precursors have become hard resins due to the amount of cross-linking. Continuing to heat the polymer leads to the pyrolysis stage (Stage III) where the backbone of the polymer breaks, after which the elements will form ionic bonds with each other, thus forming

PDCs [85, 143, 151-153]. Pyrolysis also includes the formation of short-range networks, Kumada rearrangements, and further eliminations. The initial ceramics formed through pyrolysis are amorphous, but they can be crystallized through further heating to temperatures exceeding 1000 °C (Stage IV), although for the purposes of MBPP this final step is not needed as the amorphous ceramics are sufficient for enhancing mechanical strength of the composite.

The temperature regime and associated weight loss each polymer are listed in **Table 3.3**, although more polymer-focused research may be needed to narrow down the temperature ranges. Clearly the most weight loss occurs in the first two steps of thermal decomposition, except for the 10wt% loss in the DZ which may be attributed to the high heating rate. Importantly the pyrolysis (Stage III) for each polymer occurs over a temperature range associated with processing molten Al. The yield of each polymer is on the lower end of what is to be expected due to the high heating rate, but within the normal realm of yield [79, 84]. For standard PDC (i.e. not MMNC related) usage higher yields of 70-80% can be achieved with much slower heating rates (<1-10 C/min), which is not suitable for this application [63, 79, 151-153].

3.2.4 Fourier transform infrared analysis

We performed FTIR analysis on polymers heated to different temperatures within the pyrolysis regime, or past the point when pyrolysis should begin as found by the TGA-DSC data, to better understand what would be an ideal temperature for MBPP experiments. As can be seen in the non-normalized data (**Figs. 3.7a**, **3.7c**, **3.8a**, **3.8d**) there is significant amount of complex bonding in the as-received polymers and still some absorption when the samples are heated 500 °C, which was measured to be the start of pyrolysis, but heating the polymers beyond that temperature led to almost flat spectra.

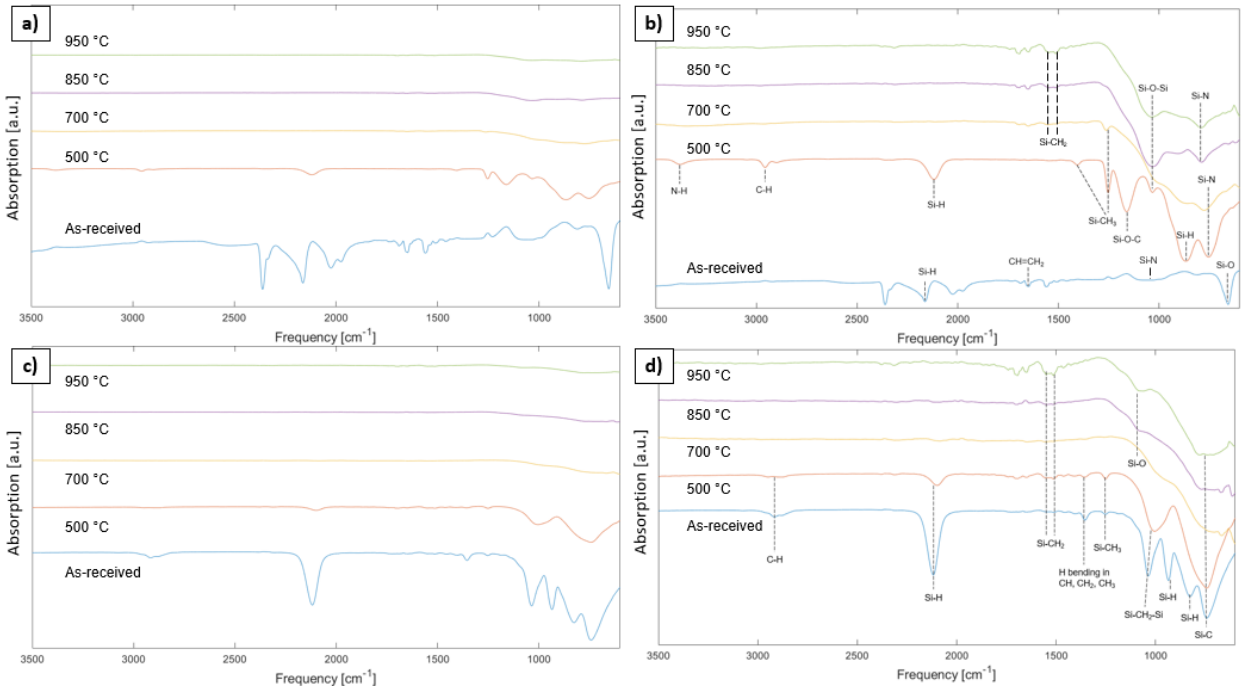

Figure 3.7 (a, c) Not normalized and (b, d) normalized Fourier transform infrared results for Durazane 1800 and SMP-10, respectively

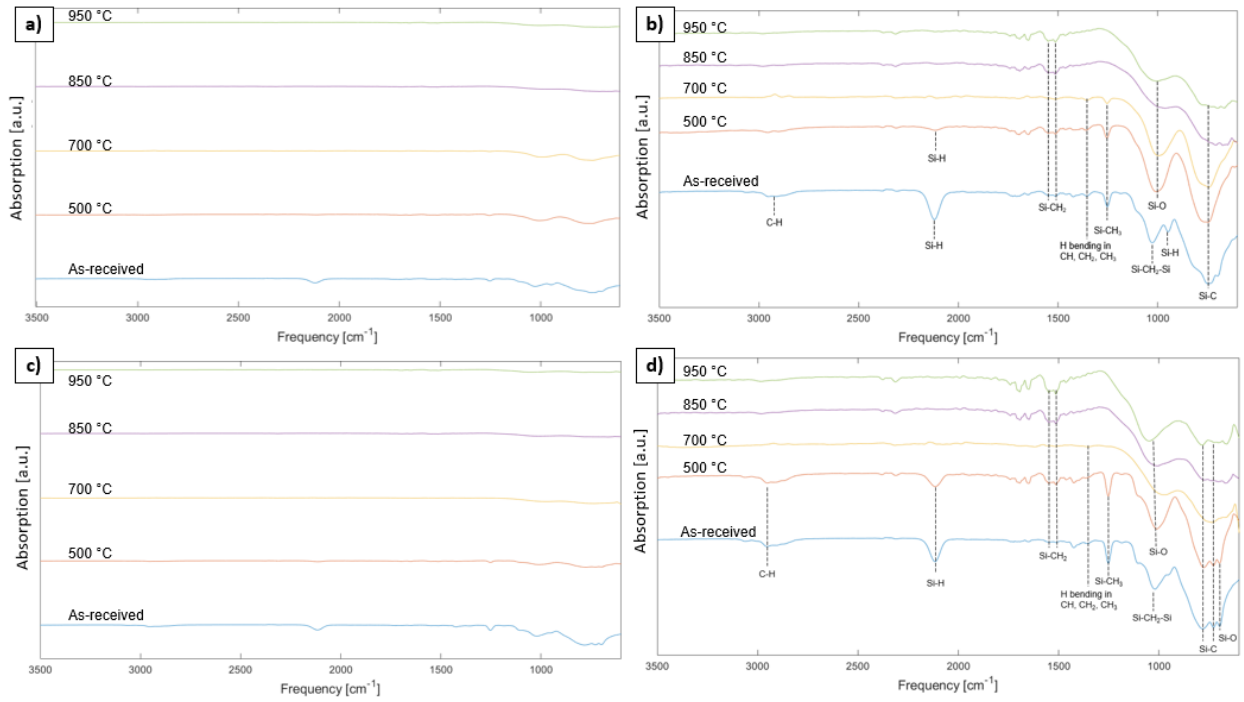

Figure 3.8 Not normalized and (b, d) normalized Fourier transform infrared results for SMP-500 and SMP-730 respectively

The normalized data (**Figs. 3.7b**, **3.7d**, **3.8b**, **3.8d**) makes the peaks of the bonds easier to identify but does not show the extent to which the higher temperature samples have minimal absorption. As-received DZ shows peaks for Si-H (2163 1/cm), $CH=CH_2$ (1650 1/cm), Si-N (1060 1/cm), Si-O (657 1/cm), and a few peaks likely related to proprietary materials. Interestingly the DZ sample heated to 500 °C shows more complex structure likely due to thermal cross-linking and has peaks for N-H (3377 1/cm), C-H (2956 1/cm), Si-H (2115 and 870 1/cm), $Si-CH_2$ (1405 and 1256 1/cm), Si-O-C (1160 1/cm), Si-O-Si (1037 1/cm) and Si-N (756 1/cm). The as-received and 500 °C peaks all match what could be found in the DZ structure [62, 71, 154]. Heating DZ to 700 °C and beyond removes most of the peaks except for Si-O-Si, and Si-N, as expected for samples sufficiently in the pyrolysis temperature regime. $Si-CH_2$ (1550 and 1514 1/cm) is also found in the pyrolyzed samples but is extremely small when viewed in the non-normalized data (**Fig. 3.7a**) and may be due to the testing environment. The reduction in peaks to primarily Si-O-Si and Si-N bonding follows what has been seen in literature for pyrolyzing similar polymers [63, 65, 81, 82, 138, 143, 155, 156]. The FTIR data also speaks to the difficulty of pyrolysis in the presence of oxygen: there were no Si-C or ternary Si-C-N peaks found likely due to the preferential formation of oxides over the formation of complex carbides. The oxygen was likely absorbed into the polymer during experiment setup prior to pyrolysis, although some amount could be from the purified Ar.

The SMP-10 FTIR data shows a similar trend of reduction of peaks, shown in **Fig. 3.7d**: the as-received sample has peaks for C-H (2916 1/cm), Si-H (2114, 937, and 828 1/cm), $Si-CH_2$ (1550 and 1514 1/cm), $Si-CH_3$ (1250 1/cm), $Si-CH_2-Si$ (1036 1/cm), Si-C (741 1/cm) and for H-bending (1355 1/cm) in CH, CH_2, and CH_3 structures, as expected by the polymer's structure [151, 152, 154, 157]. Note that the presence of Si-C bonds in the as-received state is because the

backbone of SMP-10 is composed of Si-C, whereas the backbone of DZ is primarily Si-N, and not an indication that there was SiC ceramic in the starting polymer. Upon heating the polymer to 500 °C much of the structure stays intact, although there is loss of Si-H bonding, and heating further to 700 °C or higher led to a structure primarily of Si-O (1084 1/cm), Si-C (741 1/cm), and Si-CH_2 (1550 and 1514 1/cm). These trends follow what has been shown in literature and indicate that there is essentially only SiC and SiO_2 left after heating beyond 700 °C [64, 77, 86, 151, 152, 156, 158-163].

The other two Starfire polymers have similar FTIR spectra to SMP-10. The normalized data of SMP-500 is shown in **Fig. 3.8**. The as-received polymer has peaks for C-H (2944 1/cm), Si-H (2122 and 947 1/cm), Si-CH_3 (1253 1/cm), Si-CH_2-Si (1025 1/cm), Si-C (745 1/cm), Si-CH_2 (1544 and 1514 1/cm), and for H-bending (1355 1/cm) in CH, CH_2, and CH_3 structures. Upon heating the polymer to 500 °C, and even up to 700 °C, much of the structure stays intact, although there is a loss of Si-H bonding and a transition to Si-O bonding (1000 1/cm). Heating beyond 700 °C resulted in a structure primarily of Si-O and Si-C bonds. SMP-730 results in essentially the same FTIR spectra, although there are two consecutive peaks for Si-C likely due to the more complex nature of the polymer compared to SMP-10 and SMP-500. In its as-received state it has peaks for C-H (2953 1/cm), Si-H (2115 1/cm), Si-CH_3 (1253 1/cm), Si-CH_2-Si (1021 1/cm), Si-C (782 and 731 1/cm), Si-CH_2 (1545 and 1513 1/cm), Si-O (696 1/cm), and for H-bending (1422 1/cm) in CH, CH_2, and CH_3 structures. Again, only Si-O and Si-C are left when heated above 700 °C.

3.2.5 Analysis of pyrolyzed material

To check that pyrolysis was occurring macroscopically we held 50 g of each polymer at 850 °C under Ar for 1 hour. Using the FTIR results alongside the TGA-DSC results we chose

850 °C as a good operating temperature for pyrolyzing both polymers in the MBPP experiments. The resulting materials were clearly PDCs, owing to their black glassy appearance (see **Fig. 3.9**).

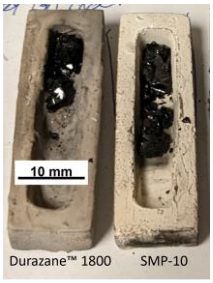

Figure 3.9 Pyrolyzed Durazane 1800 (left) and SMP-10 (right)

The black color is common in PDCs and is related to excess C forming pockets of graphite within the amorphous structure [153, 164-166]. After grinding theses samples into powder, the pyrolyzed PDC samples were analyzed with X-ray diffraction (XRD, Rigaku Smartlab equipped with a D/Tex Ultra 250 detector), from 15-90° operating at 40 kV and 44 mA and a scan speed of 5 °/min. The raw data were analyzed using PDXL software (V2.8.4, Rigaku) then smoothed using a linear regression model in MATLAB with a smoothing window 100 prior to plotting. The XRD results of the pyrolyzed polymers are shown in **Fig. 3.10** with the square root of the intensity values to improve clarity: the DZ (blue line) and SMP-10 (orange line) are completely amorphous as they have no peaks, but the SMP-500 and SMP-730 both show two broad peaks which correspond roughly with SiC and SiO_2.

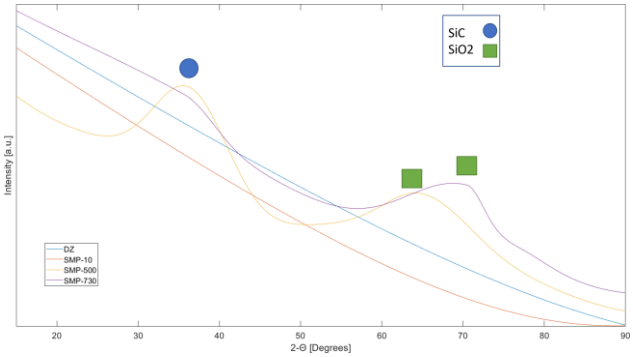

Figure 3.10 X-ray diffraction spectra for polymers pyrolzed at 850 °C

We tested Vickers micro-hardness on these samples (Clark Microhardness Tester, CM-400AT) using a load of 300 gf for the PDCs and a dwell time of 15 seconds. To create samples for hardness tests chunks of the pyrolyzed polymers were mounted in epoxy then ground flat using SiC grinding sheets (340, 600, 1200 grit). All reported microhardness values are an average of 5 tests, excluding outliers. The microhardness values were converted from Vickers Hardness units (HV) to MPa with the following equation:

$$HV_{MPa} = \frac{2F_{load}\sin\left(\frac{136}{2}\right)}{D_1 * D_2} \tag{3.1}$$

Where F_{load} is the force in grams, and D_1 and D_2 are the length (μm) of the diagonals of the indentation. The results of the hardness testing are listed in **Table 3.4**. The hardness measurements of the pyrolyzed polymers match well with what is expected in literature for SiO_2 and amorphous PDCs [65, 66, 157, 167]. The large amount of standard deviation in the DZ and SMP-500 samples is likely from porosity or microcracks locally reducing the hardness of the material. While SMP-500 showed the highest micro-hardness, the SMP-10 showed the lowest amount of deviation in its measurements.

Table 3.4 Results of Vickers Microhardness testing on the polymer derived ceramics

Material	**VH (GPA)**	**Outliers (Gpa)**	**STD (GPA)**
Durazane 1800	6.05	3.63	1.39
SMP-10	7.52	n/a	0.36
SMP-500	9.32	14.17	1.3
SMP-730	5.3	n/a	0.71

Microstructural analysis was done with a MIRA3 Tescan field emission gun scanning electron microscopy (SEM) in secondary electron (SE) mode with an accelerating voltage of 15 kV and beam intensity of 8-10. SEM was performed on PDCs from pyrolyzed DZ and SMP-10, but was not performed on SMP-500 or SMP-730 as their structures were expected to be the

highly similar to that of the pyrolyzed SMP-10. The SEM of the pyrolyzed DZ is shown in **Fig. 3.11a** and that of the pyrolyzed SMP-10 in **Fig. 3.11b**. Both material have clear cracks running through them from shrinkage during pyrolysis, although it is interesting that the pyrolyzed SMP-10 has a secondary phase. Likely of excess C, running through some of the major cracks. SEM proved challenging on these samples due to the extreme amounts of charging, although for the purposes of identification of the phases in future experiments these images were sufficient.

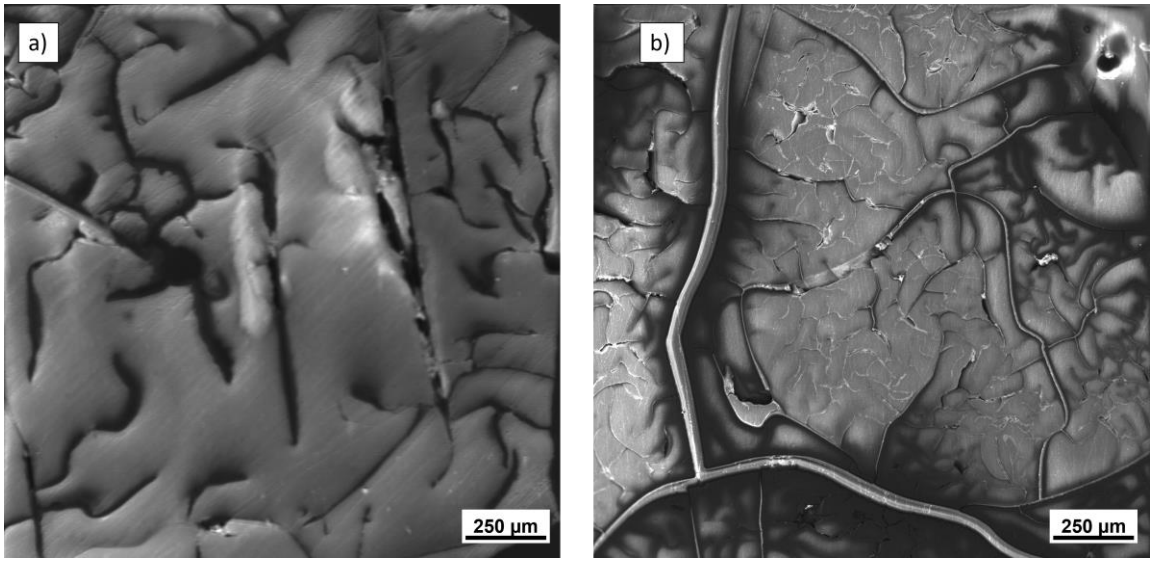

Figure 3.11 SEM images of (a) pyrolyzed Durazane 1800, and (b) pyrolyzed SMP-10

3.3 Metal-based polymer pyrolysis experiments in aluminum

3.3.1 General processing methods and equipment

All MBPP experiments were conducted in either a horizontal tube furnace (Thermoscientific TF55030A-1) or a top-loading crucible furnace (Lindberg/Blue M™, Waltham, MA, model No. 56611) with a Eurotherm EPC3016 controller. Almost all experiments were conducted with a cover gas of Ar (Cryogenic Gasses, Detroit, MI) purified with an oxygen trap (T300-2, Vici Metronics, Poulsbo, WA) prior to contact with the samples. Experiments conducted in the tube furnace were done by placing the samples inside a 1" quartz tube and

having the Ar flow through the tube at a rate of 50 mL/min, then flow out of the tube into an extendable vacuum trunk. Unfortunately, the end-caps used in these experiments were not perfect seals so the prospect of holding an Ar environment throughout the experiment would not have worked, thus a flow of gas was preferred. Specialized aluminum oxide boats were made for these experiments using castable ceramics from Cotronics Corp. (Item 780-1). These boats can be seen in **Fig. 3.9**. On occasion cracks in the boats were filled or fixed with a high-temperature refractory coating (Pyro-Paint™ by Aremco Products Inc., Valley Cottage, NY). Experiments in the horizontal tube furnace primarily used Al powder (30 μm/500 mesh, Alpha Chemicals, Stoughton, MA) as the matrix material, as it made for easier mixing with the polymer precursors and easier placement in the boats. Since the boats were unreachable in the quartz tube the Al powder and polymer had to be mixed at room temperature and were hand mixed until homogeneous. These samples were allowed to furnace cool until it was safe to open the furnace and remove them from the quartz tube, typically <500 °C.

Samples made in the crucible furnace also had a cover gas, although for these experiments the hose of Ar was attached to an Inconel tube that was placed at the mouth of the graphite crucibles. The flow was increased to 100 mL/min due to the higher chance of oxygen exposure, and the vacuum trunk was placed near the mouth of the furnace to catch any fumes from the pyrolysis process. Samples were either allowed to cool in the graphite crucibles or were poured into room-temperature rectangular graphite molds. For experiments in the crucible furnace Al shot was used (99.99%, 2-5 mesh, Belmont Metals) as the matrix basis. The furnace setup allowed for Al to be brought to pyrolysis temperature prior to adding the polymer precursors into the liquid Al.

Experiments in this chapter all used the polymer precursors in their as-received states, although experiments not recorded in this dissertation used thermally cross-linked polymer powder as the reactive addition. For those experiments the as-received polymers were placed in the aluminum oxide boats then heated to sub-pyrolyzing temperatures (200 – 400 °C) with a cover flow of Ar gas. When done the polymers became solid resins which could be ground into a fine powder with mortar and pestle or with a ball mill.

The MBPP samples were analyzed using Vickers Microhardness, XRD, and SEM as outlined in Section 3.2.5. SEM samples were prepared using alumina grinding sheets (340, 600, 1200 grit) followed by monocrystalline diamond suspensions (9, 3, 1 µm, MetaDi by Buehler Ltd., Lake Bluff, IL). Care was taken to ensure no SiC grinding sheets were used with the MBPP samples to avoid any confusion caused by comparing *in situ* SiC particles with SiC particles from grinding sheets embedded in the Al matrix.

3.3.2 Powder-based MMNC experiments

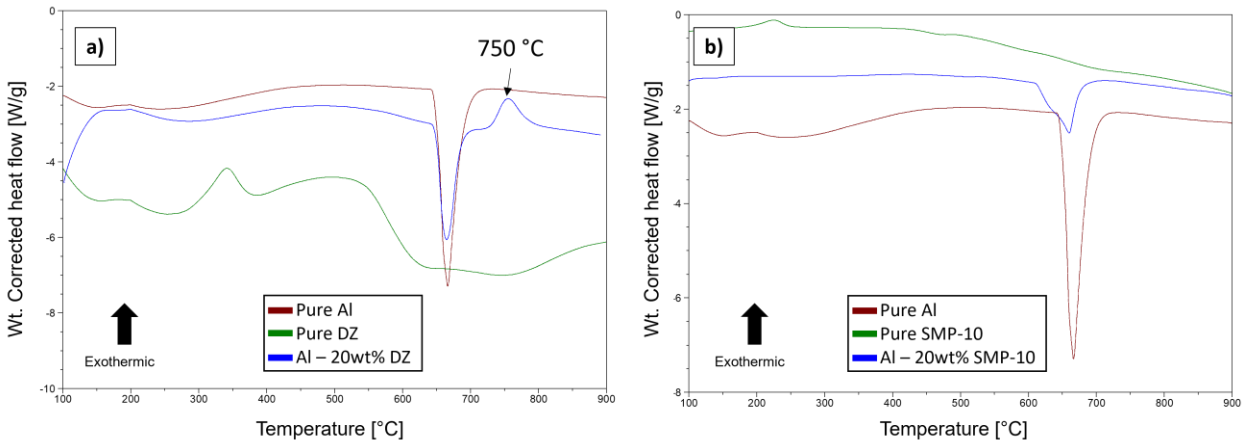

Figure 3.12 Differential scanning calorimetry results for mixtures of Al powder and (a) Durazane 1800 and (b) SMP-10

The most successful MBPP experiments were conducted using Al powder as the basis for the metal matrix using the equipment outlined in Section 3.3.1. We first tested a mixture of Al powder with 20 wt% polymer with DSC, the large amount of polymer was used to see if any extraneous reactions occurred when the polymer decomposed in the presence of Al. **Fig. 3.12a** and **3.12b** show an overlay of the DSC data for pure Al, pure polymer, and the mixture of Al with DZ or SMP-10, respectively. There is a clear peak in the mixture of Al and DZ (**Fig. 3.12a**) at 750 °C that is not found in either the pure DZ or Al DSC scans, which indicates a reaction occurring between the two at that temperature. This is likely caused by the DZ chain fully decomposing and forming a mixture of SiO_2 or Al_2O_3, as both were found in the XRD spectra (**Fig. 3.13**) of similar samples and have exothermic formation enthalpies [168]. The DSC spectrum of Al20SMP does not show any peaks other than one for Al melting, although this peak is shifted and broadened which could be due to some effects caused by the polymer decomposition.

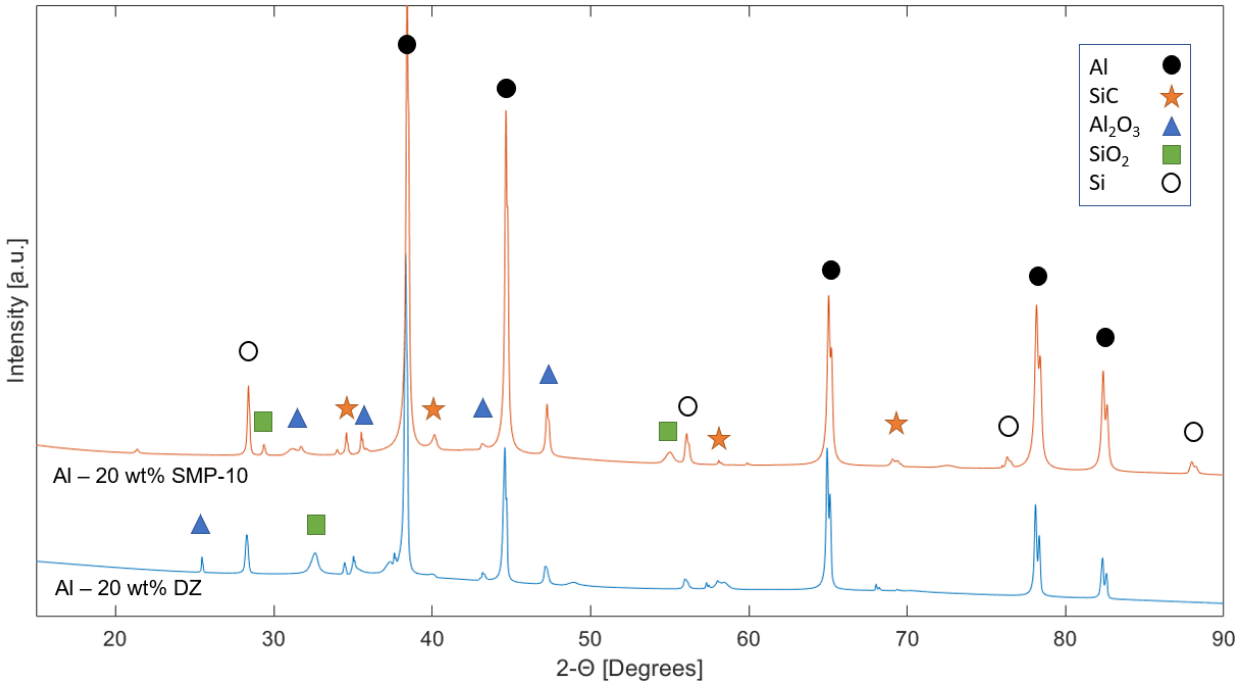

Figure 3.13 X-ray diffraction spectra for pyrolyzed mixtures of Al with SMP-10 (top) and Durazane 1800 (bottom)

The pyrolyzed mixture from the DSC results were analyzed with XRD in **Fig. 3.13**. The Al20DZ sample shows clear peaks for both SiO_2 and Al_2O_3, along with small peaks for SiC and Si, but none for SiCN or SiN. The Al20SMP mixture is fairly similar although it has much stronger peaks for Si and SiC. Interestingly, the XRD spectra for both the pyrolyzed DZ and SMP-10 show no peaks (**Fig. 3.10**), as expected for an amorphous material, which indicates that the presence of Al changes how the polymer pyrolyzes or possibly that there was trapped oxygen between Al powder particles.

To create the MMNC samples the Al powder was first sonicated in acetone then separated using vacuum assisted filtering with a 0.2 μm Whatman™ nylon membrane. The cleaned Al powder was hand mixed with the liquid as-received polymers at room temperature, then the mixture placed in an alumina crucible and heated to 850 °C for 1 hour. The crucible sat inside a quartz tube which had an Ar cover gas flow of 50 CC/min to minimize oxidation and burning of the polymer.

For melt experiments the projected volume fraction (V_f^{PDC}) of the ceramic from the liquid polymer precursor was estimated with the following formula from Castellan et al. [155]:

$$V_f^{PDC} = x_{yield} \frac{\rho_{Al}}{\rho_{PDC}} W_f^{polymer} \quad (3.2)$$

Where x_{yield} is the ceramic yield of the precursor, which was experimentally determined to be 60 wt% for DZ and 70 wt% for SMP-10, ρ_{PDC} and ρ_{Al} are the density of the PDC particles and the Al melt, 1 and 2.7 g/cm^3 respectively, and $W_f^{polymer}$ was the given weight fraction of the polymer added to the Al. Melt experiments used 0, 5, 10, and 15 wt% polymer, or 9.5, 19, 28 vol% SMP-10 and 8.7, 17.6, and 26.3 vol% DZ. Separate Al-20wt% as-received polymer samples were made with the same technique and were used solely for analyzing if and how the

metal would react with the polymer during pyrolysis via TGA-DSC. A summary of samples and their shorthand notation can be found in **Table 3.5**.

Table 3.5 Shorthand notation for metal-based polymer pyrolysis samples

Material	Name
Durazane 1800™	DZ
StarPCS™ SMP-10	SMP10
Al – 5 wt% Durazane 1800™	Al5DZ
Al – 10 wt% Durazane 1800™	Al10DZ
Al – 15 wt% Durazane 1800™	Al15DZ
Al – 20 wt% Durazane 1800™	Al20DZ
Al – 5 wt% SMP-10	Al5SMP
Al – 10 wt% SMP-10	Al10SMP
Al – 15 wt% SMP-10	Al15SMP
Al – 20 wt% SMP-10	Al20SMP

The bulk microstructure of all of the MMNC samples show significant porosity (**Figs. 3.14a, 3.15a, 3.16a, 3.17a, 3.18a**) with most pores ranging from a few μm, while a few are hundreds μm across. This porosity is clearly caused by two separate reasons: the porosity is mainly caused by the gas exuded from the polymer during decomposition, similar to how metallic foams can be made [169]. Second, even with significant cleaning beforehand there is evidence for much of the Al powder having an oxide skin preventing liquid Al coalescing into a bulk material. Looking within the porous regions of the Al5DZ sample in the BSE micrograph of **Fig. 3.14b** there are clearly PDC particles: the EDS map in **Fig. 3.14d** shows a large amount of Si, C, N, and O around the different pores in the region which indicates that the formed PDCs have dotted the outside surface of the Al matrix. Furthermore, imaging these samples in SE mode reveals that some of what appears to be porosity in BSE imaging is in fact a large amount of non-conducting material from the pyrolyzed polymers. This material was found in both Al-DZ and Al-SMP samples and shows up as the bright spots in **Figs. 3.15a**, **3.18a**, and **3.19a**. Due to

the amount of charging that occurred from this material it was difficult to identify via SEM but quick EDS scans showed it having large amounts of C and O.

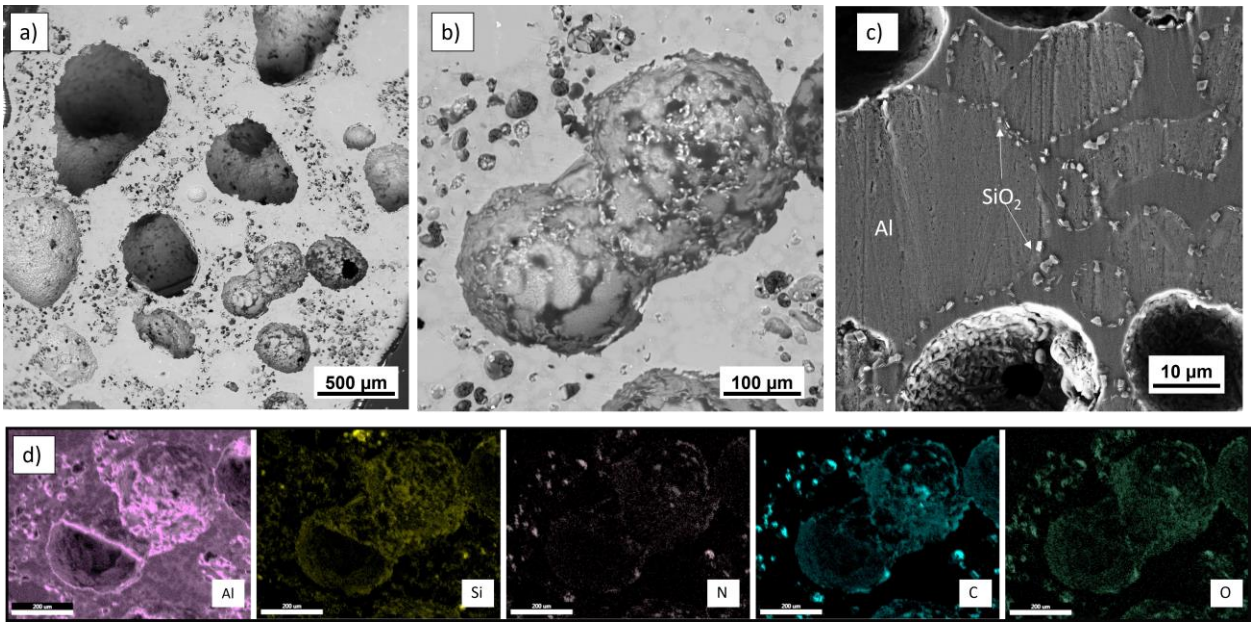

Figure 3.15 (a) SEM of Al-Al-5wt% Durazane 1800. (b) Close up of a pore showing particles in its surface. (c) SiO2 particles surrounding an Al grain. (d) EDS spectra of the sample showing Al, Si, N, C, and O.

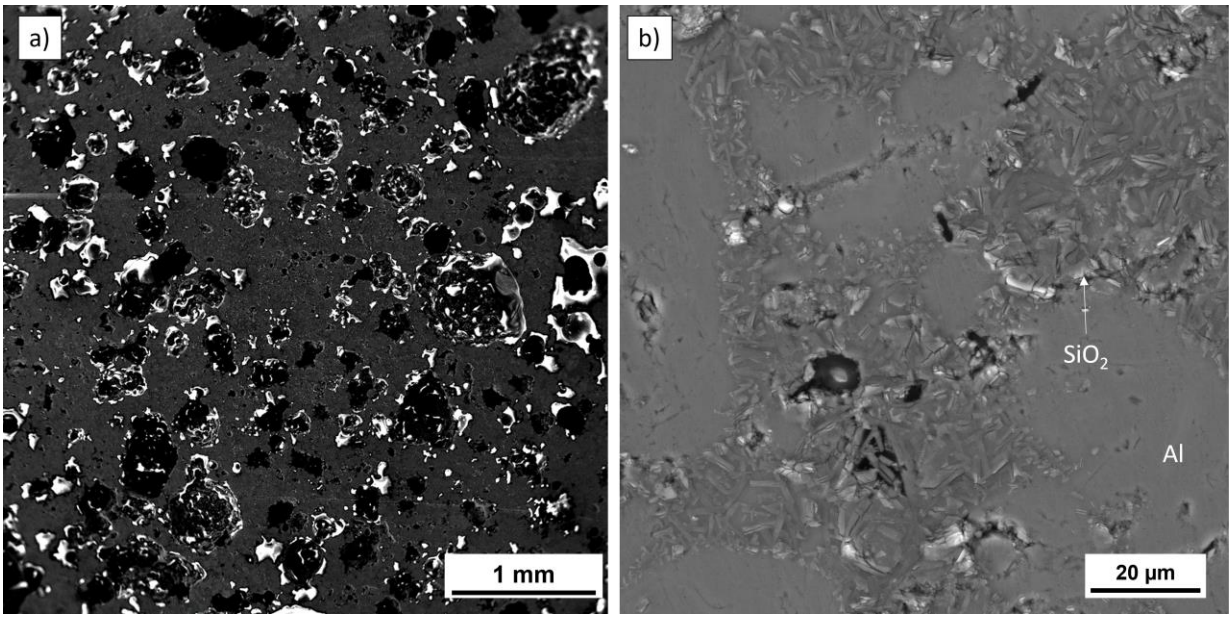

Figure 3.14 (a) SEM of Al-10wt% Durazane 1800, showing the general microstructure. (b) SEM of the needle-like SiO2 particles found in the sample.

Looking at regions between pores for the Al-DZ samples gives more insight into how the MBPP process occurred. In the Al5DZ sample shown in **Fig. 3.14c** there are clear regions of Al that were the original Al powder dotted by blocky SiO_2 particles along their edges. Using the oxide particles as boundaries we found the Al grains to be 26.4 μm $\pm$ 8.4, meaning that they are essentially the same size as the starting powder. The oxide particles themselves were 0.87 μm $\pm$ 0.29 and showed good dispersion around the matrix as well as inside the porous regions. Increasing the amount of DZ in the starting mixture led to an increase in the amount of SiO_2 particles in the microstructure, as shown in **Figs. 3.15b** and **3.16b**, but did not significantly change their sizes. The Al15DZ sample also showed regions of pure Si partially surrounding some of the Al, shown as the light gray regions in **Fig. 3.16b**, a feature which is likely in the other samples but hidden behind the SiO_2 particles. Surprisingly there were also large regions of the MMNCs that did not contain any porosity but contained a significant amount of oxide particles (**Fig. 3.16a**). We did not find significant amount of SiC particles in these samples.

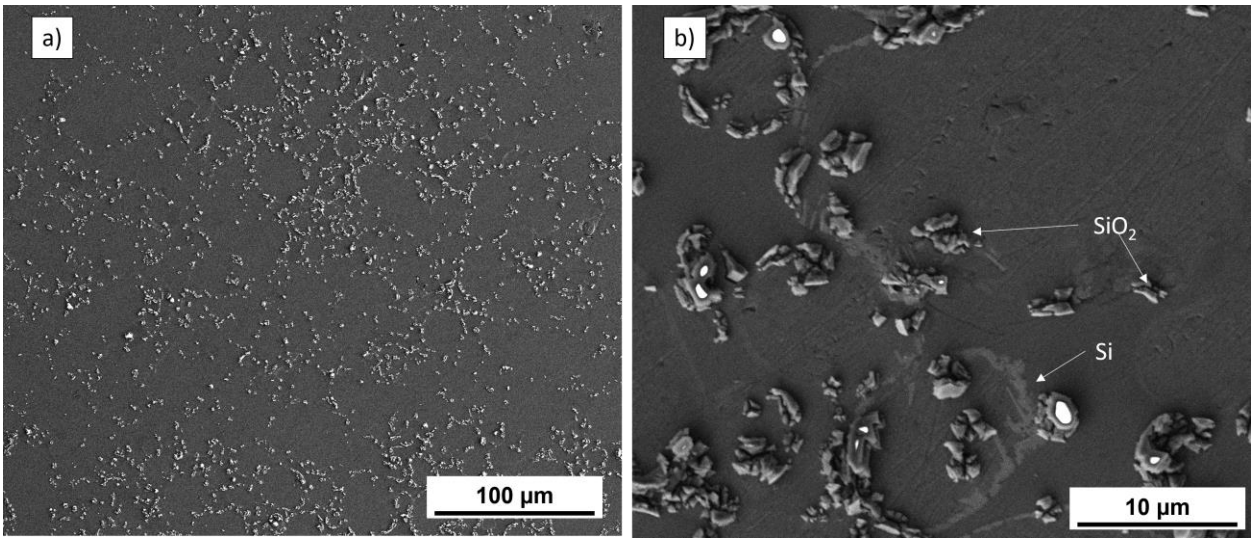

Figure 3.16 (a) SEM of Al-15wt% Durazane 1800, showing the general microstructure. (b) SEM of the blocky SiO2 particles found in the sample and Si-rich regions.

The Al-SMP samples had similar microstructure to the Al-DZ samples including porosity and unhomogenized Al powder, but with significantly different reinforcement particles. Instead

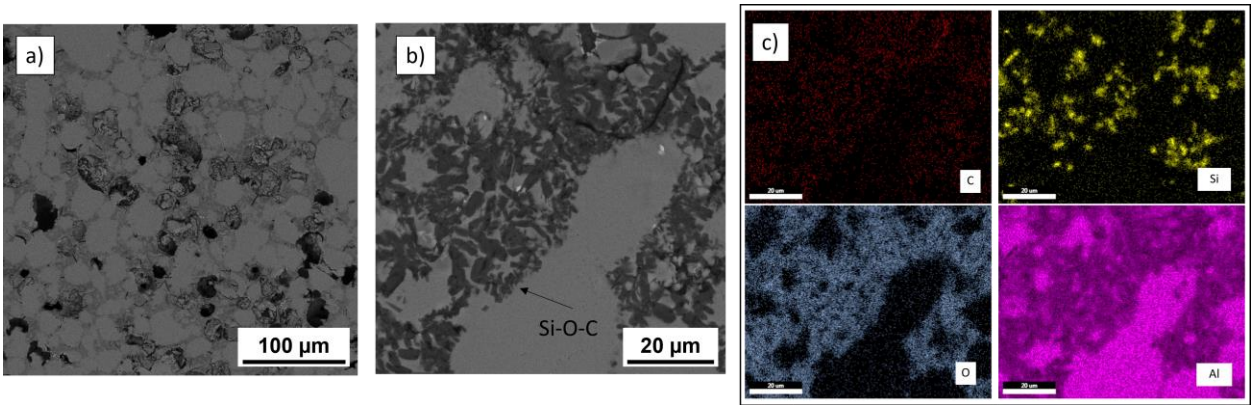

Figure 3.17 (a) SEM of the Al-5wt% SMP-10 microstructure. (b) A closer view of the microstructure showing large amounts of an Si-O-C phase. (c) EDS spectra of 8b showing in clockwise C, Si, O, and Al.

of blocky SiO_2 particles there are a large amount of needle-like Si-C-O, which appear as dark regions in the BSE image of **Fig. 3.18b** but as bright needles in the SE micrographs of **Figs. 3.17b**, **3.19b**, and **3.19c**. An EDS map of the particles shows the presence of Si, O, and C (**Fig. 3.17c**), and spot EDS on the particles verified them generally as an inhomogeneous combination of Si, C, and O. These particles are smaller than those made with DZ, ranging from 0.1 – 0.5 µm thick and 0.15 – 3 µm long. There were some regions that also had SiO_2 particles, blocks of C, and micrometer-sized SiC particles (**Figs. 3.17a** and **3.19c**). The Al-SMP samples were more likely to have regions of Si dispersed in the Al matrix, which are the lighter gray regions in **Fig. 3.19c** and the enhanced contrast inset in **Fig. 3.19b**.

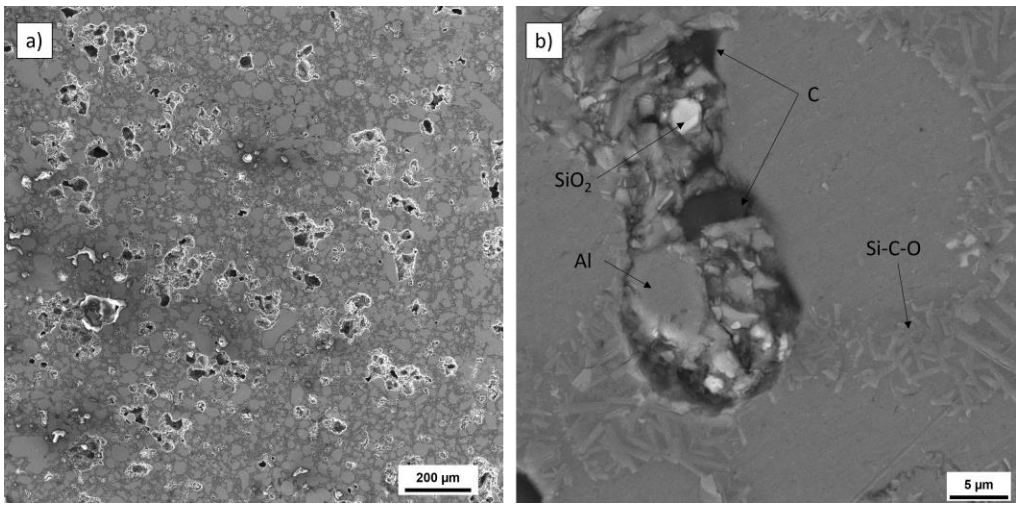

Figure 3.18 (a) SEM of the Al-10wt% SMP-10 microstructure. (b) A closer view of the microstructure showing large amounts of an Si-O-C phase as well as partilces of SiO2 and chunks of C.

The separation of the C-rich and Si-rich regions clearly shows that the pyrolysis process is affected by the presence of the Al matrix and shows that improvements to the MBPP process can be made. More SiC could be produced by varying processing parameters such as the amount of polymer used, the state of the polymer (as-received or cross-linked into a resin), and the pyrolyzing temperature, or by the way the polymer is incorporated into the Al matrix.

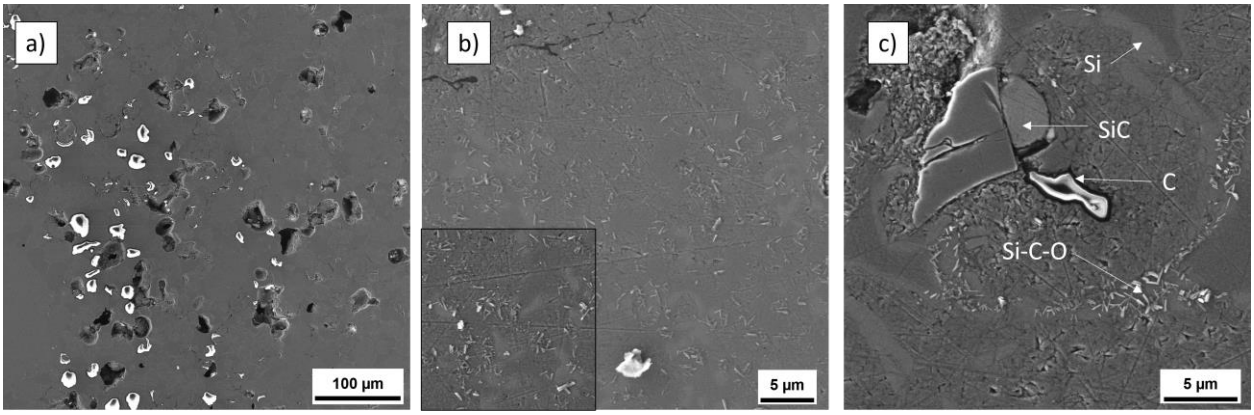

Figure 3.19 (a) SEM of the Al-15wt% SMP-10 microstructure. (b) A closer view of the microstructure showing large amounts of an Si-O-C phase, the inset corner has enhanced contrast to show the Si-rich regions. (c)SEM of an SiC particle along with SiCO and excess C.

3.3.3 Mechanical properties of powder-based MBPP samples

The Vickers Microhardness results shown in **Table 3.6** show a general trend that increasing the amount of polymeric precursor increases the hardness of the materials, with the exception of Al5SMP which decreased in hardness compared to pure Al. Al15DZ and Al15SMP had the highest VH values of 955 and 473 MPa, respectively, showing an increase of 350% and 122% compared with pure Al powder. The samples with higher polymer content also showed a few areas of extreme hardness, on the order of GPA, which were clearly regions with excess amounts of ceramic. The hardness measurements of the pyrolyzed polymers match well with what is expected in literature for SiO_2 and amorphous PDCs [65, 66, 157, 167]. Due to the porosity in the samples reliable tension or compression measurements could not be made.

Table 3.6 Vickers Microhardness values of the powder metal-based polymer pyrolysis samples

Material	VH (MPa)
Al powder	213 ± 16
Al – 5 wt% DZ	243 ± 42
Al – 10 wt% DZ	364 ± 70
Al – 15 wt% DZ	955 ± 120 (Outlier of 5019)
Al – 5 wt% SMP-10	170 ± 51
Al – 10 wt% SMP-10	343 ± 68
Al – 15 wt% SMP-10	473 ± 29 (Outlier of 1246)
Pyrolyzed DZ	6050 ± 1390
Pyrolyzed SMP-10	7515 ± 360

3.3.4 Larger-scale MBPP experiments

Multiple attempts were made at creating more large-scale MBPP samples by using the crucible furnace as outlined in Section 3.3.1. Generally, these experiments were done by bringing the Al melt to pyrolyzing temperatures (850+ °C) then adding packets of polymer wrapped in Al foil (AFI UHV Aluminum foil, All Foils, Strongsville, OH) into the melt. These experiments had varied success, although there were a few major concerns prevalent in most of them.

Since the polymer was heated rapidly to the pyrolysis temperature it typically generated a flame from the crucible when added. Although the trunk kept the gasses and flame byproducts safely contained, the flame itself made it difficult to continue processing the material (i.e. ultrasonic mixing, stirring the melt) during the pyrolysis process.

There was also difficulty caused by lack of wetting of the polymer precursor and the as-formed ceramics in the bulk experiments. In the powder experiments the Al powder and polymer could be manually mixed and ensure proper dispersion of the polymer and some amount of wetting between the phases, but the abrupt pyrolysis of the large-scale experiments did not allow this or any other type of mixing to occur. These issues could be worked out with further testing

of processing parameters, or by altering the precursor somehow (e.g. sputtering polymer powder with metal), although for the purposes of this dissertation those steps were not pursued.

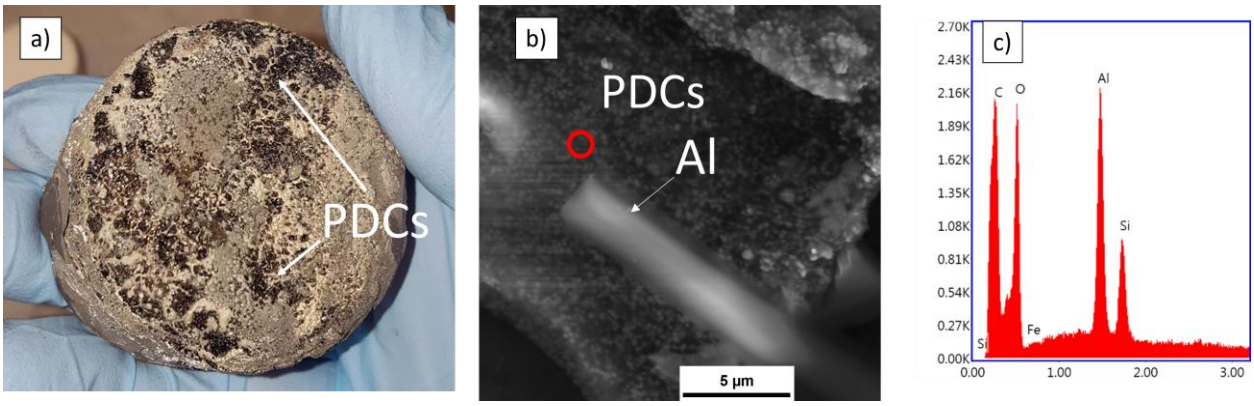

Figure 3.20 (a) Photograph of bulk MBPP sample, where the black regions are polymer derived ceramics, (b) SEM image of the bottom of the sample showing Al and PDCs (c) EDS spectra from the red circle in (b) showing strong peaks for C, O, Al, and Si

Fig. 3.20a is a picture of the bulk Al-MBPP sample made with Durazane 1800, and **Fig. 3.20b** is an SEM micrograph of one of those black sections. The black regions on the bottom are PDCs that formed within the Al, as demonstrated by the EDS histogram showing strong peaks for Si, C, and O (**Fig. 3.20c**), but settled to the bottom of the sample. **Fig. 3.21a** is an SEM micrograph of the Al bulk which has a large amount of PDC material completely inhomogeneous from the Al matrix. Zooming in on the bulk PDC material reveals small needle-like particles similar to those in **Figs. 3.18** and **3.19**. Seeing the large regions of PDC phase made via MBPP in a bulk Al sample gives credibility to the potential usefulness of the method, but clearly there is more work to be done for it to be considered commercially viable in large melts. Based on literature for Mg and Cu MMNCs it is possible to create much smaller PDCs within a metal matrix via MBPP, although much work must be done for refining the method [50, 84, 150, 155, 170-177].

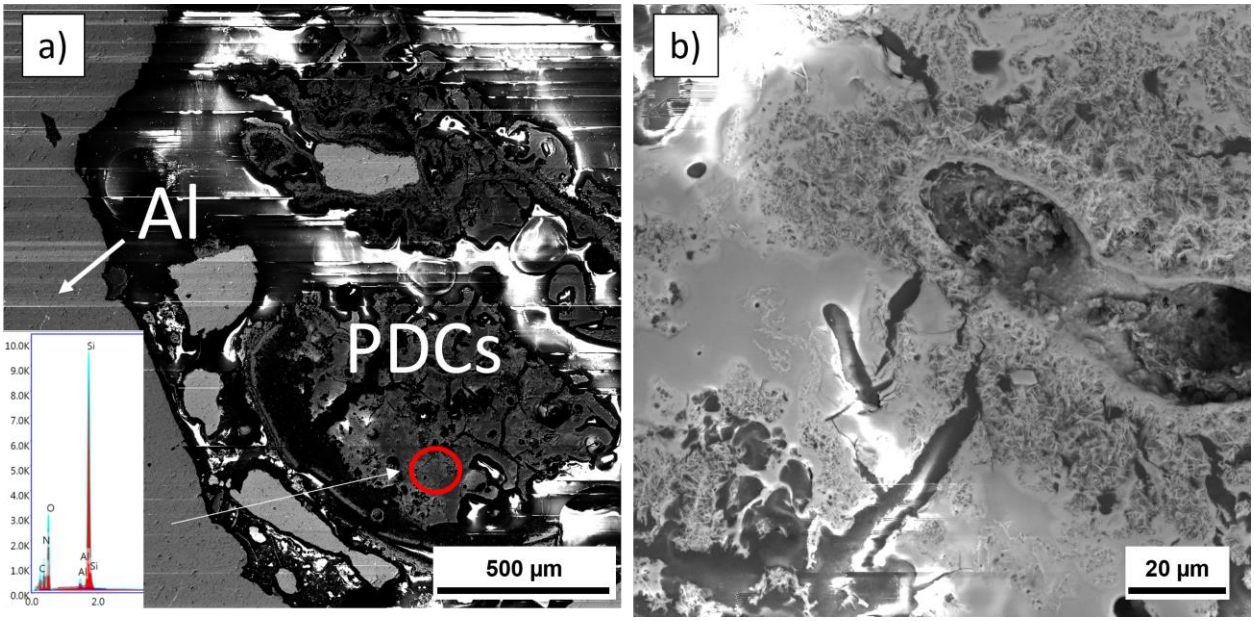

Figure 3.21 (a) SEM of inhomogeneous polymer derived ceramics within the Al matrix, (b) SEM image with increased magnification on the ceramic phase shows needle-like particles on the surface

3.4 Friction stir processing of Cu for precursor polymer incorporation

3.4.1 Motivation

In addition to the Al-melt experiments for MBPP processing, Cu-SiC MMNCs were made via friction stir processing (FSP) following closely the methodologies found in [50, 172]. FSP was chosen to test if we could mechanically mix unpyrolyzed polymer into a solid metal matrix to later control the pyrolysis inside the solid matrix. Since Cu has a melting point (T_m = 1,084.6 °C) beyond the pyrolysis temperature of the polymers pyrolysis could occur within a solid, and therefore less reactive, matrix if the precursor is properly mixed into it.

These experiments were done specifically to try and capture the polymer pyrolysis occurring *in situ* using synchrotron-based X-ray radiography (XRR) at the Advanced Photon Source (APS) beamline 2-BM at Argonne National Lab. Al could not be used for these experiments for two reasons. First, the attenuation coefficient of Al and Si are so similar that

there would not be enough contrast between Al and any Si-rich phases from the polymer. Second, the melting temperature of Al (T_m = 660 °C) is so far below the pyrolysis temperature that there was concern the oxide skin on an Al foil sample would not be able to prevent the sample from collapsing during the experiment.

3.4.2 Experimental methods

Durazane 1800 (DZ) was chosen as the precursor polymer for these experiments, as we had the most experience thermally cross-linking it into a resin compared with the other precursors. The liquid DZ was thermally cross-linked at 300 °C under an Ar cover gas for 1 hour, then the hard resin was turned into a powder using mortar and pestle. Care was taken to place the powder in a sealed glass jar prior to experimentation to prevent further absorption of oxygen, although in the resin state it is less reactive with air than in the liquid state [136, 143]. Cu plates (99.9%, McMaster-Carr) measuring 4x24x0.25 inches (101.6x609.6x6.35 mm) were used as the matrix material. A series of holes were drilled into the Cu plate to be filled with polymer powder and act material wells during FSP. The holes were all 1.7 mm in diameter, had a depth of 0.5 mm, and were drilled either in an alternating fashion (**Fig. 3.22a**, hole pattern 1) or in a single line (**Fig. 3.22a**, hole pattern 2) along the expected weld path. A schematic of the FSP setup can be seen in **Fig. 3.22a**.

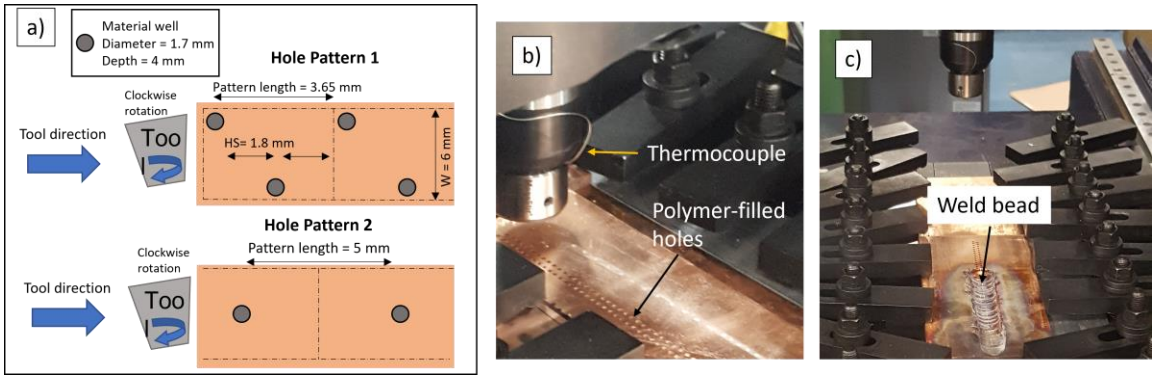

Figure 3.22 (a) Two different hole patterns used for introducing polymer powder into the Cu matrix via FSP, (b) FSP setup with thermocouple attached to the tool head (c) Post-FSP sample

A friction stir welder (Model RM7 2017, Bond Technologies, Inc., Elkhart, IN) was used to incorporate the polymer into the Cu matrix. A steel tool with pin length of 5.7 mm and diameter of 8 mm was used, and it was tilted 0.5° away from the travel direction to improve the force delivered to the sample. The tool was rotated at 1000 RPM in a clockwise rotation to push the polymer material into the Cu matrix, and had a transverse travel speed of 25 mm/min. A thermocouple was attached to measure the temperature of the tip during FSP. A baseplate of pure Cu was placed under the welding sample to both prevent any contamination from the equipment workbench and to prevent welding the Cu to the FSP machine if the weld depth exceeded the Cu plate thickness. Two FSP experiments were done following the two different hole patterns drilled into Cu, for simplicity Cu-1 will refer to the alternating pattern and Cu-2 will refer to the line of holes, as shown schematically in **Fig. 3.22a**. Pictures of the FSP setup before and after the experiment are in **Fig. 3.22b** and **3.22c**, respectively. After the FSP experiments metallographic samples were sectioned from the weld bead, some of which were analyzed as-made and others were annealed in air at 1000 °C for one hour in order to test the *in-situ* pyrolysis of any mixed in polymer. The samples were prepared for imaging with the same method as outline in Section 3.3.1.

3.4.3 Characterizing techniques

The Cu samples were characterized using a Tescan MIRA3 FEG SEM operating at an accelerating voltage of 5-10 kV and a beam intensity of 8-15, operating in secondary electron (SE) imaging mode. An EDAX energy dispersive spectroscopy (EDS) system integrated with the SEM was used for localized chemical identification of particles and secondary phase precipitates. Vickers Microhardness data was measured with a Clark 400AT Microhardness

Tester using a 15 s dwell time and a 200 g load. 5 measurements were taken per sample. Two samples, one from the as-made and one from material annealed at 1000 °C, were ground into small rods and were then analyzed with µCT (Zeiss Xradia Versa 520 3D X-ray Microscope) operating in absorption mode, with an optical magnification of 40x, a source energy and current of 40kV and 75 µA, respectively, exposure time of 12s, and a voxel size of 0.33 µm.

XRR samples were prepared by first cutting thin slices of the as-made Cu composite (1x1x0.5 cm) using a 3 inch wafering blade and a low-speed saw (TechCut4™ by Allied High Tech Products, Inc.) in Professor Amit Misra's lab (University of Michigan Material Science and Engineering department), with the aim of capturing un-pyrolyzed polymer within the sample. The samples were then thinned to a foil of <50 µm thickness using a Gatan disc grinder (Gatan, Inc.) on 1200 grit SiC paper. The Cu foils were sandwiched between two square quartz (SiO_2) coverslips, each 100 µm thick and the edges of the assembly were coated with a high temperature-resistant Al_2O_3 thermal paste to ensure stability of the assembly during reaction. Dimensions of the sample sandwich assembly varied but were all <8 mm in width to fit inside the resistance furnace assembly available at the beamline.

A monochromatic X-ray beam operating at 20 keV was focused on the samples. The X-rays were converted to visible light using a 25 µm thick LuAG:Ce scintillator, then images were collected using a FLIR Oryx CCD camera with a 5x magnifying objective lens and an exposure time of 200 ms. This setup resulted in a 1689 x 1413 μm^2 field-of-view (FOV) and a pixel resolution of 0.69^2 μm^2. For pyrolysis experiments the furnace was lowered onto the samples and equilibrated at 650 °C prior to imaging. Once imaging began the furnace was given a heating rate of 10 °C/min to 950 °C, so radiographs were collected for approximately 30 minutes per

experiment. The radiographs were processed by normalization using dark and white-field images, then a reference image was subtracted from each image to remove noise.

3.4.4 Microstructural characterization and discussion

The first FSP experiment with the holes following pattern 1 (**Fig. 3.22a**) wound up snapping the FSP tool tip: the alternating holes led to a significant amount of chatter in the tip which eventually led to it being broken and left in the Cu bulk. There was some chatter in the Cu-2 sample, but reducing the amount of holes significantly prevented a similar problem from occurring. Thus, there was likely far less polymer introduced into either of the samples: in Cu-1 the material was not mixed in efficiently due to the chatter of the tool and in Cu-2 the reduction of the amount of holes inevitably reduced the amount of polymer available for MBPP processing.

The thermocouple connected to the FSP tool measured a max temperature of 650 °C, meaning that some amount of polymer, perhaps the smallest particles, likely pyrolyzed when it was mixed into the Cu. This temperature regime is consistent with the literature of using FSP to mix polymer into Cu [93, 172]. However, as this temperature is at the low end of the pyrolysis temperature regime for Durazane 1800, a secondary pyrolysis step was needed to complete the composite.

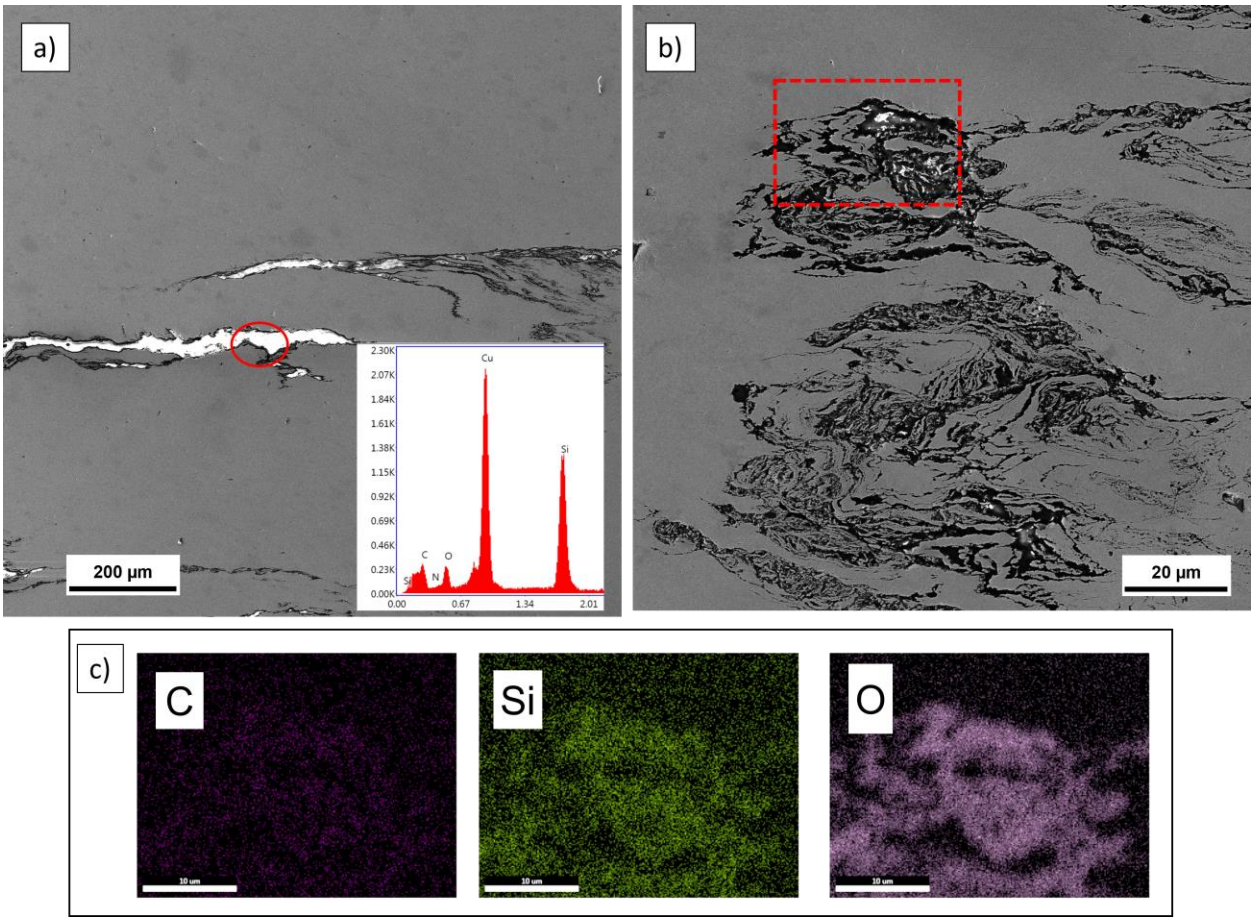

Figure 3.23 (a, b) Sample SEM micrographs showing polymer material mixed into the Cu matrix from friction stir processing, (c) EDS map of C, Si, and O for the boxed region in (b)

The microstructure of an unannealed Cu-2 FSP sample can be seen in **Figs. 3.23a** and **3.23b**, where the complex, curving structure is indicative of mixing via FSP [93, 172]. EDS scans on the black curving whisps (**Fig 3.23c**) picked up large amounts of Si, O, and some C, verifying that they are indeed material from the polymer mixed into the Cu matrix. These regions were not well dispersed throughout the sample and were only within a small portion of the weld bead. The poor mixing is likely due to doing a single FSP pass instead of multiple passes, as is often done for FSP [60, 178-181]. The annealed sample showed a series of pores seemingly along the weld path direction. These pores can be seen in **Fig. 3.24** in the µCT image (**Fig 3.24a**) and the SEM image (**Fig 3.24b**). A magnified image of the pore (**Fig 3.24c**) does not reveal any obvious particles formed, although there is slight charging from one of the porous regions,

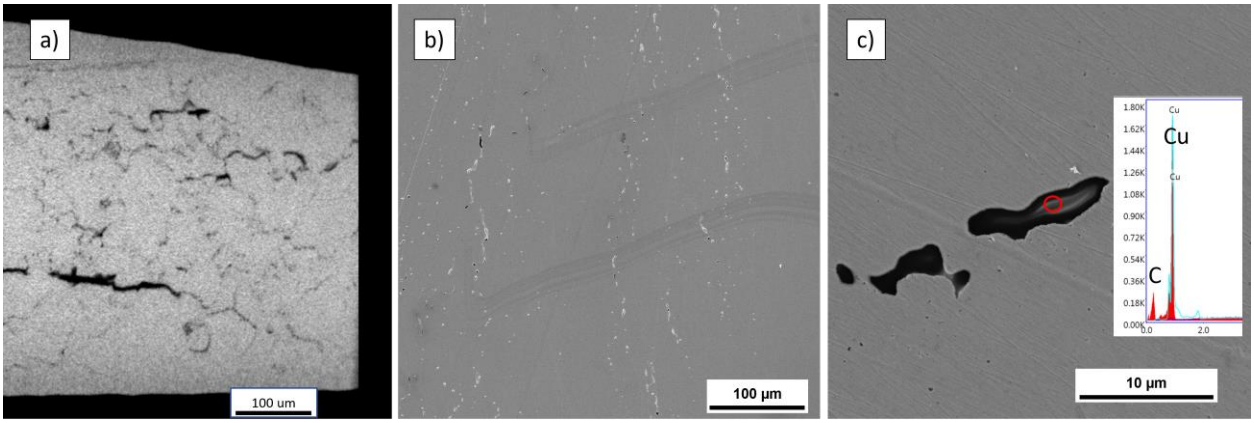

Figure 3.24 (a) A cross-section image from the µCT scan (b) SEM micrograph of the pores found in the Cu-FSP sample, (c) Magnified view of one of the porous regions

indicating that there is material in within it. Spot EDS shows some amount of C, but no Si, suggesting that the pyrolyzed material did not form carbide but instead regions of C throughout the sample.

Unfortunately, the XRR experiments did not help illuminate the matter. The attenuation contrast between the Cu matrix and the polymers or Si-based ceramics should have been sufficient to distinguish the phases: the Si in the polymer and in the ceramics would have been darker than the Cu matrix, regardless of the form, although the carbides should be slightly brighter than the polymer due to the loss of C and H. Prior to heating the samples up it was unclear if there were regions of unpyrolyzed polymeric material within the Cu matrix despite taking the material from where the SEM samples were taken. As the samples were heated, they showed a significant amount of activity through the growth then disappearance of dark regions, as can be seen in **Fig. 3.25.**

A macroscopic image of the XRR sample taken after the experiment can be seen in **Fig. 3.26a**. It should be noted that most of the sample fit within the FOV of the XRR imaging, so almost anything found in SEM would have been seen in the synchrotron experiments. The sample was not ground or polished, but was instead imaged as-is after removing it from the quartz slides. Post-mortem SEM of the XRR samples showed that the samples had a skin of

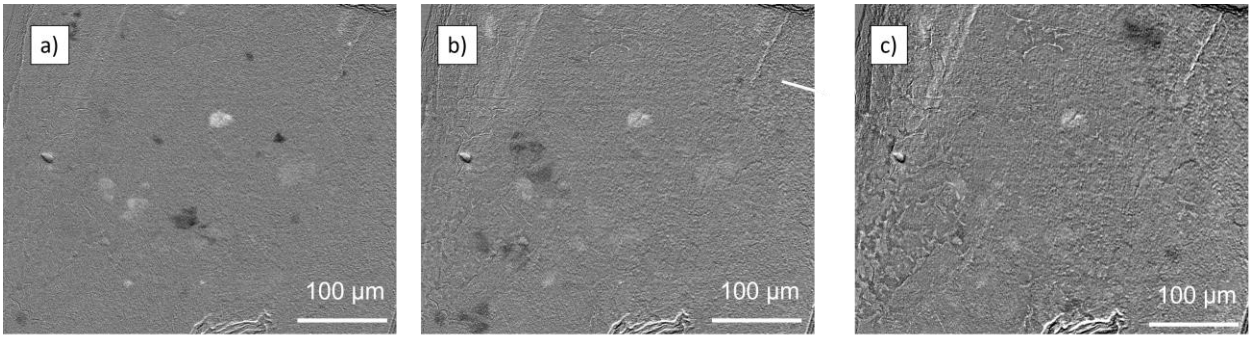

Figure 3.25 Flat-field corrected radiographs depicting various time steps while heating the Cu-FSP sample

copper oxide (**Fig. 3.26b**) with only a few regions of Si-based material, as identified through EDS mapping (**Fig. 3.26c** and **3.26d**). Since SEM is only a surface level technique it was difficult to find any matching phases or structures with the dark regions identified in XRR, although it is possible that the Si-rich phases found in **Fig. 3.26c** correlate with one of the dark regions.

Our initial thought was that these dark regions represented the polymer particles expanding slightly, exuding gas, then pyrolyzing and shrinking into SiC particles, all of which are normal for the pyrolysis process [80, 85, 143]. If this was the case, there are a few corollary hypotheses. First, the starting polymer particles were smaller than the resolution of the XRR (0.69^2 µm^2 per pixel), thus making them indistinguishable from the Cu matrix. Second, the pressure from the exuded gas and expanding polymer are enough to generate porosity in the heated Cu matrix. Third, the final shrinkage of the polymer to the PDC leads to particles that are once again smaller than the XRR spatial resolution.

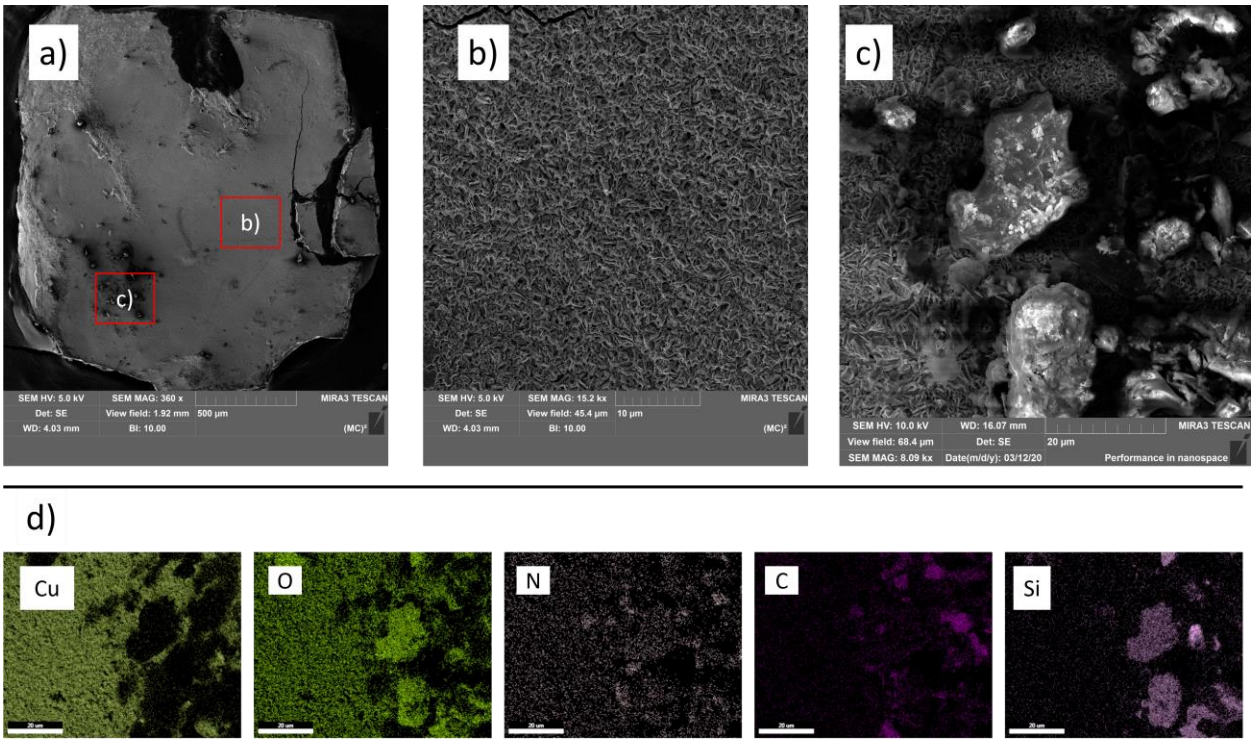

Figure 3.26 (a) Zoomed out SEM image of the synchrotron-based X-ray radiography sample after it underwent the heating experiment, (b) Magnified view of the surface at box b, (c) Magnified view of the surface at box c, (d) EDS map of Cu, O, N, C, and Si of region in (c)

There are a few clear problems with these hypotheses. First and foremost, based on SEM analysis (**Figs. 3.23** and **3.24**) the size of the polymer material regions and the formed PDCs should have greatly exceeded the spatial resolution of the XRR, meaning that the polymer regions should have been visible at the start of and throughout the experiment, regardless of where they were in the sample. Second, even if the pyrolysis process was able to form porosity in the Cu matrix, there should have been a lasting impact from the porosity, meaning that the porous regions should have a sustained change in intensity based on their change in material thickness. Unfortunately, we still do not have a sufficient explanation for the XRR data, and leave this as a challenge for future research.

3.4.5 Mechanical testing of Cu samples

Some of the Cu-FSP samples were mechanically tested using a Vickers microhardness tester. Their hardness values can be found in **Table 3.7**. Cu-1 tests showed a slight decrease compared to the control Cu sample (-3.5%), while the unannealed and annealed Cu-2 samples both showed an increase in hardness (+17% and +12%, respectively). These results indicate that there was some benefit to adding the polymer precursor material via FSP to the Cu matrix, with a sustained increase in hardness after annealing, despite our lack of finding well-dispersed reinforcement.

Table 3.7 Vickers Microhardness values for the Cu-MBPP experiments

Sample	Hardness (MPA)	SD
Cu-1	456.5	168.7
Cu-2	553.8	106.8
Cu-2, annealed	529.2	86.2
Cu FSP, control	473.1	23.2

3.4.6 Conclusions from Cu experiments

We decided to discontinue working with Cu and FSP for a number of reasons. First, transitioning to FSP experiments turned out to be far more complex that we realized, and it would have taken a significant amount of time to optimize the process to efficiently incorporate polymer into the metal matrix while avoiding further breaking of tool tips. One possibility to reduce tool tip wear would be to use long channels parallel to the tool path filled with polymer powder instead of individual holes, or a combination of holes and a channel as done by Kumar *et al.* [93, 172]. There was also a standing question as to how much polymer was pyrolyzed during the FSP step and how much was incorporated unpyrolyzed, as well as whether it would be better for the polymer to pyrolyze during the FSP or in an annealing step after. Finally, our primary goal was to create low-weight MMNCs; Cu was a good surrogate to watch MBPP *in situ* via

XRR at ANL since Al and SiC would have been indistinguishable from one another, but Cu was not the focus of the MBPP research. Based on these questions and problems, along with the fact that the XRR results did not reveal enough significant information, we decided to discontinue researching Cu for MMNC experiments.

3.5 Metal-based polymer pyrolysis experiments in other metal systems

3.5.1 Motivation

After some success in Al and Cu matrices we decided to test MMNC production via MBPP in other metal systems. The systems were chosen for two main reasons: Mg was chosen to follow similar experiments done in literature and for its possible use as a lightweight composite matrix material, and Zn and Sn were chosen as systems with very low melting points. We repeated similar experiments to literature to try and elucidate how MBPP could be improved in Al alloys, and the tests with low melting metals was done to test how well we could disperse unpyrolyzed material into a metal melt without it pyrolyzing.

3.5.2 Experiments with Mg – methods

Mg-based MBPP experiments were conducted in Professor Alan Lou's lab at The Ohio State University, Materials Science and Engineering department) with the assistance of Michael Moodispaw and Dr. Jianyue Zhang. The experiments were conducted to match those done in literature using molten Mg [84, 150, 173-177]. We chose to use AZ91 due to its commercial popularity and because it was most readily available for the experiments. While most of the MBPP work with Mg has used commercially pure Mg [84, 150, 174-177], there was some success in literature using other Mg alloys such as AZ91 and AE44 [173]. The nominal chemistry of AZ91 can be found in **Table 3.8**.

Table 3.8 Nominal composition of AZ91 [83]

Element	Composition (wt%)
Al	8.3-9.7
Zn	0.3-1.0
Mn	0.15-5.0
Si (Max)	0.1
Fe (Max)	0.005
Cu	0.03
Ni	0.002
Mg	Balance

All the experiments were conducted using graphite crucibles and 80 g of AZ91 with the aim of adding 2 wt% polymer into the matrix. **Table 3.9** lists out which polymers were used in each experiment. Prior to each experiment the graphite crucible was coated internally with a BN spray to prevent reactions with the graphite. An induction furnace with an MTI heater was used with a set current of 400 A to reach 850 °C. There was some current drift present, so an immersion thermocouple probe was used to ensure the correct temperature of the melt. During heating a cover gas of CO_2 with 5 vol% SF_6 (5000 ppm) was used to prevent the molten AZ91 from reacting with oxygen. SF6 is commonly used as a cover gas for Mg experiments as its density is so high that it sinks to the surface of the melt and stays there as a protective layer. The polymers were wrapped in Al foil (Kroger Home brand), then the package was preheated to 200 °C in a box furnace prior to adding to the melt.

Table 3.9 Outline of Mg-based MBPP experiments

Experiment No.	Polymer Precursor	Microhardness (MPA)	SD (MPA)	Change (%)
1	N/A (control)	677	21.1	0.00
2	SMP-730	680	26.7	0.55
3	SMP-730	700	29.1	3.50
4	SMP-500	644	35	-4.85
5	SMP-500	670	24.2	-1.03
6	SMP-10	670	21.2	-1.04
7	Durazane 1800	700	43.8	3.40

Once the melt was at temperature, we added the polymer packet and hand stirred with a graphite rod for <1 minute, all while the crucible was still in the induction coil. After mixing in the packet we closed the furnace and reheated the melt for 5 minutes, after which the crucible was removed, then the oxide was skimmed with a graphite rod and finally the melt was cast into a preheated (200 °C) permanent steel mold. The mold used was designed for 5 mm thick plates. Previous experiments in the Lou group with Mg alloys measured a cooling rate of 60 °C/s for this mold. Once the castings were solidified, we removed them from the mold and quenched in water. There was the possibility of using a Col Palmer ultrasonic processor to ultrasonicate the molten composite prior to casting but incorporating this step safely while still acting swiftly enough to prevent the melt from solidifying proved to be too difficult with the experiment setup.

3.5.3 Experiments with Mg – results

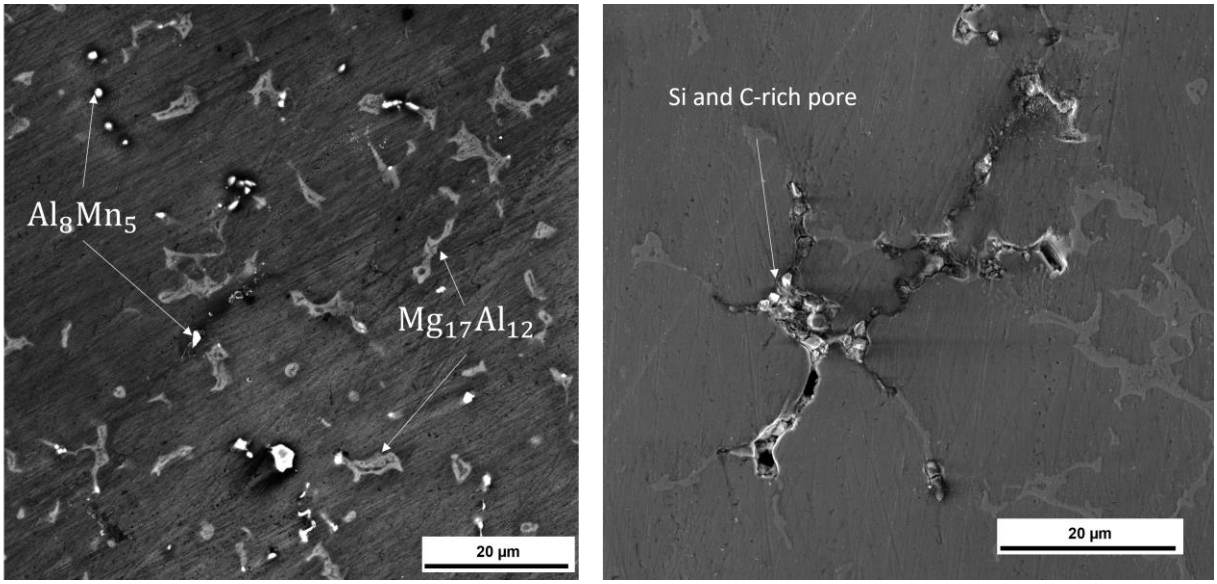

Figure 3.27 (a) Sample SEM showing the microstructure of the AZ91 samples, (b) A porous region in the sample rich in Si and C from the polymer pyrolysis

The experiments with Mg did not lead to a significantly altered microstructure. Vickers microhardness, SEM, and XRD were taken for these samples following the methods outlined in

previous sections. SEM and XRD analysis show the standard structures of AZ91: α-Mg matrix, ß phase ($Mg_{17}Al_{12}$, also referred to as γ phase), and particles of Al_8Mn_5. A few samples showed porous regions that were rich in Si and C, although these were not common and primarily found in sample 7, which was made using Durazane 1800. Example microstructures from these experiments are found in **Fig. 3.27**. The change in microhardness varied between samples, with sample 3 and 7, made with SMP-730 and Durazane 1800, showing the most improvement compared with the control, while other samples showed a decrease in microhardness (see **Table 3.9**). XRD identified the normal phases for AZ91, but unfortunately peaks for Mg and MgAl2 completely overlap the biggest peaks for SiC, so XRD was not beneficial for identifying any phases formed via MBPP. Example XRD spectra are shown in **Fig. 3.28**.

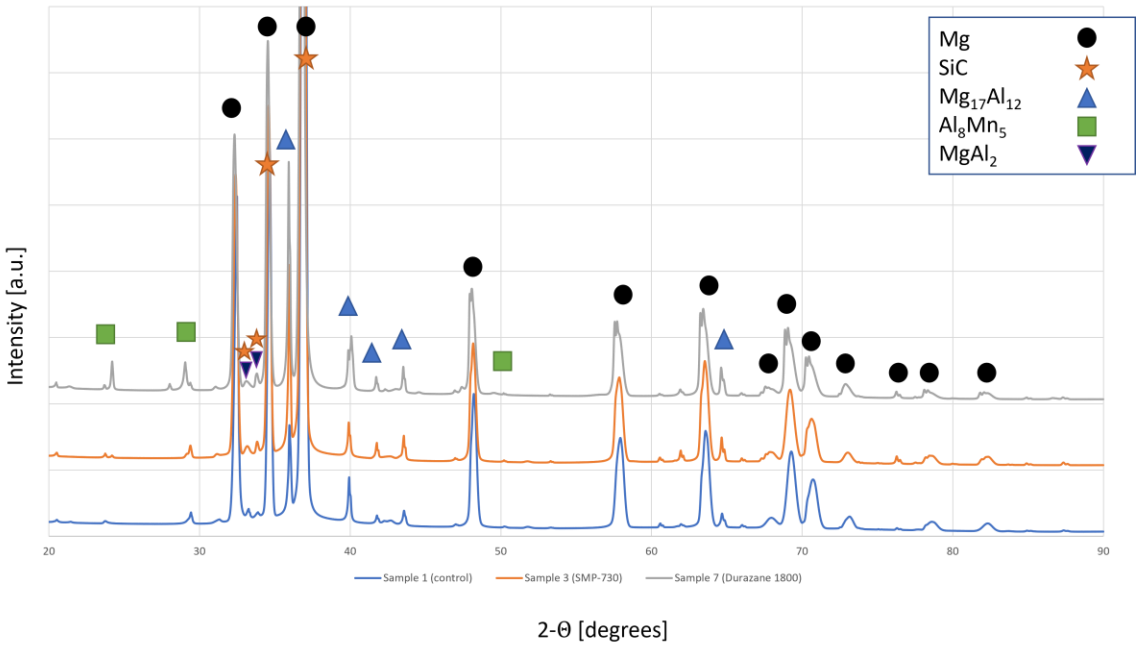

Figure 3.28 X-ray diffraction of AZ91-MBPP samples, (bottom) control sample, (middle) Sample 3, made with SMP-730, (top) Sample 7 made with Durazane 1800

3.5.4 Experiments with Sn– methods and results

Experiments were done with Sn to test if we could add polymer material into the metal without any amount of pyrolyzing and minimal thermal cross-linking to occur since the melting temperature of Sn (T_m = 232 °C) is well below the pyrolyzing temperature. Experiments were conducted using 5 wt% Durazane 1800 and either Sn foil or Sn powder (99.8%, < 45 μm, Sigma Aldrich). The Sn foil was made by rolling Sn sheet (99.9%, McMaster-Carr) to 2 mm thick. Foil experiments were conducted by wrapping thermally cross-linked (T = 300 °C) Durazane 1800 powder with the Sn foil, then heating that packet up to 850 °C under Ar and holding for 1 hour. Sn powder experiments were conducted in a similar manner, except that the polymer and Sn powder were hand-mixed until homogeneous prior to heating.

There were multiple problems which hampered these experiments. First, the Sn was prone to severe oxidation at the pyrolyzing operating temperature, despite the Ar cover gas. 850 °C was clearly far too high a temperature to operate with Sn without a vacuum or exceedingly clean protective atmosphere. Wetting was clearly an issue, to the point that pyrolyzed material would easily flake off and be completely unmixed with the Sn after the experiments. On top of the wetting, the density differences between Sn and the polymer were so great ($\rho_{Sn}^{liq} = 7\frac{g}{cm^3}, \rho_{poly} = 1\frac{g}{cm^3}$) that the polymer was able to float to the top while Sn was molten and heating up to the pyrolyzing regime.

The foil experiments yielded no significant results; it was clear that after the Sn melted the polymeric material floated to the top of the liquid so there was essentially no interaction between the phases during pyrolysis. The powder experiments had slightly better results, although still lacked homogeneity. The powder samples a few regions of large SiCNO precipitates, as identified by spot EDS, although most commonly there was a lamella-type structure between Sn and SiCNO phase. A sample microstructure and EDS map can be found in

Fig. 3.29. Based on these results we decided that MBPP in Sn was not a suitable substitute for understanding the process in an Al matrix.

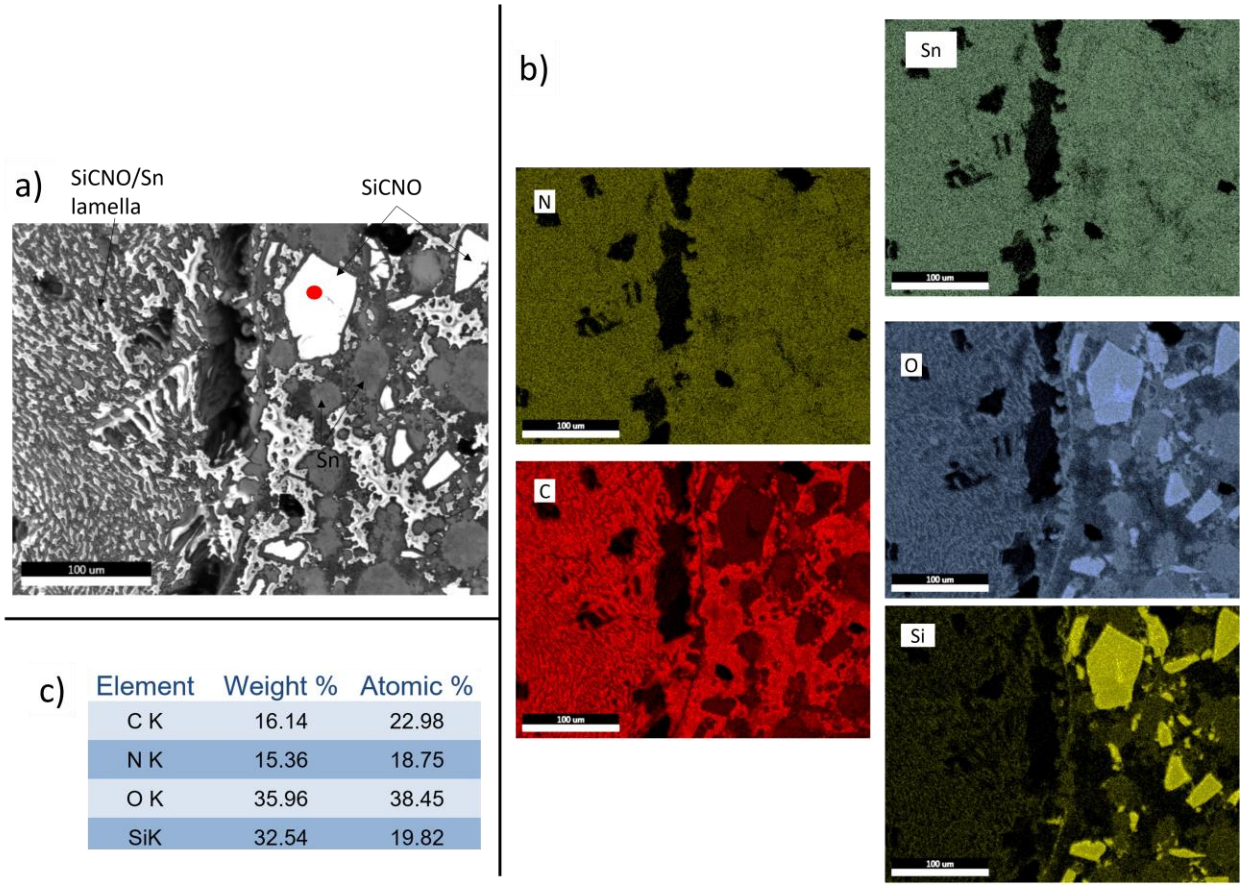

Figure 3.29 (a) Sample SEM of the Sn-MBPP microstructure in a region with PDCs mixed into the matrix, (b) EDS map of a) for N, C, Sn, O, and Si, (c) Spot EDS from the red dot in a)

3.5.5 Experiments with Zn – methods and results

Experiments with Zn were conducted for a similar reason to the Sn experiments, where the melting temperature of Zn (T_m = 420 °C) is lower than that of Al (T_m = 660 °C). These experiments used Zn powder (99.9%, 150 µm, Sigma Aldrich) as the matrix material and was mixed with SMP-10 for 5 wt% addition. The mixture was heated to 850 °C under Ar and held for 1 hour.

While the samples did not oxide as much as Sn, the Zn experiments were plagued by the other problems found in the Sn experiments (poor wetting, density differences). The samples were imaged on the low vacuum mode of a Tescan Rise using a 100 µm aperture inserted into the objective lens and operating at 30 keV and a beam current of 330-350 pA. Low vacuum imaging was chosen to reduce the amount of charging by the pyrolyzed phase and improve the possibility of identifying any phases in the pyrolyzed material. Unfortunately, the regions that had some amount of pyrolyzed ceramic showed complete separation from it and the Zn powder (**Fig 3.30**). After a few initial experiments it was decided to not continue working with Zn.

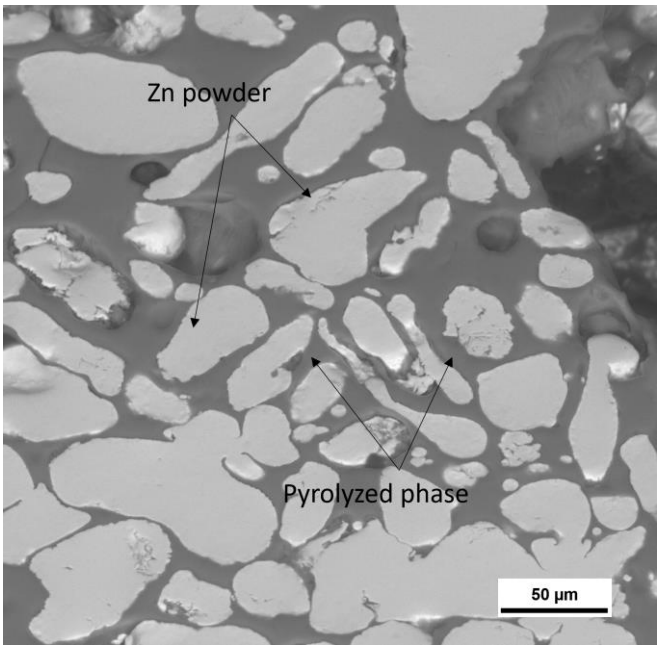

Figure 3.30 Sample SEM showing the microstructure of the Zn-powder MBPP experiments. The pyrolyzed material and the Zn matrix are marked

3.6 Conclusions

In this chapter we investigated *in situ* MMNCs processed via MBPP and assessed the feasibility of using MBPP as a processing route for MMNC production. The work focused first on the analysis of multiple perspective precursor polymers, by analyzing their thermal

degradation and ceramic yield using thermogravimetric analysis coupled with differential scanning calorimetry, Fourier transform infrared spectroscopy, and X-ray diffraction. Significant attention given to Durazane 1800 and SMP-10. Al-SiC(O) and Al-SiCN(O) MMNCs were the focus of the experiments, although tests with Mg, Zn, Sn, and Cu were also done.

Multiple *in situ* aluminum matrix composites were fabricated by combining aluminum powder with the polymer at different weight fractions, then the mixtures were heated to a temperature of 850 °C to pyrolyze the polymer within the Al matrix. Scanning electron microscopy found that the formed composite microstructure was porous but showed a good dispersion of reinforcing particles consisting of blocky SiO_2 and needle-like SiOC ranging from 0.15 – 3 μm. Vickers Microhardness of the as-cast composites showed an increase of 350% and 122% for Al – 15 wt% Durazane 1800 and Al – 15 wt% SMP-10, respectively. The porosity in the samples and inhomogeneous distribution of the created particles prevented further mechanical tests. Poor wetting between the metal matrix and the polymer powder was common in all the material systems and led to lower than expected amount of strengthening phase in the matrix. Furthermore, reactions between the elements in the polymer and the metal matrix were observed, meaning that the pyrolysis was not occurring as it would in a fully inert environment.

CHAPTER 4

Salt-Flux Reaction Synthesis: Insights into Reaction Pathways and Formed Microstructure in Al/TiC Metal Matrix Nanocomposites

4.1 Introduction

Current demands for fuel-efficiency and increased electric vehicle range in the automotive and aerospace industries continue to push the necessity of strong and lightweight materials. Al-alloys have been used extensively due to their high strength-to-weight ratio, but the reduction of mechanical properties at elevated temperatures limits their use in many applications. In comparison to base alloys, Al-based metal matrix nanocomposites (MMNCs) have improved mechanical properties at both ambient and elevated temperatures, with their properties heavily dependent on the reinforcement characteristics (e.g. size, volume fraction, morphology) [25, 40-42, 54, 182-189]. MMNCs are often produced through *ex situ* methods, where the reinforcement particles are premade and mixed into the matrix [40, 54, 183, 184, 186] which allow for controlling particle size, type, and volume fraction, but *ex situ* processing methods can lead to reinforcement contamination [25, 28], undesirable particle-matrix interfacial reactions [28, 190] and poor particle-matrix wetting [21, 25] thus making the production of large-scale MMNCs difficult.

Alternatively, *in situ* methods generate reinforcing particles directly in the melt via reactive processes, thereby avoiding some of the difficulties faced by *ex situ* MMNCs [39-41, 191-193]. The reactive processes to form particles *in situ* are typically complex and can involve

intermediate reaction steps, parallel reaction pathways that form different reinforcement morphologies, and the generation of undesirable secondary phases, all of which affect the final microstructure and mechanical properties [10, 100, 107, 191, 192, 194-197]. Therefore, further understanding of the particle formation kinetics and reaction pathways is critical for microstructural control of *in situ* MMNCs.

A promising *in situ* approach for creating Al-TiC MMNCs involves reacting a mixture of C powder and a Ti-bearing salt-based flux (dipotassium titanium hexafluoride, K_2TiF_6) in an Al melt [41, 100, 107, 112, 191, 196-199]. When the flux is reduced by the Al melt it releases solute Ti by **Eqn. 4.1** [100, 102, 103, 107, 200].

$$3K_2TiF_6(l) + 4Al(l) = 3[Ti] + 3KAlF_4(l) + K_3AlF_6(l) \quad (4.1)$$

This approach is promising for its ease of use and for its potential to be integrated into a foundry workflow as surface fluxes are already an industry practice, and Lee et al. found that changing the Ti-bearing flux may not affect the produced MMNC [199]. The TiC is hypothesized to form through a reaction between solid C particles and free Ti atoms that are released during the flux reduction by the liquid Al, however multiple underlying mechanisms and kinetics are still subject to question [41, 100, 107, 189, 191, 198, 201, 202]. TiC is expected to be formed either directly from Ti and C (**Eqn. 4.2** or **4.3**), or indirectly by first forming an Al_3Ti intermetallic which then breaks down and reacts with C to form TiC (**Eqn. 4.4**). It has also been speculated that for other *in situ* processes TiC can be formed indirectly using Al_4C_3 as an intermediate phase, but that intermetallic has not been seen from salt-flux reactions [192, 201, 203].

$$[Ti] + C(s) \rightarrow TiC(s) \quad (4.2)$$

$$[Ti] + [C] \rightarrow TiC(s) \quad (4.3)$$

$$[Ti] + 3Al \rightarrow Al_3Ti(s), \text{ then } Al_3Ti(s) + [C] \rightarrow TiC(s) \quad (4.4)$$

It is still unclear which mechanism of formation is followed for salt-flux reaction synthesis, including what role the Al_3Ti plays in the production of TiC particles, and the submicrometer nature of the TiC particles limits which techniques can be used to study the reaction.

Synchrotron-based X-ray characterization has led to great insights into multiple MMNC systems recently, including the effects reinforcing particles have on grain growth [204-206], MMNC additive manufacturing [207, 208], ultrasonic processing of molten MMNCs [209], and analyzing void formation within MMNCs [210]. The high spatial and temporal resolution and 3D analysis gives improved understanding of detailed microstructure and the effects of processing parameters.

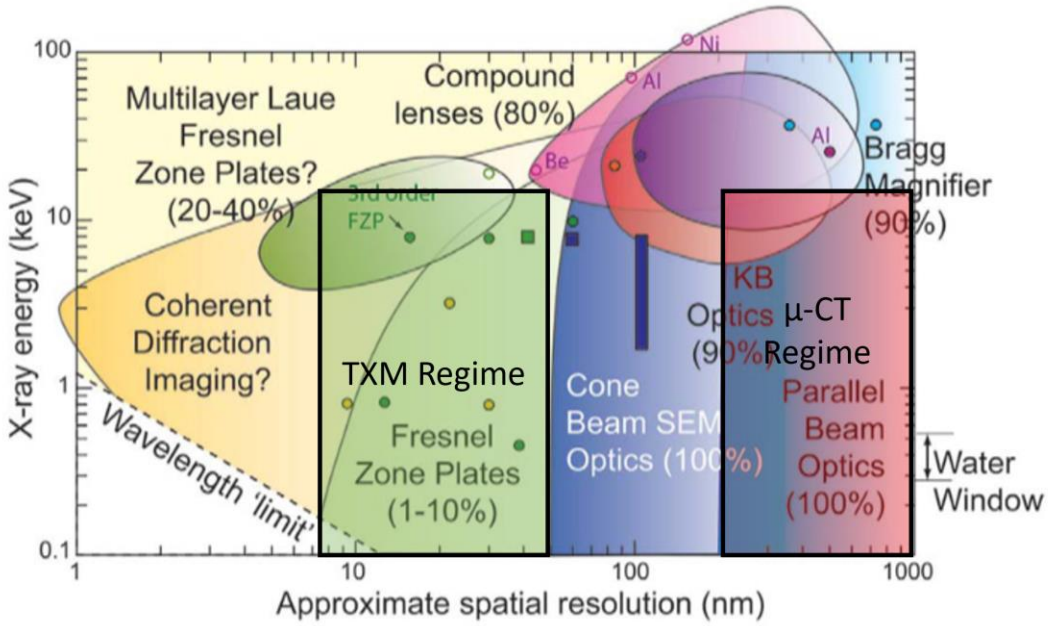

Figure 4.1 A schematic summarizing various x-ray tomography imaging modes compared with their spatial resolution. Regions corresponding to TXM (Fresnel Zone Plates) and µ-CT (Parallel Beam Optics) have been outlined for clarity (adapted from [211])

We used synchrotron-based X-ray nanotomography (TXM) to visualize the microstructure of *in situ* Al/TiC MMNCs in 3D with nanoscale resolution to gain a deeper understanding of their microstructure and therefore the formation mechanisms of TiC as well as the distribution and morphologies of the TiC and Al_3Ti formed via salt-flux reaction synthesis. Based on previous experiments we knew that the TiC particles formed via salt-flux reaction synthesis are often sub-micrometer, and are generally tens of nanometers in diameter, which made visualizing them particularly difficult. The enhanced optics at our chosen beam line can achieve a resolution of < 20 nm^2 per pixel, thus this technique provided a solution to the problem of visualizing the extremely small particles. In comparison, lab-based µ-CT equipment can only achieve a resolution of 1 μm^2 per pixel, so any µ-CT scans would make distinguishing individual TiC particles impossible. The schematic in **Fig. 4.1** shows the various types of optics in X-ray tomography equipment and their possible pixel resolutions, with regions corresponding to what is used for TXM and µ-CT highlighted for clarity (adapted from [211]).

4.2 Salt-flux reaction synthesis (SFRS) experimental methods

4.2.1 SFRS experimental methods

The *in situ* MMNC samples were prepared using Al shot (99.99%, 2-5 mesh, Belmont Metals) as the metal matrix. K_2TiF_6 flux (> 100 µm, Millipore Sigma) and super activated C (<100 nm, SkySpring Nanomaterials, Inc.) powders were chosen as reactants, and weighed out to target a 1:1 molar ratio for stoichiometric TiC production. The powders were mixed with mortar and pestle until homogeneous, then added in an amount to create 3 vol% TiC in the Al melt, assuming 100% of the Ti released from the flux reacted to form TiC. Molten Al at 850 °C has a solubility of 1 wt% Ti, which if met would be about 25% of the Ti from the flux. While some Ti loss to solute is expected, the salt-flux reaction is said to take place at the liquid flux-melt

interface so it was assumed that a majority of the Ti would react to form TiC rather go into the melt [100].

The Al was melted in a 3 kg graphite crucible (inner diameter 49 mm) and brought to 850 °C without a protective gas cover. Once the melt had reached 850 °C, as measured by an immersion temperature probe, the powder mixture was added on top of the melt and allowed to remain stagnant until the flux was fully liquified. The melt was mixed via a BN-coated steel impeller placed at the liquid Al/liquid flux interface rotating at 300 RPM for 10 minutes, after which the melt was poured in a straight line (8-11 mm thick and 25-40 mm wide) on a chilled Cu plate (1 °C) to avoid settling of the particles and ensure their presence in the micropillar TXM samples.

Metallographic specimens for SEM imaging were sectioned from the as-cast material then prepared using standard polishing procedures with a 1 µm diamond-suspension finishing step. 2D microstructure characterization was performed using a Tescan MIRA3 field emission gun (FEG) SEM operating in backscatter electron (BSE) mode at 15 kV and a beam intensity of 8-12. An integrated EDAX energy dispersive spectroscopy (EDS) system was utilized for chemical identification. X-ray diffraction (XRD) analysis was performed using a Rigaku SmartLab XRD operating at 40 kV and 44 mA with Bragg-Brentano para-focusing optics and a D/tex Ultra 250 detector.

A 1 mm rod sample of the as-cast MMNC was analyzed using a Zeiss Xradia Versa 520 X-ray Microscope operating at 40 kV and 75.07 µA in absorption mode for a voxel size of 0.33^2 μm^2. TEM samples were made by locating specific features in the µ-CT dataset and performing liftouts of them with the FEI Helios™ operating with similar parameters to the TXM sample preparation. TEM and STEM were done with a Thermo Fisher Scientific Talos F200X G2

S/TEM operating at 200 kV. The high angle annular dark-field (HAADF) images were acquired in a collection range of 55-200 mrad, with a probe convergence angle of 10.5 mrad. Energy-dispersive X-ray spectroscopy was collected with the Super-X EDS detector.

We conducted full field X-ray TXM at sector 18-ID at Brookhaven National Laboratory's National Synchrotron Light Source II (Upton, NY, USA). A monochromatic X-ray beam operating at 7 keV illuminated the sample, then a zone plate used as an objective lens with 323× magnification focused the beam onto the detector. A pixel size of 20^2 nm^2 was attained, with a FOV on the detector measuring 51.2 x 43.2 μm^2. A more detailed description of the experimental setup is available elsewhere [212]. During the TXM experiment, the sample was rotated at 2 °/s from 0 to 180°, with an exposure of 0.1 s.

4.2.2 Synchrotron-based X-ray nanotomography sample preparation

1 mm rods were cut out of the quenched MMNC samples via wire EDM (Cut-Rite EDM, Inc.), after which the rods were thinned to a point of 80-100 μm in diameter by electropolishing following a recipe used in our previous work [192]. Electropolishing was done using a mixture of methanol (CH_3OH) and nitric acid (HNO_3) at a 3:1 volumetric ratio. The beaker with the electrolyte mixture was placed in a larger beaker filled with ice and allowed to cool for 5 minutes prior to electropolishing. Once the liquid was cooled, one of the 1 mm rods and a steel plate were placed into the electrolyte being sure that the two did not touch. For this setup the EDM cut sample was acting as the anode, or the workpiece, while the steel was acting as the cathode. 10 V was used for bulk material removal, which lasted for 1-2 minutes, then 5-7 V were used for the final polishing of the sample to reduce surface roughness and better control the tapered tip. While electropolishing care was taken to examine the samples intermittently to ensure enough material was being removed and that a pointed tip was being formed. Samples were cleaned with

acetone then ethanol after electropolishing, then were stored in a Cryo Pin storage box (Ted Pella, Inc.).

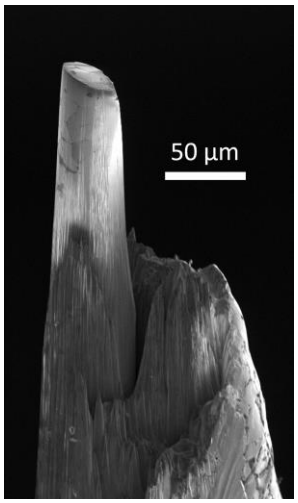

Figure 4.2 A FIBed micropillar sample made for TXM experiments

TXM micropillar specimen approximately 50 µm in diameter and 100 µm in height were fabricated from the electropolished rods via plasma Xe^+ ion milling with an FEI Helios™ G4 P-FIB operating at 30 kV and 2.5 µA for general milling, and polishing cuts were made using 30 kV and 60 nA. A representative TXM micropillar is shown in **Fig. 4.2**. Sufficient absorption

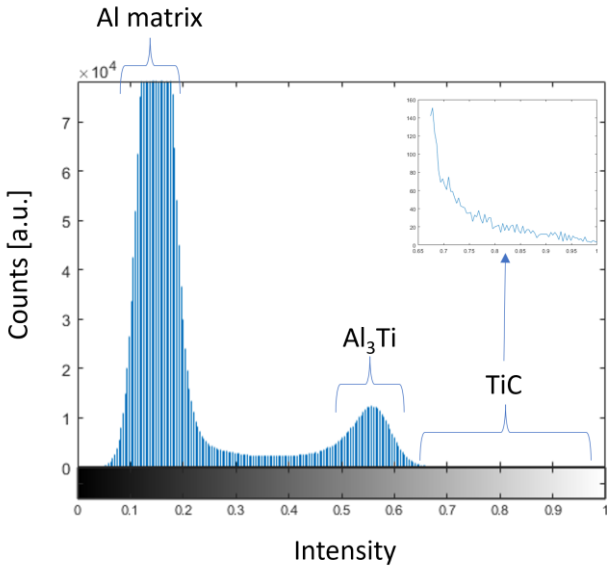

Figure 4.3 Histogram of intensity values from the reconstructed TXM data, values for the Al matrix, Al3Ti intermetallic, and TiC particles are marked. Inset shows counts for the TiC region of the histogram

contrast at 7 keV enabled identification of the phases present in the microstructure: namely the Al matrix (dark gray), Al_3Ti intermetallic (medium gray), and TiC (bright). A histogram of the grayscale intensities of the phases within the TXM data is shown in **Fig. 4.3**. Theoretical attenuation lengths, attenuation coefficients, crystal structure, and other pertinent information for the found phases and for potential phases formed during SFRS are shown in **Table 4.1**. Phase density values were from [213] and attenuation lengths were from [214]. The attenuation lengths (L_{atten}) were converted to mass attenuation coefficients ($\mu_M$or written as $\frac{\mu}{\rho}$) using Eqn 4.5, then were converted to linear attenuation coefficients (μ_L) using Eqn 4.6 [214], where ρ is the material density.

$$\mu_M = \frac{1}{L_{atten} * \rho} \tag{4.5}$$

$$\mu_L = \mu_M * \rho \tag{4.6}$$

Table 4.1 Crystal structure and attenuation data for potential phases formed during salt-flux reaction synthesis

		Attenuation Length at 7 keV [213]	**Density [212]**	**Mass Attenuation Coefficient**	**Linear Attenuation Coefficient**
Phase	**Crystal Structure**	L_{atten} (cm)	ρ (g/cm^3)	μ_M (cm^2/g)	μ_L (1/cm)
Air	Gas	5.06E+01	1.21E-03	16.39185812	1.98E-02
Al	Cubic	5.25E-03	2.7	70.50161618	190.35
Al_4C_3	Trigonal	6.15E-03	2.98	54.52086464	162.47
AlF_3	Orthorhombic	9.21E-03	2.82	38.48716144	108.53
C (Graphite)	Hexagonal	6.65E-02	2.26	6.65408282	15.04
F	Gas	2.53E+01	1.70E-03	23.3315253	3.96E-02
K	BCC	5.31E-03	8.62E-01	218.3387645	188.21
K_2TiF_6	Trigonal	2.36E-03	3	141.4425156	424.33
K_3AlF_6	Cubic	3.17E-03	2.7	116.8287081	315.44
$KAlF_4$	Tetragonal	3.87E-03	3.01	85.95532163	258.73
KF	Cubic	2.54E-03	2.55	154.568942	394.15
Ti (High temp)	Cubic	7.70E-04	4.37	297.0934372	1298.30
Ti (Low temp)	Hexagonal	7.50E-04	4.49	297.0936543	1333.95
$Ti_{1.1}Al_{2.9}$ (High temp)	Tetragonal	1.80E-03	3.44	161.6468843	556.07
Ti_3Al	Hexagonal	9.07E-04	4.22	261.2528936	1102.49
TiAl	Tetragonal	1.22E-03	3.82	215.4107802	822.87
$TiAl_2$	Tetragonal	1.60E-03	3.53	177.0151023	624.86
Al_3Ti	Tetragonal	1.92E-03	3.37	154.7038486	521.35
$TiC_{(0.95)}$	Cubic	8.53E-04	4.91	238.8349052	1172.68
TiF_4	Orthorhombic	2.63E-03	2.94	129.1289765	379.64

4.2.3 An alternative path to creating TXM samples

Since conducting these experiments members of the Shahani lab (University of Michigan, Material Science and Engineering department) have come up with a more efficient and safer method of pre-FIB sample preparation to replace electropolishing which we report here. The new method requires a Dremel tool attached to a stand to hold it perfectly horizontal so that the samples can be mechanically ground into a tip by hand. This setup still requires 1 mm rods to be

cut from bulk material via EDM, with the added step that any burr or edge artifact from EDM processing must be ground down so that the rods are as cylindrical as possible. 1 cm sections of the rod are cut to be used as the workpiece, and are pushed into thin plastic casing (e.g. electrical wire insulation) so that the majority of the workpiece (50 – 60% length) is inside the casing. The casing is used to improve the grip of the Dremel tool on the workpiece.

The workpiece is placed inside the Dremel collet and tightened to the point that it does not move while the Dremel is spinning: care must be taken to avoid overtightening and snapping the workpiece. Once in place, the Dremel can be turned on and the workpiece can be hand-sharpened using strips of SiC grinding paper (320, 600, 1200 grit) until the tip is <100 µm in diameter, as measured by optical microscope. Each grinding step can take 3-5 minutes, although it may take more time depending on the user's dexterity and comfort with the technique. After the sample has been ground to a point it must be cleaned by sonicating it in an ethanol bath. After cleaned and dried the sample may be milled using the FIB as discussed in Section 4.2.2. A schematic of this process is shown in **Fig. 4.4**.

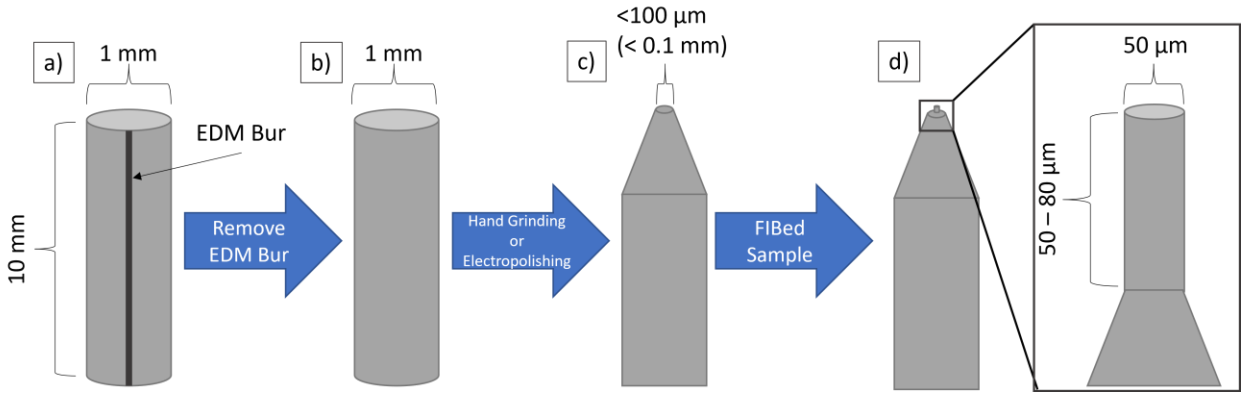

Figure 4.4 A schematic of the process for creating TXM micropillar samples. a) A 1 mm diameter rod received from wire EDM, with a vertical bur along its length. b) The sample after the EDM bur is removed. c) The sample is thinned into a tip of < 0.1 mm either by hand grinding or by electropolishing. d) The final micropillar sample is made using the FIB. *Not shown* is the required cleaning step between c) and d), where the sample is sonicated in ethanol.

4.2.4 Data processing techniques

We used the forward projections to reconstruct the sample volume in 3D using TomoPy, a Python-based open-source framework for tomographic data processing [215]. This work was done using Python 3.8, Anaconda Navigator as the Python hub, Spyder 5.05 for editing and testing code, and Anaconda Powershell prompt (Anaconda3) to run the code. There is currently a push to transition to using JupyterLab and Jupyter Notebook, an online platform for organizing and running code, for this step of the data extrapolation but we will not go into detail here. For more information about JupyterLab see [216].

Using Python we first centered each dataset, then normalized each projection with the corresponding dark- and white-field images, then removed ring artifacts [217], and finally reconstructed the data used the Gridrec algorithm, a direct Fourier-based method with a Parzen window filter [218]. Further calculations were done in MATLAB R2020b using the Image

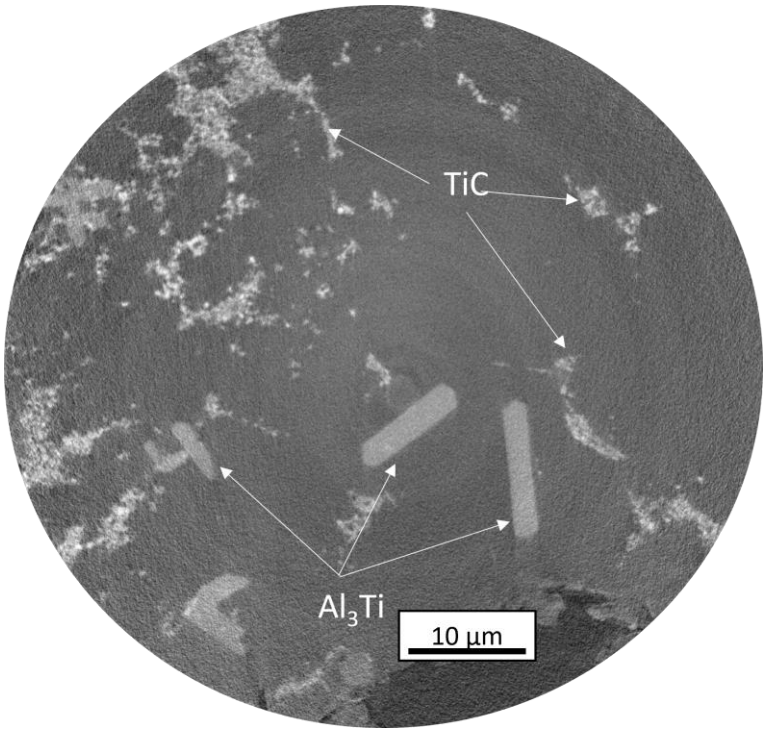

Figure 4.5 Representative reconstructed slice of the TXM data showing TiC agglomerates and Al_3Ti plates

Processing Toolbox by MathWorks. A representative reconstruction slice along the axis of rotation is shown in **Fig. 4.5**, clearly showing the Al matrix (dark gray), Al_3Ti (medium gray), and TiC clusters (light gray) inside the Al matrix. The grayscale intensities of individual slices were normalized using the Beer-Lambert law to account for small differences in slice diameter.

The phases in the TXM data were segmented by going through each 2D reconstructed slice and using a multi-level grayscale thresholding to separate the phases based on their grayscale values. After each image was segmented, it was added to a volume of segmented data so that the 3D structures of the phases could be ascertained and manipulated further. An example of a segmented feature is shown in **Fig. 4.6**.

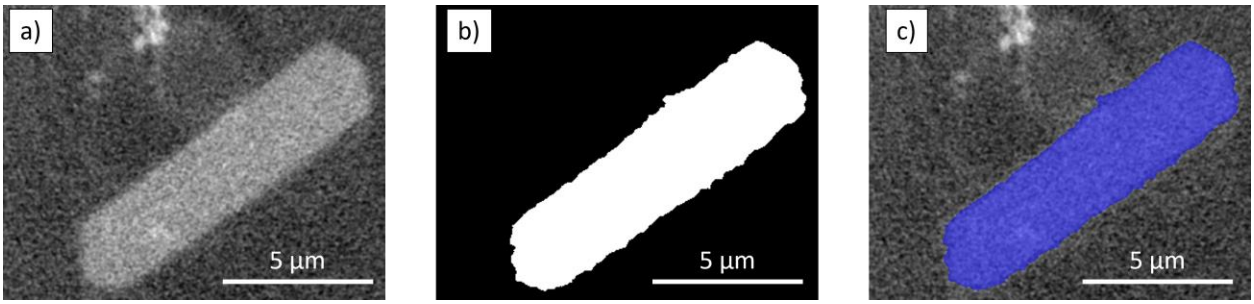

Figure 4.6 Typical process for segmenting the TXM data (a) starting reconstructed image (b) Image segmented by grayscale thresholding (c) A mask of b) overlayed onto image a)

While intensity-based segmentation worked most of the time, there were occasions where the phases overlapped or did not have sufficient contrast to solely rely on pixel values. On some occasions phases had to be differentiated by focusing on their edges, i.e. finding the max of the gradient of pixel values, using MATLAB's built in edge-finding function and pre-defined edge detection methods (e.g. Sobel and Canny) [219]. Once the edges are defined clearly, they can be used by themselves to define phases or masks of the phase of interest can be created and used in conjunction with other techniques for separating the data.

Another way of segmenting was via the randomness in the image: MATLAB's entropyfilt function returns an image where the grayscale values correlate to the randomness in

the image, which can later be segmented using an intensity threshold or edge finding segmentation [220]. This function is particularly helpful for differentiating phases with a repeating pattern or texture from a solid-filled phase. For this work it was useful for differentiating intermetallics from clusters of carbides.

On some occasions the phases overlapped which required a few extra steps to cleanly separate them. First a general threshold was used to separate the features from the background. Once this was done a mask of one phase was created and used on the original image to crop out any unneeded data. The masked image could then be re-segmented with more constrained threshold values than would be usable with the unmasked data. An example of this process is shown in **Fig. 4.7**, where the feature is first masked using edge-finding, then the darker and

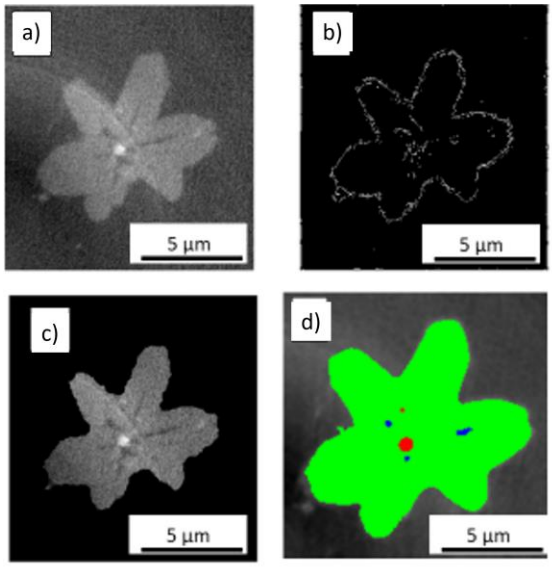

Figure 4.7 Example of a more complex segmentation process (a) Starting image (b) Example of using edge-finding to separate the intermetallic phase (c) Matrix removed by masking the image with the mask from the edge-finding process (d) Overlay of segmented phases, showing the intermetallic in green, TiC in red, and Al inside the intermetallic in blue

brighter features within the masked image can be segmented more cleanly. This process was particularly helpful in segmenting internal features that had similar grayscale values to the Al matrix that otherwise may have been lost.

A variety of steps could be done following the segmentation. The most common data processing workflow of the segmented data included median filtering in 3D to reduce background noise, followed by removal of volumes below a certain size threshold. From the filtered data the effective volume fractions were calculated, and effective particle diameters were determined based on the sizes of the individual connected components of each phase.

For 3D visualization the segmented data had to be converted from a volume of segmented data into a surface by using the isosurface command in MATLAB [221]. This command generates arrays of the faces and vertices for the 3D structures of the segmented phases. Once the data was in this format it could be further smoothed to improve surface calculations, such as interfacial normal distributions, and visual appearance [222]. Helpful MATLAB functions for segmenting and creating a 3D visualization can be found in **Appendix A**.

As a side note, cropping the data tightly to the region of interest (ROI) was an important step to reduce computation time and noise in the data. Normally the images can be cropped to a rectangular or circle around a ROI, eventually making a rectangular prism or cylinder of 3D data, respectively. Cropping was also key to remove any edge defects in the sample data.

4.3 Results and discussion

4.3.1 Microstructural observations

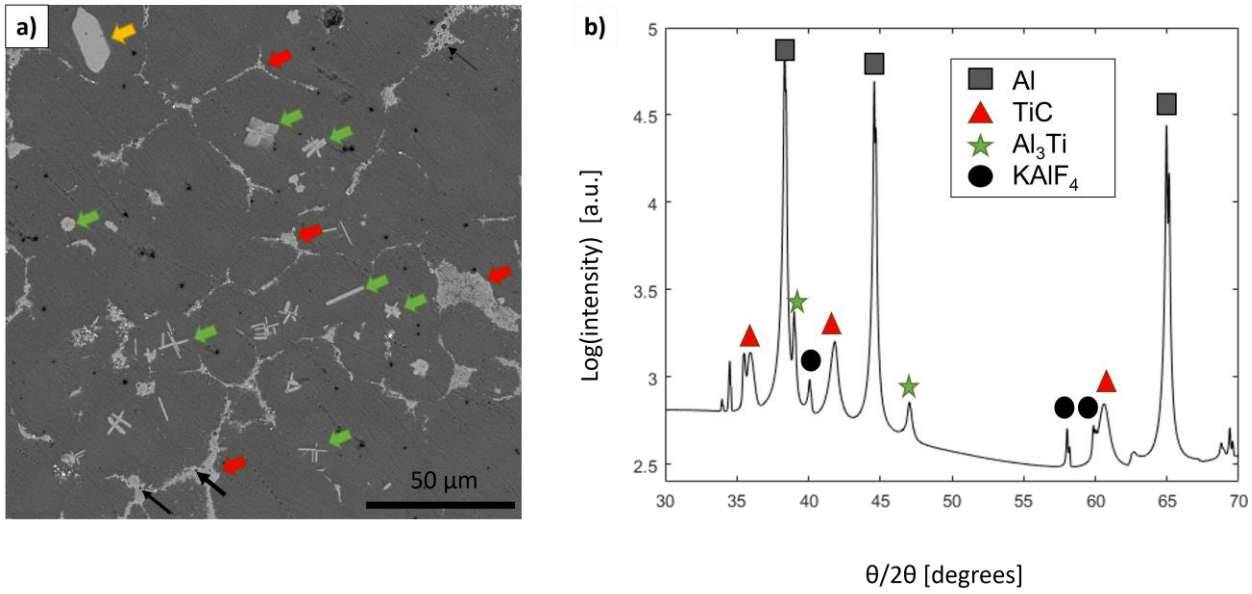

Figure 4.8 (a) Representative SEM micrograph of the quenched Al-TiC MMNC. The TiC (red arrows) and Al_3Ti intermetallic (green arrows for orthogonal plates, yellow arrow for individual plate), and $KAlF_4$ (black arrows) are all present. (b) XRD pattern of the as-made material. Peaks for Al, TiC, Al_3Ti and $KAlF_4$ are present

The morphologies of Al_3Ti and TiC particles can be seen in **Fig. 4.8a**. The SEM shows Al_3Ti intermetallics of various sizes (green arrows). Generally, they are overlapping plates at various orientations, although there is one large individual plate near the top left corner (see the orange arrow in **Fig 4.8a**). The TiC particles (red arrows) can be seen as agglomerates in the grain boundaries, likely pushed there during solidification [223]. Al_3Ti intermetallics (green arrows) of multiple morphologies can also be seen through the sample. Particles of $KAlF_4$ (black arrows), a product of the flux reacting with Al, can be seen within the TiC agglomerates as small black circles. For typical use of K_2TiF_6 flux, the $KAlF_4$ and other byproducts are removed from the melt via degassing and can be found in the dross [41, 100, 197, 224], but we did not perform this step prior to quenching. XRD peaks for TiC, Al_3Ti, and $KAlF_4$ can be seen in **Fig. 4.8b**, verifying that both TiC particles and Al_3Ti intermetallics were created via the *in situ* process.

There is no sign of excess C in either the SEM or XRD, likely due to staying afloat in the liquid flux layer and being skimmed off prior to pouring.

A 3D visualization of the microstructure can be seen in **Fig**. **4.9a,** with the TiC in red and the Al_3Ti in green, and the data edge in light blue, while **Fig. 4.9b** only displays the Al_3Ti. Using the segmented data we calculated the volume fraction of the TiC and Al_3Ti to be 3.3 and 0.8 vol%, respectively. Multiple morphologies of Al_3Ti were found in the TXM data, including orthogonal plates (**Figs. 4.9c** and **4.9d**), individual plates (**Figs. 4.9e** and **4.9f**), cuboids (**Figs. 4.9g** and **4.9h**), as well as large blocks (**Fig. 4.10**). **Fig. 4.9b** shows the orthogonal plates and individual plates, orange and black arrows respectively, but the other types were not shown in this data. **Figs. 4.9c**, **4.9e**, and **4.9g** were the smallest intermetallic of their morphological type found in the data, while **Figs. 4.9d**, **4.9f**, and **4.9h** show a more developed version of that morphology with pointed corners due to growth instability [225-227]. In all, 41 orthogonal

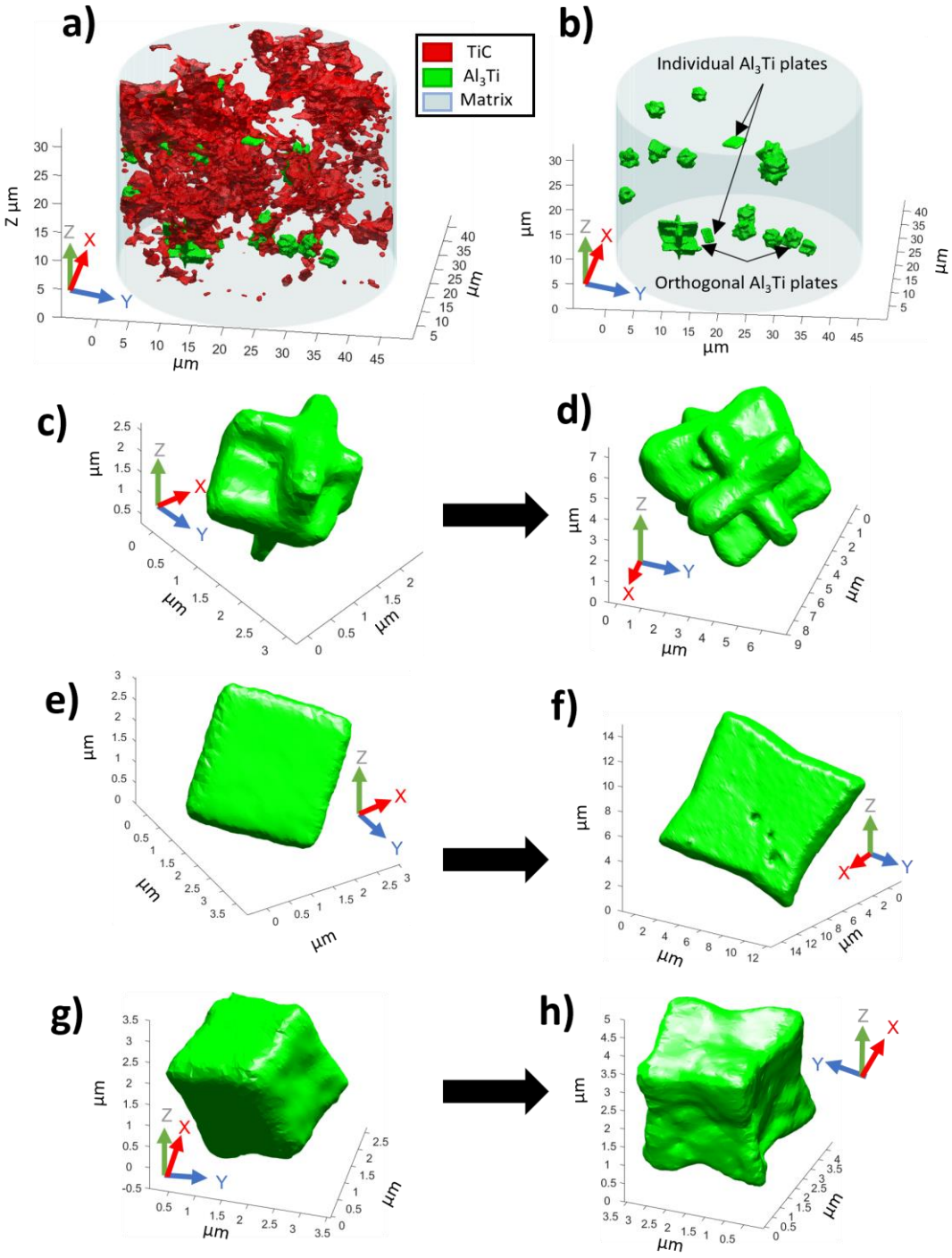

Figure 4.9 (*a*) Volume rendering of a cylindrical field-of-view within stacked TXM slices. Multiple forms of Al_3Ti (green) are shown alongside agglomerates of TiC (red). The data boundary is light blue. (*b*) Same volume rendering displaying only the Al_3Ti, orthogonal plate structures (orange arrows) and individual plates (black arrows) can be seen. (*c*) Small orthogonal plate Al_3Ti (*d*) Larger orthogonal plate Al_3Ti whose sides are bowed from growth instability. (*e*) Small individual plate Al_3Ti (f) Larger plate Al_3Ti whose sides are bowed from growth instability. (*g*) Small cuboid Al_3Ti (h) Larger cuboid Al_3Ti whose sides are bowed from growth instability.

plates, 18 individual plates, 11 cuboids, and 3 instances of large blocks were found in the TXM

data. The surprising diversity of Al_3Ti morphologies led to further examination into the intermetallics themselves, as intermetallic morphology can directly impact mechanical properties [228].

It has been demonstrated that Al_3Ti morphology is affected by cooling rate [196, 197, 229-235], so a repeat melt experiment was performed to measure the cooling rate of Al on chilled Cu. For this experiment pure Al was heated to 850 °C and poured onto the chilled Cu plate while multiple thermocouples were placed directly in the path of the pour. Data from the thermocouples was recorded using a DataDI-1100 (DataQ Instruments, Akron, OH). A peak recorded cooling rate of 24 °C/s was measured immediately after the Al was poured on the Cu, while the average cooling rate was 2 °C/s. This cooling rate range is the range in literature to create plate-like Al_3Ti, sometimes called flakey or needle-like, such as in **Fig. 4.9e-f**, with the lower end of the cooling rate capable of forming the coarser blocky Al_3Ti found in **Fig. 4.10** [196, 197, 229-235], and can explain those intermetallic morphologies in our data.

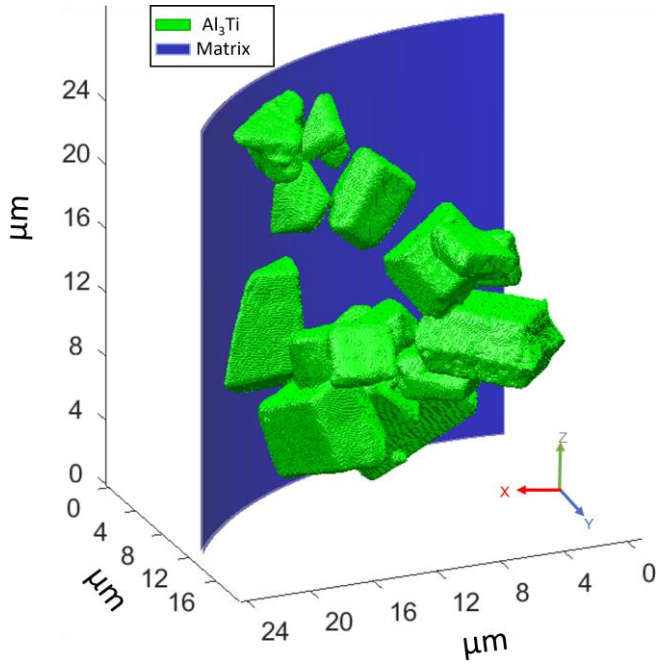

Figure 4.10 Volume rendering of a partial cylindrical field-of-view within stacked TXM slices showing an agglomeration of blocky Al_3Ti (green) along the sample boundary (dark blue).

Unlike the plates, the cuboids and orthogonal plates have not been shown to occur due to changes in the cooling rate of Al-Ti systems. It was suggested by El-Mahallaway that Al_3Ti rich in Ti, closer to Al_2Ti, tends towards a cuboid shape, or that the cuboid is a developed version of globular Al_3Ti precipitates [198]. Majumdar and Muddle found similar cuboid structures and determined it was a ß' phase of Al_3Ti consisting of roughly Al-20wt% Ti [235]. An inhomogeneous distribution of Ti in the matrix may have led to similar trends as seen in El-Mahallway or Majumdar's work since some regions of the TXM data showed a local volume fraction of the TiC exceeding the expected overall volume fraction of 3%, implying inhomogeneous solute Ti in the melt. Small globular Al_3Ti (Ravg = <1um) was also found in the TXM data, but their small size made it was difficult to discern if they were precursors to cuboid shapes or would grow into other morphologies. Other aluminum intermetallics have cuboid morphologies, such as Al_3Zr, Al_3Hf, and Al_3Sc [234, 236, 237], all of which have also shown morphological sensitivity to cooling rate [234, 236, 237]. Therefore, it is possible that the Al_3Ti cuboids are either due to inhomogeneities of the Ti solute, leading to supersaturated Al2Ti intermetallics, or from impurities in the matrix.

There are some examples of the orthogonal plates of Al_3Ti in literature, that were either assumed to occur due to twinning [238] or were not studied in depth [107, 187]. There are multiple examples of thin flakes of Al_3Ti forming perpendicular structures, although they tend to be much larger dendrites of intermetallic formed through slow cooling [196, 197, 229-233]. Looking through the TXM data we consistently found TiC particles at the center/intersection of the Al_3Ti plates. In comparison, there were no such TiC particles at the center of any of the other morphologies of Al_3Ti or any other consistent relationship between the two phases, although

there were instances of TiC on or near the surface of intermetallics, likely being engulfed during the Al_3Ti growth. The TiC particle within the Al_3Ti plates can be seen in red in **Fig. 4.11a**.

Based on these observations we hypothesized that the orthogonal plate morphology of the Al_3Ti is due to a nucleation effect, i.e.- the Al_3Ti heterogeneously nucleates on the TiC particle and grows epitaxially, and not due a growth instability or Ti-solute segregation effect as was seen in the other morphologies. Furthermore, due to non-reciprocal nucleation theory [239] if TiC is nucleating Al_3Ti, then the converse cannot be true, thus determining that for salt-flux reaction synthesis the TiC is made prior to the Al_3Ti and ruling out the indirect route of TiC formation via the breakdown of Al_3Ti (see **Eqn. 4.4**). Examples of overlapping plates of Al_3Ti are found in literature although they are not orthogonal to each other and may be caused by a different mechanism than nucleating on TiC [198]. It has been shown that Al_3Ti can heterogeneously nucleate on TiB_2 [198, 240] and on Al_2O_3 [241] but neither of these resulted in an orthogonal plate structure.

The interfacial normal distribution (IND) of the orthogonal plate structure was calculated as a check for symmetry and to verify that the plates were indeed orthogonal. The zone axis for the calculation is the pink arrow in **Fig. 4.11a**, and the stereographic projection of the IND is shown in **Fig. 4.11b**, with the pink spot being the zone axis at the center. The hot spots along the edge of the projection circle represent that the faces are at a 90° rotation from the zone-axis, and the hot spots themselves are all 90° from one another, confirming that the plates are essentially

orthogonal to one another. There is some amount of noise due to surface defects, such as TiC particles on the surface of the Al_3Ti which were removed for the IND analysis.

The orthogonal plates exhibited a variety of forms. While the basic structure of three orthogonal plates was common, many intermetallic structures had extra planes growing in parallel to basic ones or had extraneous planes unrelated to the main ones. Some of these planes are likely caused by twinning of the Al_3Ti, a common defect in the intermetallic [242, 243], and

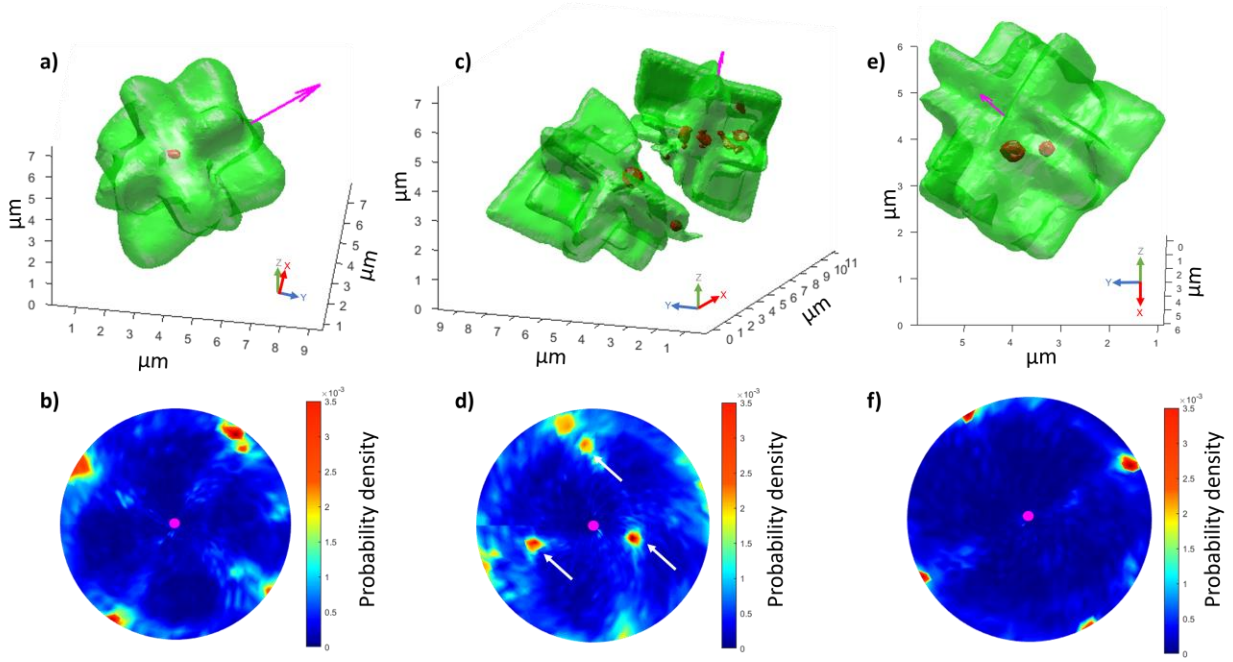

Figure 4.11 Volume rendering of an Al_3Ti intermetallic (green) with a nucleating TiC particle (red) in its center. The pink arrow is the zone axis for interfacial normal distribution (IND) calculations. (*b*) The stereographic projection of the IND for the intermetallic in 2a. (*c*) Volume rendering of two misaligned Al_3Ti intermetallics each with a nucleating TiC particle in their center. The pink arrow in the right-hand intermetallic is the zone axis for IND calculations. (*d*) The stereographic projection of the IND for the intermetallics in 2c, the white arrows point to regions related to the misaligned (left) intermetallic. (*e*) Volume rendering of an Al_3Ti intermetallic with two nucleating TiC particles denoting it was two separate intermetallics which completely coalesced. The pink arrow is the zone axis for IND calculations. (*f*) The stereographic projection of the IND for the intermetallic in 2e.

by stress and defects from the fast cooling rate used. Structures with parallel planes in the main orthogonal directions can be seen in **Figs. 4.11c** and **4.11e**.

Another interesting phenomenon with the orthogonal plate intermetallics was that some had one or multiple of their plates underdeveloped. We hypothesize that this underdevelopment

was due to their proximity to other Al_3Ti intermetallics during growth, thus sharing the Ti-solute field and becoming underdeveloped in the region between the structures. **Fig. 4.11C** shows two Al_3Ti orthogonal plate structures that were growing next to each other but were misaligned from one another. The plates in the region between the two are stunted in comparison to the rest of the structures, as that would be where the Ti-solute field of the two overlapped causing competition in growth. We calculated the INDs of both these structures and have the overlayed stereographic projection in **Fig. 4.11d**. The zone axis was chosen for the right-hand Al_3Ti and is represented as the pink arrow coming out of its top. In **Fig. 4.11d** the hotspots with the white arrows represent the left-hand, or "misaligned", Al_3Ti. It was found that the intermetallic was rotated 15-30° off-axis, depending on the axis, from the Al_3Ti used as the basis for the calculations.

Fig. 4.11e shows a single Al_3Ti structure with two large TiC particles inside it, and two parallel plates in each orthogonal direction. The distance between the two TiC particles was found to be $D_{TiC} = 202\ nm$, using their radii and centroids found from MATLAB, while the distance between each parallel plate was found to be $197\ nm$ ($\pm 21, N = 12$). The correlation between the particle distance and the plate distance implies that this structure was formed by two individual Al_3Ti orthogonal plate structures nucleating on separate TiC particles, and during growth the two impinged on one another and rotated to matching crystal structure until fully coalescing driven by boundary curvature [244, 245]. This rotation could be done by rigid sliding of one intermetallic with respect to the other along their boundary [245]. The IND stereographic projection is shown in **Fig. 4.11f** shows almost perfect alignment of the planes in each direction, and therefore represents how completely the two structures aligned with each other.

We used the intensity values within the TXM data to more thoroughly identify the phases within the TXM data, particularly for identifying the bright particle within the orthogonal Al_3Ti

plates. Using the methodology outlined by Ebner *et al.* [246] we were able to normalize the intensity values of the Al/TiC MMNC sample and yield absolute values by using the linear coefficient values of air and of pure Al along with their measured intensity values from the TXM data (see **Table 4.2**). The Ti solubility in Al at room temperature is low enough that it is reasonable to assume the matrix is essentially pure Al. From these values we were able to create a linear scale to reliably compare the intensity values of present phases with the expected linear attenuation coefficients (**Eqn. 4.7**)

$$\mu_L = aW + b \tag{4.7}$$

Where W is the grayscale intensity value and a and b are constants (7.96×10^{-5} and -70.27, respectively, both are in units of 1/cm).

Table 4.2 Measured intensity values from TXM data with the expected phase identified along with calculated linear attenuation coefficient using the normalized scale for the sample

Expected Phase	**Intensities of TXM Data** (W)	**Linear attenuation Coefficient** (Calculated) (μ_L, 1/cm)
Al (matrix)	3.28E-04	1.90E+02
TiC Core Particle	1.70E-03	1.28E+03
Al_3Ti Plate	7.88E-04	5.56E+02
Al_3Ti Star	8.23E-04	5.84E+02
Air	8.84E-05	1.99E-02

Using this method, we were able to calculate both the theoretical intensity values for all phases which could have formed during the salt-flux reaction synthesis (see **Table 4.1** for possible phases and **Table 4.3** for calculated intensity values) using their theoretical linear attenuation coefficients and also calculate the linear attenuation coefficients for the phases found in the TXM data for direct comparison (see **Table 4.2**). This allowed for direct comparison between phases and direct understanding of the chemistry of the phases in the TXM data.

The results of comparing the theoretical and experimental values are summarized in **Table 4.4**. The top of the table reviews how well the Al, air, and Al_3Ti intermetallic compare

with their theoretical values, while the lower portion compares the values for the core particles with all possible cubic, tetragonal, trigonal, and orthorhombic phases, as all those structures have internal angles of 90° and could possibly explain the orthogonal plate structures. The air and Al have almost no differences as they were used for the normalization function, but for the intermetallics (plate and orthogonal plate structure) there is consistently a difference of ~10% from their theoretical values which could suggest some error in the normalization procedure: a 3rd known phase/datapoint would increase the accuracy of this method. On top of potential error from the method, the differences could come from the intermetallic being off-stoichiometry, or put another way that there is 5-10% more Ti in the intermetallic than the theoretical amount (i.e. $Al_{3-x}Ti_{1+x}$).

Table 4.3 Theoretical intensity values for phases which may be present from the salt-flux reaction synthesis. Values were calculated using theoretical linear attenuation coefficients from [214]

Phase	Theoretical Intensity value (W)
C (graphite)	1.07E-04
Ti (High temp)	1.72E-03
Ti (Low temp)	1.77E-03
$TiC_{(0.95)}$	1.56E-03
Al	3.28E-04
Al_3Ti	7.44E-04
$Al_{2.9}Ti_{1.1}$	7.87E-04
$TiAl_2$	8.74E-04
TiAl	1.12E-03
Ti_3Al	1.47E-03
Al_4C_3	2.93E-04
AlF_3	2.25E-04
K_3AlF_6	4.85E-04
$KAlF_4$	4.14E-04
KF	5.84E-04
K_2TiF_6	6.22E-04
TiF_4	5.66E-04
Air	8.84E-05
F	8.84E-05
K	3.25E-04

More phases were considered for identifying the core nucleating particle within the orthogonal plate structure, as it is feasible that any crystal structure with internal angles of 90°

could have led to the unusual intermetallic structure, even if their axes are not all equal (e.g. trigonal and tetragonal structures). The results in **Table 4.4** rule out a significant amount of the possible phases as their intensities and linear attenuation coefficient values do not match whatsoever with what was measured. The only phases which are remotely close to the experimental values are a high temperature Ti cubic phase and TiC, however the former does not seem likely as the transition to cubic Ti is at T = 882 °C, which is far beyond our experimental operating temperature. Below that transition temperature Ti is hexagonal, meaning it would not lead to the neat 3-fold symmetry of the orthogonal plate structure. Furthermore, we did not find any evidence of pure Ti in the TEM, XRD, or SEM analysis.

Table 4.4 Comparing the differences of the theoretical and experimental values or the linear attenuation coefficients and intensities of the phases found in TXM.

Suggested phase	**Comparing Experimental and Theoretical Linear Attenuation Coefficients** ($\Delta\mu_L, \%$)	**Comparing Experimental and Theoretical Intensities** ($\Delta W, \%$)
Al (matrix)	0%	0%
Al_3Ti Plate	7%	6%
Al_3Ti Orthogonal Plate	12%	11%
Air	1%	0%
Comparing Possible Nucleating Phases (Cubic, Tetragonal, Orthorhombic, Trigonal) with the Measured Core Particles		
Suggested phase	**Comparing Experimental and Theoretical Linear Attenuation Coefficients** ($\Delta\mu_L, \%$)	**Comparing Experimental and Theoretical Intensities** ($\Delta W, \%$)
Al_4C_3	689%	481%
AlF_3	1081%	656%
K_2TiF_6	202%	173%
K_3AlF_6	306%	251%
KAlF4	396%	311%
KF	225%	191%
Ti (High temp)	-1%	-1%
TiAl	56%	51%
$TiAl_2$	105%	95%
TiF_4	238%	201%
$TiC_{0.95}$	9%	9%

By ruling out all of the other possibilities we can safely say that the orthogonal plates of Al_3Ti are nucleating on a core TiC particle, but the match is not perfect. The error between the

experimental and theoretical values of the TiC falls in the same magnitude as what was found for the intermetallics, so it is possible that the difference is from method error. Similar to our discussion with the Al_3Ti analysis, the core TiC particles are likely off-stoichiometry. The theoretical values were calculated for Ti/C at a ratio of 1/0.95 and since the theoretical intensity values were lower than the experimental ones we can safely say that there are far more C-vacancies in the core TiC particle than expected since an increased amount of Ti (or loss of C) would increase the phase's intensity values and linear attenuation coefficient. As discussed earlier, it is common to have large amounts of C-vacancies when creating TiC [121, 122, 247]. A closer examination of the XRD data does suggest that there is a large amount of C-vacancies in the TiC formed through SFRS, although that is discussed more in Chapter 5 (see **Fig 5.4**).

Fig. 4.12 shows the distribution of the TiC particles within the Al matrix in the TXM data, and it was found that the particles followed a log-normal distribution (solid line). The

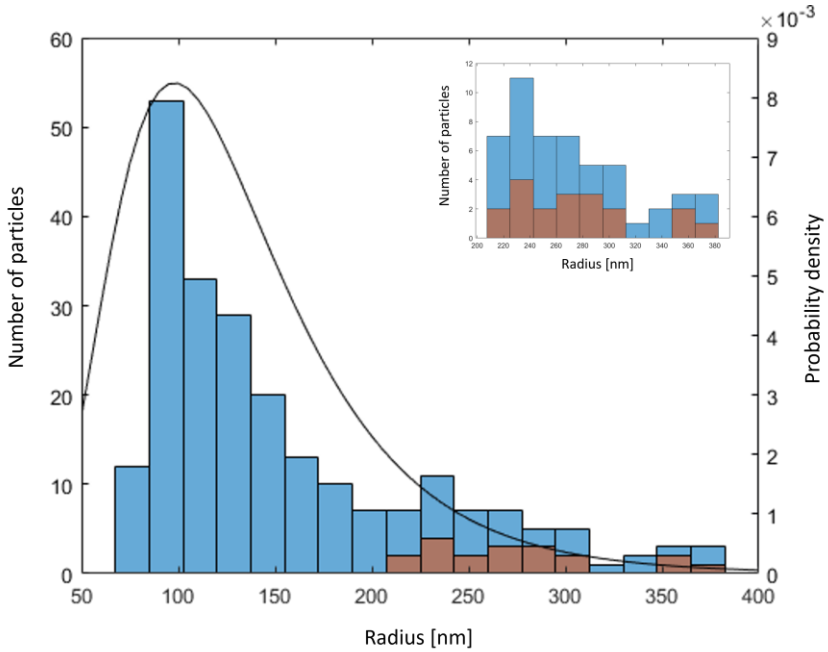

Figure 4.12 A histogram showing the distribution of TiC particle radii in nm. The brown columns represent the TiC found to nucleate the orthogonal structure of Al_3Ti. The range was decided with the TXM spatial resolution as the minimum with the maximum chosen to avoid counting agglomerates of TiC. The inset is a zoom in on the range of particle sizes relating to nucleating Al_3Ti

calculations focused on TiC particles that could be discernable, so particles of R < 50 nm were ignored as they could not be discernable from noise, and particles of R > 500 nm were assumed to be large agglomerates and likewise ignored. The brown overlayed boxes indicate the TiC particles which acted as heterogeneous nucleating spots for the Al_3Ti orthogonal plates, i.e. were found at or near their center. The inset of **Fig. 4.12** shows just the range of bins with these types of TiC included. It was found that the average $R_{TiC}^{avg} = 160\ nm \pm 99$, but the average size of the TiC nucleating the Al_3Ti was $R_{TiC-Nuc}^{avg} = 290\ nm \pm 59$. This suggests that there is a minimum size of the TiC for heterogenous nucleation of Al_3Ti to occur, as suggested by Greer that at a given undercooling there is a minimum particle diameter at which melt inoculants allow a free-growth condition of a secondary phase [248-250]. Using Greer's equation (**Eqn. 4.8**) we can find the expected undercooling (ΔT_{fg}) that would provide free growth of Al_3Ti on TiC.

$$\Delta T_{fg} = \frac{4\gamma}{\Delta S_V d} \tag{4.8}$$

Where γ is the interfacial free energy between the solid nucleating phase and liquid, ΔS_V is the entropy of fusion per unit volume of the nucleating phase, and d is the critical diameter of the nucleant. We used **Eqn. 4.9** to find ΔS_V:

$$\Delta S_V = \frac{\Delta H_{mol}}{T_m} \frac{\rho_{Al_3Ti}}{M_{Al_3Ti}} \tag{4.9}$$

Where ΔH_{mol} is the enthalpy of formation of Al_3Ti (80,000 mJ [251]), T_m is the melting temperature (1613 K), ρ_{Al_3Ti} is the density of the intermetallic (3.4 $\frac{g}{cm^3}$), and M_{Al_3Ti} is the molar mass of the intermetallic (128.81 g/mol). Using these values we found $\Delta S_V \cong 1.3 \frac{J}{cm^3 K}$. Then using $\gamma = 0.074 \frac{mJ}{cm^2}$ for Al_3Ti and liquid Al [252] and $d = 4x10^{-5}$ cm, as found in the TXM data, we found a required undercooling of $\Delta T_{fg} \cong 6$ °C. This would imply a liquidus line for

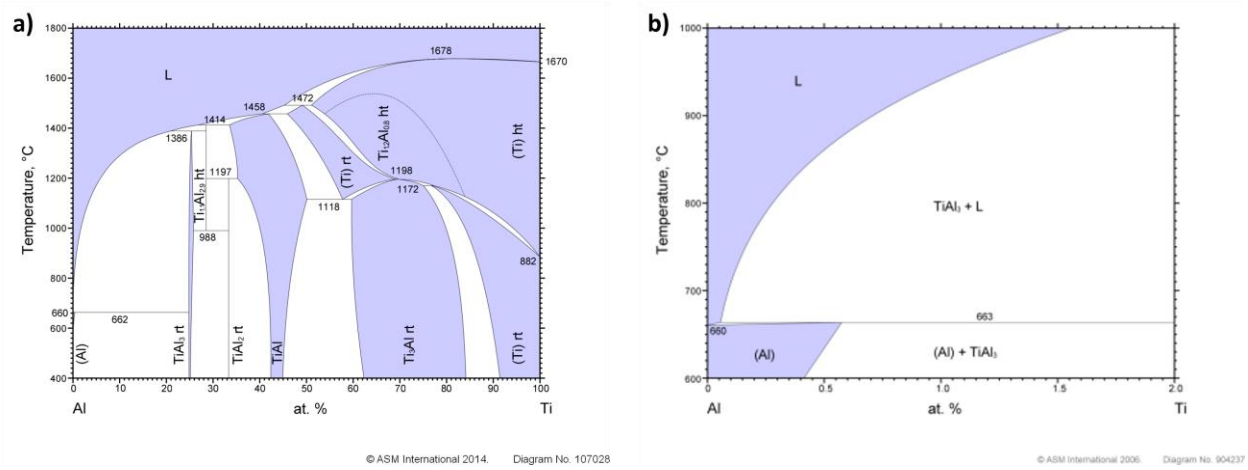

Figure 4.13 Phase diagrams for the Al-Ti binary system. a) The full Al-Ti phase diagram and b) The Al-rich side of the Al-Ti phase diagram. Both are from [212]

Al_3Ti and liquid Al at 856 °C which coincides with 1wt% Ti in the Al matrix prior to nucleating the intermetallic. This would imply that about one quarter of the Ti from the K_2TiF_6 did not form TiC and instead went into the Al matrix during the reaction, reaching the Ti solubility limit at the melt temperature. This conclusion reasonably fits the volume fraction of TiC and Al_3Ti we found in the TXM data, thus reaffirming the amount of Ti which did not form TiC. A reference Al-Ti phase diagram and the Al-rich side of the diagram are shown in **Fig. 4.13**.

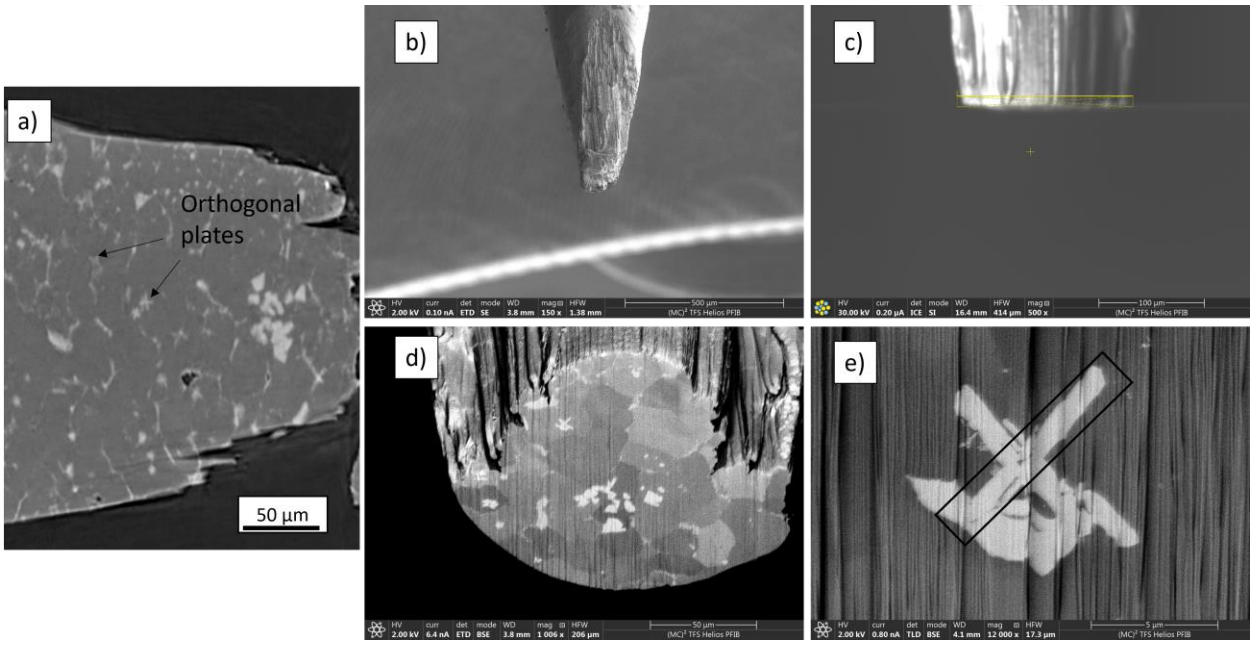

Figure 4.14 (*a*) µ-CT scan of the Al-TiC MMNC, the red arrows point out potential orthogonal plate structures of Al_3Ti. (b) SEM of the original 1 mm pillar (c) The pillar cut down to the approximate location of the desired structure. (d) SEM of the surface exposed with the FIB cut. (e) SEM of the orthogonal plate Al_3Ti used for the TEM specimen, the black box shows where the TEM sample was cut from.

Using the µ-CT data we were able to discern locations of orthogonal plates in the sample to be analyzed with STEM via a precise PFIB lift-out, with the goal of capturing a nucleating TiC particle at the center of an Al_3Ti orthogonal plate structure. The process is shown in **Fig. 4.14**. Unfortunately, we found that this elegant approach was not effective for finding a perfect feature for TEM sample due to the resolution limit of the µCT. After initial TEM specimen were made this way we decided to perform a TEM lift-out from a bulk sample polished for SEM imaging

TEM analysis is shown in **Fig. 4.15**, focusing on the interface between the Al_3Ti and TiC particles. HRTEM analysis found that the interface between the Al3Ti and TiC phase was almost completely coherent, as shown in **Fig. 4.15**c. Fast Fourier transformation (FFT) patterns from the Al_3Ti and TiC regions are shown in **Figs. 15d** and 15**f**, respectively, while respective simulated diffraction patterns are shown in **Figs. 15e** and **15g** with zone axes of $[10\bar{1}]$ for Al_3Ti and $[\bar{1}\ \bar{2}\ 3]$ for TiC. We found that the materials were highly off axis, so getting a perfect diffraction from

them was not achievable. Since the Al_3Ti FFT pattern was a single line we could only index it by d-spacing, and found the measured d-spacing is 3.62 Å which matches closely with its (1 0 1) plane [253]. The TiC pattern we were able to match with simulated length and angle ratios using SingleCyrstal 4 (CrystalMaker Software Ltd.). The simulated FFT for the TiC identified the planes as (111) or ($\bar{4}$20). As these crystals were off a main zone axis the plain identifications are reasonable estimates but may not be exact.

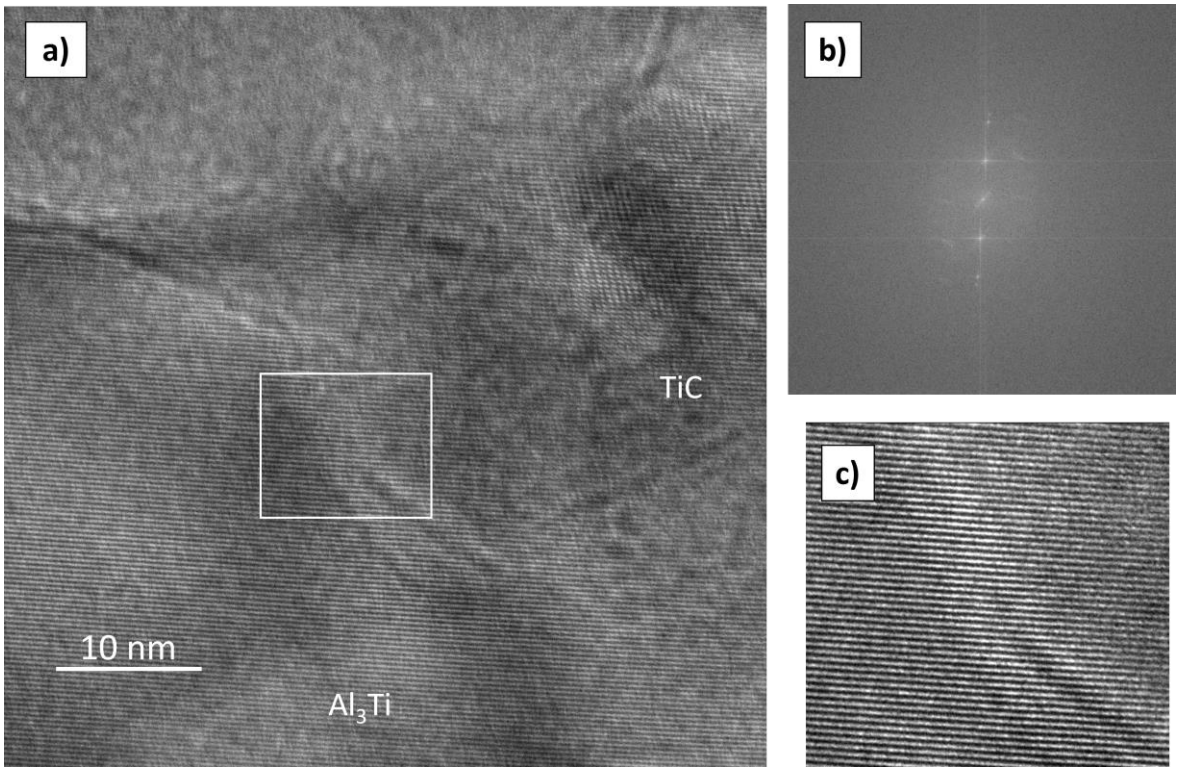

Figure 4.15 TEM analysis of TiC particles within the Al3Ti orthogonal plate structure. a) TEM showing one side of a split Al_3Ti arm with Al between the plates, small TiC particles can be seen at the interface of the phases. The Dotted orange line roughly separates the two phases. b) HRTEM magnifying the region of the red box in a) showing the interface of Al_3Ti and a TiC particle. c) A magnified region of the white box in b) showing coherent planes across the Al_3Ti/TiC interface. d) and f) show fast Fourier transformation patterns from the Al3Ti region (blue circle) and TiC (orange circle), respectively. e) and g) show simulated diffraction patterns from Al_3Ti (e, blue outline) with a zone axis of roughly [10$\bar{1}$] and TiC (g, yellow outline) with zone axis [$\bar{1}$ $\bar{2}$ 3].

While this TiC particle isn't the core particle nucleating the intermetallic, it is a suitable equivalent to prove that the Al_3Ti can be coherent and therefore likely epitaxial with the carbide phase. This smaller particle impinged on the intermetallic surface and rotated to reduce its

surface energy. We made multiple attempts to capture the nucleating particle but were unable to capture one clearly likely because the thinning thickness of a single PFIB pass was nearly the thickness of the nucleating particle.

.**Fig. 4.16a** shows the Al_3Ti cross section of the STEM sample, the Al_3Ti is dark gray, TiC are small black dots, and the Al matrix is light gray. This intermetallic turned out to have significant splitting of the intermetallic plates, as many of the orthogonal plates were found to be parallel plates with Al matrix and TiC particles in between them. **Fig. 4.16b** is a HAADF image of the box in **Fig. 4.16a** showing clusters of TiC (marked with red arrows) trapped in the intermetallic. **Figs. 4.16c-e** are HAADF spectrum images which verify that the particles are high in Ti and C. Some examples of the entrapped Al within Al_3Ti were found in the TXM data, although for simplicity this phase was left out of the 3D visualizations (**Figs. 4.9** and **4.11**).

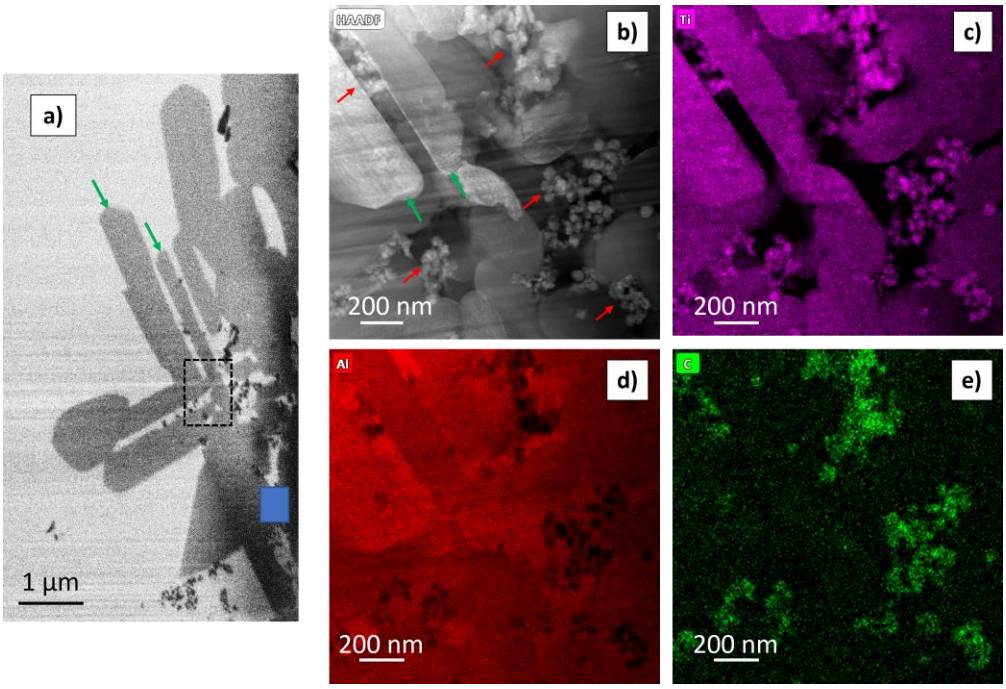

Figure 4.16 (*a*) Secondary electron SEM of the TEM sample, the light gray is the Al matrix, darker gray is Al_3Ti, and the black specks are TiC. (b) HAADF imaging of the boxed section of 6a. The red arrows point to clusters of TiC, and the green arrows point to parallel plates of Al_3Ti also found in 6a. (c) Ti spectrum of 6b. (d) Al spectrum of 6b. (e) C spectrum of 6b.

The STEM imaging revealed that the TiC particles have dual effects on the morphology of Al_3Ti. First, TiC particles above a critical radius of curvature act as nucleating sites for the Al_3Ti, thus forming the orthogonal plate structures. Secondly, the smaller TiC particles perturb the growth process of the intermetallic, similar to how grain refining particles split dendrite arms during growth [193, 204-206]. The presence of the carbides disrupts the local solute field, as the amount of solute must be in equilibrium with TiC, compared to being the normal distribution of solute in the bulk of the matrix [254]. Thus, when the growing arms of the Al_3Ti approach small TiC particles they branch and grow into the more solute-rich liquid around them. Due to the anisotropy of the Al_3Ti structure these plates continue to grow in parallel and never coalesce.

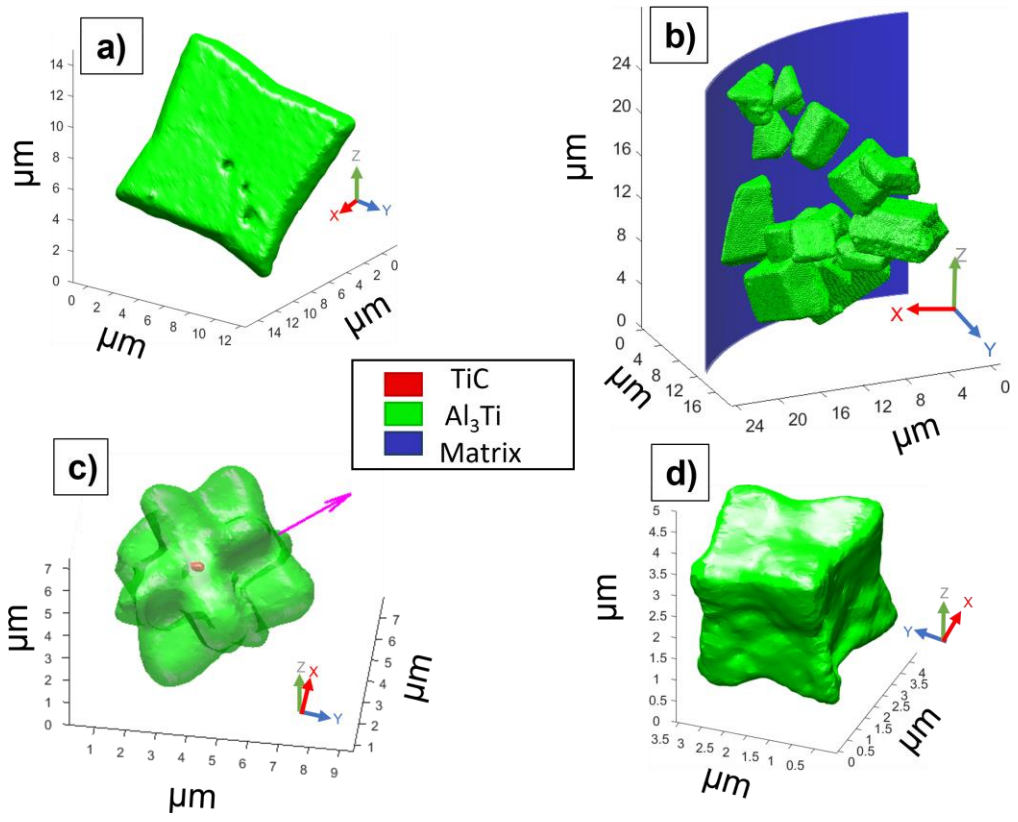

Figure 4.17 An overview of the different Al_3Ti morphologies found in Chapter 4. (a) The plate-like morphology is caused by a faster cooling rate during solidification. (b) The blocky morphology is caused by a slower cooling rate during solidification. (c) The orthogonal plate morphology is caused by Al_3Ti heterogeneously nucleating on a TiC particle and growing epitaxially from it. (d) The cuboid morphology is from the intermetallic growing in a Ti-poor region of the melt

The green arrows in **Fig. 4.16a** and **4.16b** point out two parallel plates of Al_3Ti whose growth was perturbed by the presence of TiC. This phenomenon can be seen in 2D with SEM (**Fig. 4.8a**) and in 3D with the TXM visualizations (**Fig. 4.11c**). Another corollary of this finding is that the TiC particles were not homogeneously dispersed in the melt: single plates of Al_3Ti found in the TXM data did not display this splitting behavior, meaning that they nucleated in regions that had homogeneous Ti-solute fields and neither large nor small TiC particles making their growth unperturbed. It is clear from the TXM and SEM data that in the as-solidified state most of the TiC particles are agglomerated in the grain boundaries, as is common for MMNCs including those made with salt-flux reactions [42, 54], but this insight into the as-made liquid composite helps further guide the understanding of this reaction. An overview of the different Al_3Ti morphologies and their causes outlined in this chapter can be found in **Fig. 4.17**, and the flowchart in **Fig. 4.18** reviews the different ways TiC affects the other phases from the melt.

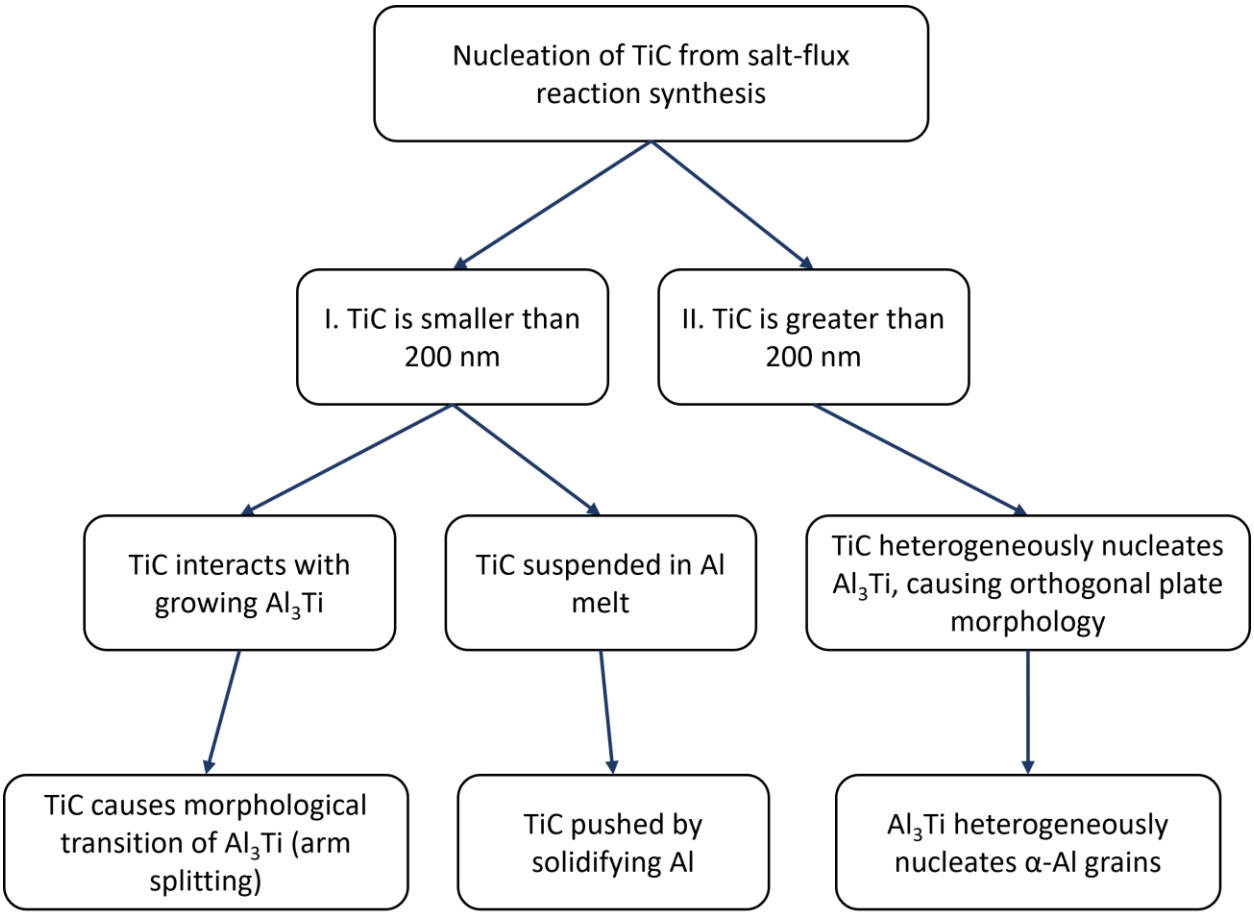

Figure 4.18 Schematic of the different interactions TiC can have with the phases present from salt-flux reaction synthesis

4.4 Conclusions

We have analyzed *in situ* Al-TiC MMNCs produced *via* salt-flux reaction synthesis. A multi-scale, multi-modal approach was taken to study the microstructure using SEM, TEM, and TXM (2D and 3D) to better understand the TiC particle formation mechanisms and its effects on the final microstructure. We found a significant amount of nano-sized TiC particles and Al_3Ti intermetallics formed from this process. Using the TXM and TEM data we found that there were multiple distinct morphologies of the Al_3Ti caused by different cooling rates, local Ti

concentrations, and nucleation method. We found that intermetallics with the orthogonal plate structure are a direct result of the Al_3Ti nucleating heterogeneously on then growing epitaxially from TiC and were able to find the critical radius of TiC for this nucleation to occur. We also found that the TiC particles led to the splitting of Al_3Ti arms during growth, thus showing a secondary effect the carbide had on the intermetallic. Due to non reciprocal heterogeneous nucleation theory we were able to determine that the TiC is formed directly from the salt-flux reaction and rule out indirect formation mechanisms which require Al_3Ti as an intermediary step. This data and analysis can lead to a more informed production of MMNCs via salt-flux reaction synthesis.

CHAPTER 5

Salt-Flux Reaction Synthesis: Studying the Effects of Si on Formed Microstructure and Secondary Phases

5.1 Introduction

Our investigation of salt-flux reaction synthesis (SFRS) with pure Al (see Chapter 4) proved that it was a promising method to create *in situ* Al-based MMNCs. This approach for MMNC production promises ease of use and has potential to be integrated into a foundry workflow since surface fluxes are already an industry practice. However, most MMNCs generated via SFRS have been made in pure Al [100-102, 107, 113, 255-257]. Although there has been some work using commercial alloys such as A356 [258], wrought 6351 [112], 6061 [259], and 7075 [260], much of these works focus on creating intermetallics (e.g. Al_3Ti) as the reinforcing phase. There has thus far been no systematic study of how common alloying elements (e.g. Si, Cu, Mg, Mn, Zn, Sn, Ni) affect the formation of TiC via salt-flux reaction synthesis, or how solute elements alter which phases form during processing.

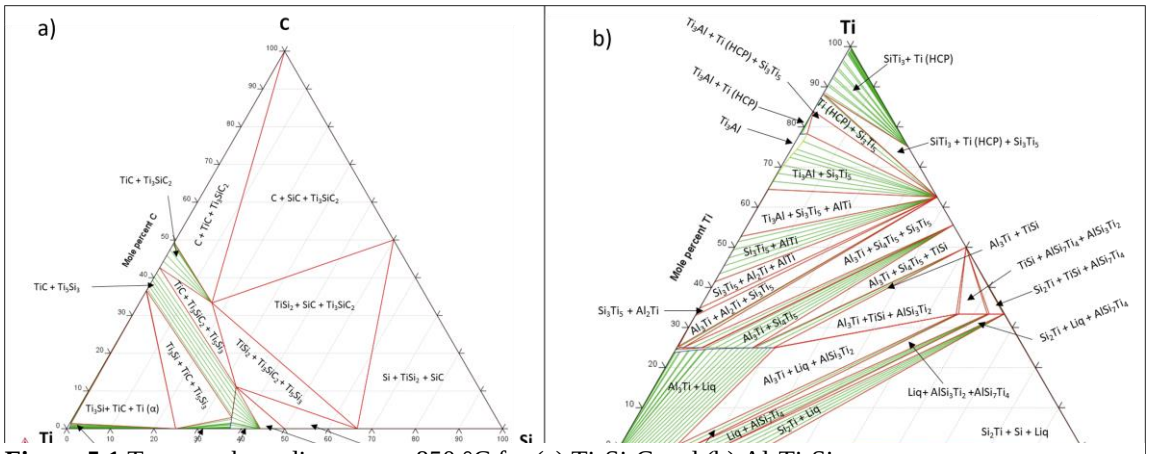

Figure 5.1 Ternary phase diagrams at 850 °C for (a) Ti-Si-C and (b) Al-Ti-Si

Si is a good solute candidate to test first as it is commonly added in large amounts to commercial Al casting alloys to improve castability and liquid flow (e.g. A356 has 7 wt% Si). Furthermore, there is evidence that Si influences both TiC and Al_3Ti, regardless of how the materials were made. Sample ternary phase diagrams of Al-Ti-Si and Ti-Si-C are shown in **Fig. 5.1**. Reese *et al*. found hexagonal TiC plates (**Fig. 5.2**) formed from SFRS and suggested the morphology was either from off-stoichiometric Ti/C ratio in the carbide or an effect of the particles forming in the presence of Si forming MAX phases [116].

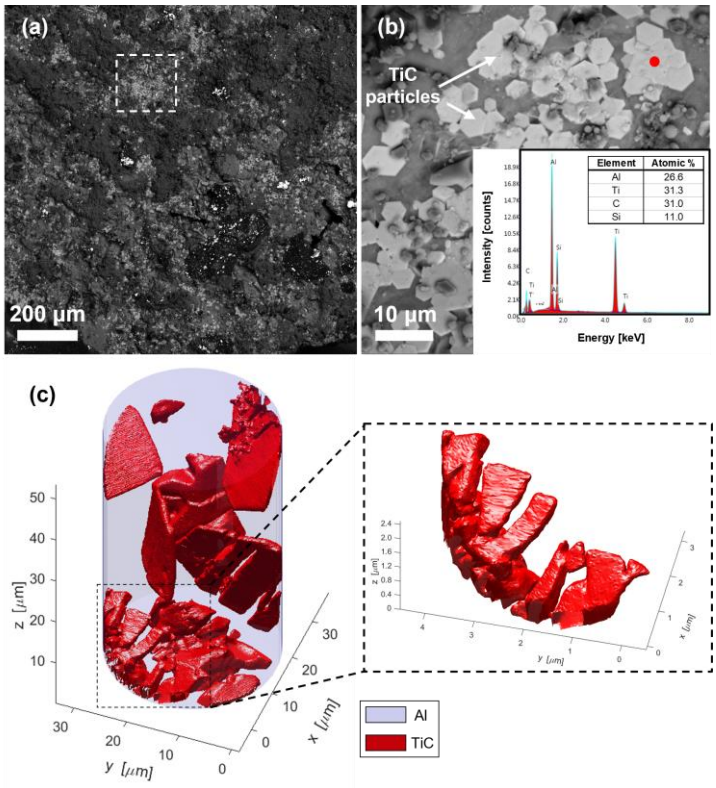

Figure 5.2 (a) BSE SEM of the sample surface of an Al-TiC MMNC made via salt-flux reaction synthesis, (b) Higher magnification of the boxed region in a) showing carbide platelets with an inset spot EDS spectrum (c) 3D visualization of TXM data showing hexagonal TiC platelets in red and the Al matrix in blue, with a higher magnification of one particle shown in the inset (from [116]).

MAX ($M_{n+1}AX_n$) phases are a ternary material where M is an early transition metal, A is a metal from groups 13 or 14 of the periodic table, and X is either C or N, forming phases such as Ti_3AlC_2 or Ti_3SiC_2, commonly with hexagonal plate morphologies [261-266]. MAX phases

are of interest as they share a mixture of metal and ceramic properties, including good machinability, low hardness, high elastic modulus, low density, superior thermal shock resistance, high strength at elevated temperatures, low thermal expansion coefficient, high oxidation resistance, self-lubricity, and exemplary electrical and thermal conductivities [261, 262, 264, 267, 268]. Often MAX phases are made via self-propagating high-temperature synthesis [264, 267, 268] or via additive manufacturing [265].

The Al_3Ti intermetallics have also been shown to be affected by the presence of Si: Si can substitute for Al in the Al_3Ti structure typically 9-12.5 wt%, resulting in a range of chemical compositions and lattice parameters, which can be written as $Ti(Al,Si)_3$ [269-271]. Ma *et al.* formed Al/Al_3Ti composites by putting K_2TiF_6 on top an Al – 7 Si alloy, and found $(Al,Si)_3Ti$ zones within blocky Al_3Ti structures that seemed to break up the intermetallic (see **Fig. 5.3**) [270, 272, 273].

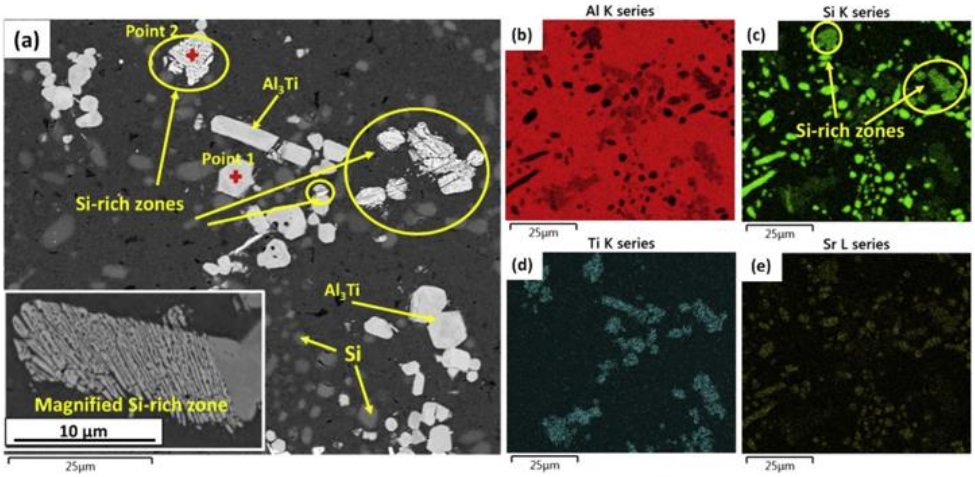

Figure 5.3 (a) SEM micrograph of Al3Ti and zones affected by Si, (b-e) EDS mapping of Al, Si, Ti, and Sr, from [266]

Other possible intermetallics at the Al-rich corner of the Al-Ti-Si phase diagram are τ_1 written as $Ti_7Al_5Si_{12}$ which can contain 17-42% Si, τ_2 written as $Ti(Al, Si)_2$ which can have 38-46% Si or 10-10 at% Al, or the ternary compounds $AlSi_3Ti_2$ and $AlSi_7Ti_4$ [270, 271, 274]. It has been suggested that $TiSi_2$, $Ti(Al,Si)_2$, $AlSi_7Ti_4$, and $AlSi_3Ti_2$ have the same crystal structure and

essentially equivalent lattice parameters [272, 274-276], although more work should be done to experimentally verify these claims, and they are still separated for thermodynamic analysis (e.g. see **Fig. 5.1b**). When called for by the results we will first name possible phases and decide upon a single nomenclature for any Al-Ti-Si phases.

Clearly there is a significant effect Si can have on TiC and Al_3Ti: its presence during the *in situ* production of MMNCs via salt-flux reaction synthesis must be studied more in depth to better understand how varied amounts of Si in the matrix affect the final microstructure and properties of the formed MMNC. We used synchrotron-based X-ray nanotomography (TXM) to visualize the microstructure of *in situ* $Al_{1-x}Si_x$/TiC (x = 0, 1, 4, 7 wt%) MMNCs in 3D with nanoscale resolution to gain a deeper understanding of their microstructure and the effects of forming MMNCs in the presence of Si.

5.2 Experimental methods

5.2.1 Sample preparation and characterization techniques

The *in situ* MMNC samples were made with four different matrix alloys: pure Al 99.99% (2-5 mesh, Belmont Metals), Al - 4.38 wt% Si (Eck Industries), Al – 6.72 wt% Si (Eck Industries), and Al – 1 wt% Si made by diluting the Al – 4.38 wt% Si alloy with pure Al shot. For the purposes of this work the samples will be referred to as pure Al, Al-1Si, Al-4Si, and Al-7Si. The salt-flux reaction synthesis experiments, metallographic sample preparation, and TXM sample preparation were all done in the same manner as outlined in Section 4.2.1. Similarly, characterization of the samples using TXM, SEM, and XRD followed the same procedure as Section 4.2.1. A reference Al-TiC sample was made using self-propagating high-temperature synthesis following the procedures outlined in [277], since this *in situ* method is proven to generate TiC particles with Ti/C in near-stoichiometric ratio.

TEM and STEM analysis on the Al-7Si MMNC sample was conducted at The Ohio State University by Dr. Jiashi Miao using an FEI Tecnai F20 TEM, operating at 200 keV and an FEI Tecnai G2-30 TEM, operating at 300 keV. Atomic resolution HAADF-STEM images were taken using Thermo Scientific Themis Z probe corrected S/TEM, equipped with a quad-silicon drift detector (Super-X) , and working at an accelerating voltage of 300 keV.

Samples for nanomechanical characterization were sectioned from the bulk material to a size of less than 2.5 cm in the length and width, and less than 1 cm in height, then glued to SEM stubs using Crystalbond™. These samples were hand-ground using SiC grinding sheets (340, 600, 1200 grit), then polished using monocrystalline diamond suspensions (9, 3, 1 µm, MetaDi by Buehler Ltd., Lake Bluff, IL). Since these samples were ground and polished by hand they were glued to the SEM stubs to improve grip and maneuverability. Care was taken to ensure the samples were as flat as possible, both for improved testing accuracy and to prevent any danger to the testing probe. Once the samples were polished to a mirror finish they were removed from the stub with mechanical force, with care not to scratch the surface. Samples were sonicated in acetone to remove Crystalbond™ residue, then sonicated in ethanol.

Nanomechanical characterization was done on a Hysitron TI-950 Triboindenter (Bruker) using a standard dynamic mechanical analysis (DMA) transducer equipped with a standard Berkovitch diamond indentation probe. Samples were glued to the stage using superglue, ensuring that glue only contacted the edges of the sample and didn’t get in between the bottom of the sample and the stage, which could decrease accuracy of results. A quasistatic trapezoid load function was used for indentation, with an loading and removal time of 5 seconds each and a dwell time of 2 seconds, and a peak force of 8000 µN. Each sample was evaluated at 16 points, the machine automatically tested a grid of 4 x 4 points each 30 µm apart. Mechanical properties

were determined from the unloading curve using 95% to 20% of the peak load. Data from these tests was analyzed using Bruker's TriboScan Analysis software (V 9.8.1.3). Due to the porosity of the materials some of the datapoints were removed as low outliers, the actual number of datapoints used per calculation can be found in **Tables 5.1** and **5.2**.

5.3 Results

5.3.1 Si effects on carbides: Microstructure characterization and discussion

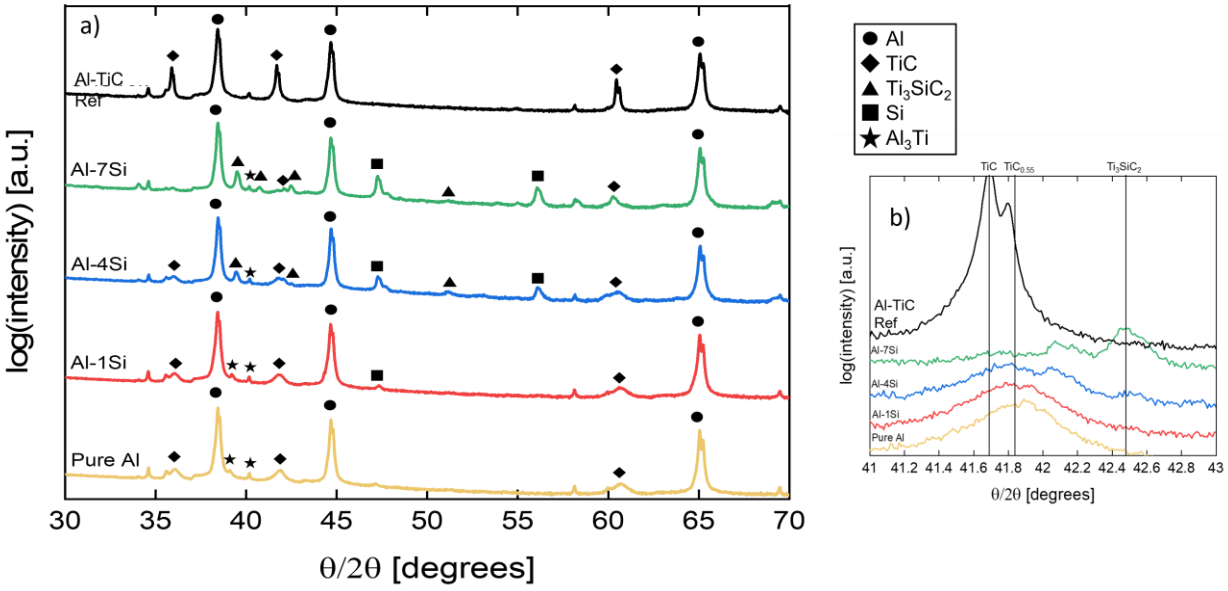

Figure 5.4 (a) X-ray diffraction spectra for the $Al_{1-x} - Si_x$/ TiC samples compared with an Al/TiC reference (b) The TiC peaks magnified to show their shift to the right

The XRD results from the MMNCs are shown in **Fig. 5.4**. While all the samples showed peaks for TiC, the Si containing samples had peaks for Si and the Al-4Si and Al-7Si spectra had peaks for Ti_3SiC_2 as well. Zooming in on the TiC peak around 41° we can see that all of the MMNCs made via SFRS have the peak shifted to the right, which indicates sub-stoichiometric C/Ti ratio in the carbide (see **Fig. 5.4b**). The shift seems to be consistent regardless of the amount of Si present.

Examples of the formed reinforcement are shown in **Figs. 5.5** and **5.6**. The carbides formed in the 1 wt% Si alloy are still spherical TiC (**Fig. 5.5a**), but as Si is added into the matrix there is a shift what phases are formed. **Figs. 5.5b** and **5.5c** both show regions of spherical TiC, but the majority of what was formed appear to be clusters of hexagonal carbides. In SEM it is difficult to tell that the materials are hexagonal plates, and while there are a few examples in 2D, the TXM 3D visualizations make the morphology clear (see **Fig. 5.7b**). It is important to emphasize that regardless of the Si content there are spherical TiC found near or within the clusters of hexagonal carbide plates, as that will guide our later discussion on formation mechanisms.

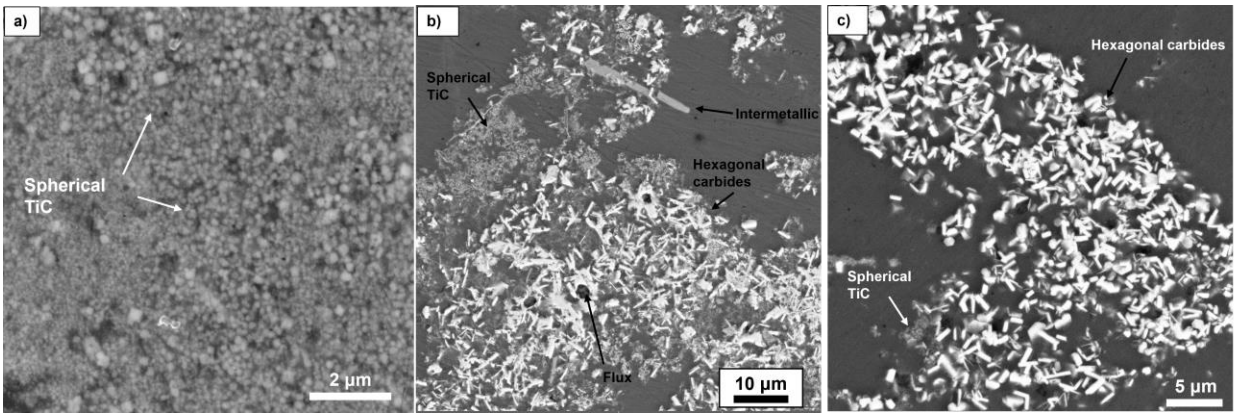

Figure 5.5 (a) SEM of a cluster of spherical TiC within an Al-1si MMNC (b) SEM of Al-4Si showing spherical TiC and hexagonal carbides (c) SEM of Al-7Si showing primarily hexagonal carbides

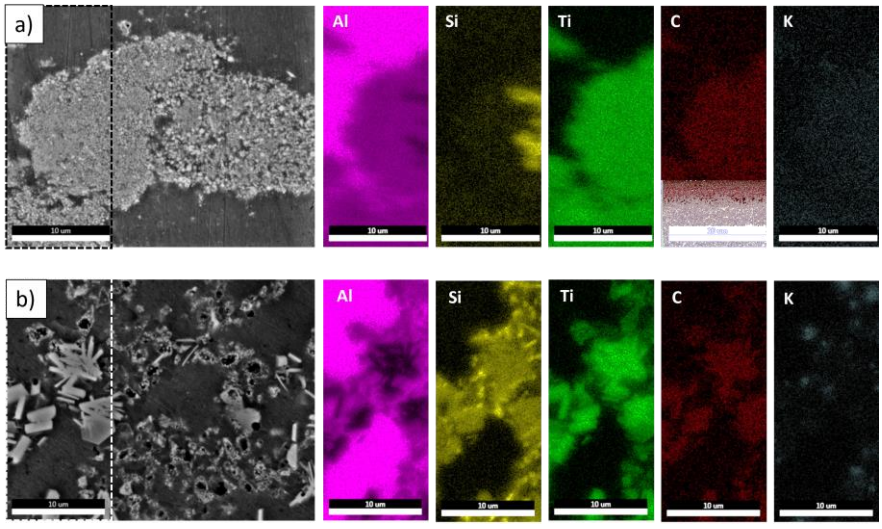

Figure 5.6 EDS mapping for (a) Cluster of TiC in Al-1Si (b) Hexagonal plates in Al-7Si

EDS maps of 1 and 7 wt% Si reinforcing phase are shown in **Fig. 5.6**, both of which show strong signals for Ti and C. In **Fig. 5.6a** there is a faint outline of Si within the cluster of TiC particles, which indicates even small amounts of Si will be incorporated into the TiC reinforcement. The bright regions of Si are likely from an Si-rich phase under the cluster, as it would also be found within the grain boundary region of the MMNC. In contrast, the hexagonal plates show very strong Si signal, which means there is far more Si present in them.

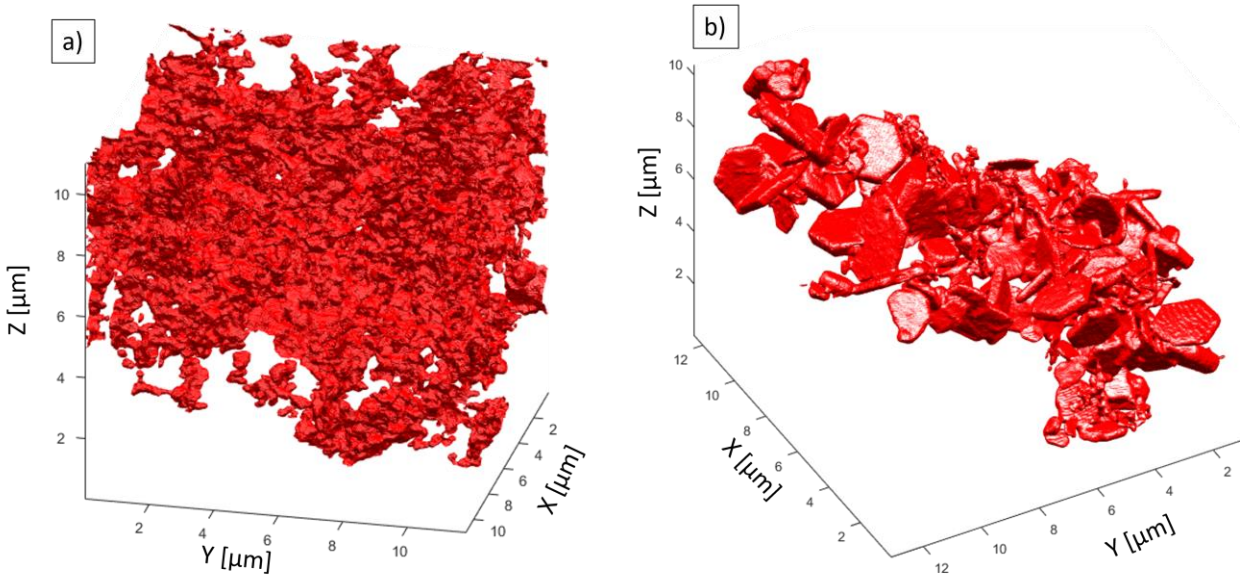

Figure 5.7 3D visualizations of (a) Spherical TiC in Al-1Si and (b) Hexagonal plates of carbide in Al-7Si

Demonstrative 3D visualizations of the TXM data are shown in **Fig. 5.7** for 1 and 7 wt% Si composites. The data was chosen as regions which exhibited only the Ti-C bearing phase and no intermetallics, in order to generate clean visuals. In the 1 wt% Si sample it is difficult to see any individual TiC particles due to their small size and the nature of them clustering together (**Fig. 5.7a**). What cannot be seen in the 2D image is the amount of Al (shown as empty space in the visualization) there actually is: that particular data set is only 13.2 vol% TiC. In contrast, **Fig. 5.7b** shows a 3D visualization of 7 wt% MMNC, where instead of particles there are clustered hexagonal plates. The length, thickness, and aspect ratio (edge length divided by thickness) of the hexagonal plates are shown in **Fig. 5.8**. Unfortunately, the plates often overlap, so there were

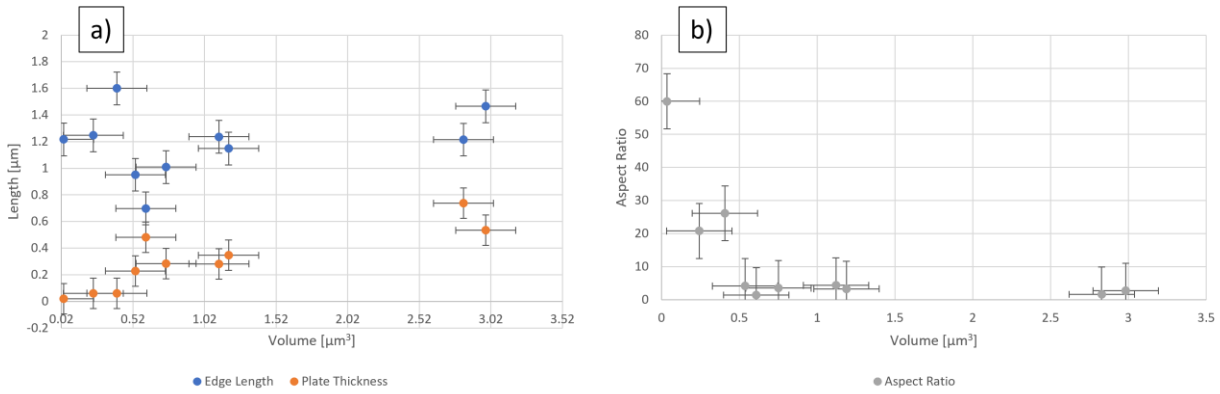

Figure 5.8 (a) Edge length and plate thickness of the hexagonal plates from segmented TXM data vs plate volume (b) Aspect ratio (Edge length / plate thickness) of the hexagonal plates vs volume

few opportunities for an automated process and hand-measurement was required for these values. As expected the thickness and length of the plates increased with increasing volume, but their ratio leveled out at a certain point, likely owing to the anisotropy of the phase.

Results from the TEM analysis clarifies the phases present in these clusters of reinforcement, and can be seen in **Fig. 5.9**. High-angle annular dark field imaging in **Figs. 5.9a** and **5.9b** show clusters of both clusters of spherical TiC and overlapping hexagonal plates. Chemical line analysis of the spherical clusters indicates that they are indeed TiC and very low in Si content, while the analysis of the hexagonal plate shows far more Si present (**Figs. 5.8c** and **5.9d**, respectively). Finally, the diffraction analysis and atomic resolution of the hexagonal plate cinch its identity as the MAX phase Ti_3SiC_2. The crystal structure of TiC and Ti_3SiC_2 is shown in **Fig. 5.10** (made in CrystalMaker, data from [278, 279]).

An important question that has yet to be solved is the nature of the Ti_3SiC_2 formation during the SFRS processing. The spherical TiC particles and hexagonal Ti_3SiC_2 plates are often found near one another in both the 4 and 7 wt% Si alloys, which at first might suggest that one phase is related to the formation of the other but since the analysis has been done postmortem, it is

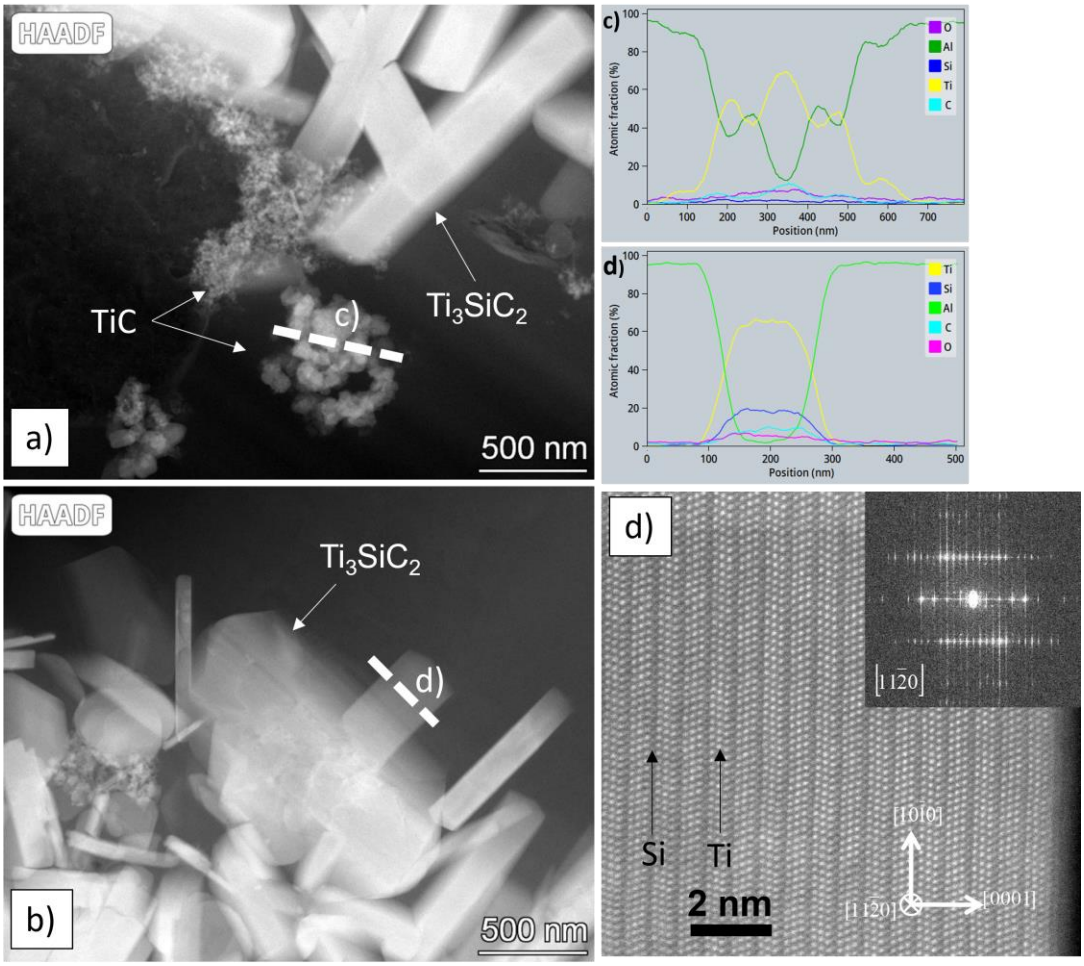

Figure 5.9 TEM analysis of the Al-7Si MMNC sample (a, b) HAADF images of a hexagonal Ti_3SiC_2 and TiC clusters (c, d) Chemical line scans from a) and b) showing the amount of Ti, Si, Al, C, and O in the lines, (d) HRTEM showing the Si and Ti atomic planes of the MAX phase, with the diffraction pattern in the inset

difficult to know if the two phases were adjacent during their formation and melt. Since small particles often get pushed to the final liquid region of a solidifying melt it is likely that the phases are formed separately but they wind up in the final location of the MMNC via pushing by the solidification front [280-282]. There are many factors involved in the pushing or capture of particles by a solidification front, some of which will be discussed further in Chapter 6. It is generally understood that during SFRS processing the TiC particles form at the interface the liquid flux layer and the Al melt [100], but there has yet to be similar work showing if Ti_3SiC_2 can form in a similar manner at the flux/Al interface or if the plates are formed via solute Ti and

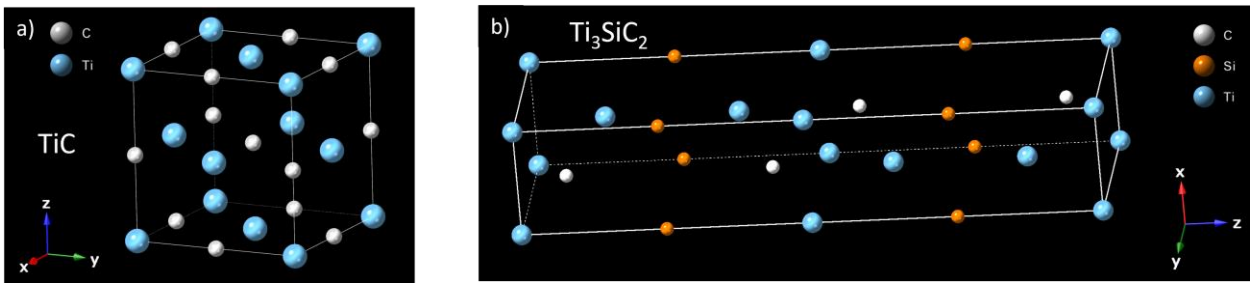

Figure 5.10 Crystal structures of (a) TiC and (b) Ti_3SiC_2

C interacting with Si in the bulk of the melt. This question will not be addressed in this work, but it is one of the standing hypotheses for the formation of Ti_3SiC_2.

Alternatively, it has been shown in literature Si has a significant impact on TiC, so it is possible that precipitated TiC either grows into Ti_3SiC_2 in the presence of Si or there is some unknown solid-state transformation occurring. The fact that the TiC particles are sub-stoichiometric supports this hypothesis the C-vacancies of TiC_x allow for Si incorporation into the lattice, thus decreasing the energy barrier for Si diffusion and leading to a significant amount of defects in the carbide (e.g. twinning, stacking faults, increased dislocations) [283-286]. There is some work which suggests that Si favors interstitial sites around Ti or surrounding C-vacancy sites [287].

Studies suggest that Si incorporation into TiC lower the stacking fault energy barrier, and that stacking faults lower the diffusion barrier of Si and C-vacncies, typically on the (111) plane, and that at a certain Si-density the structure shifts from cubic TiC to a hexagonal structure [262, 283, 285, 286]. Ding *et al.* suggested that the hexagonal structure is caused by Si adsorbing to the TiC surface then causing anisotropic growth into a hexagonal morphology and not from a structural shift [288, 289]. Furthermore, TEM observations of Ti_3SiC_2 have found segregation of Si and C vacancies into twin boundaries within the TiC lattice, forming periodic layers of Si and TiC_x [285, 286, 290]. More work must be done to see if the Ti_3SiC_2 is formed directly from the

flux reaction, indirectly through affecting TiC, or through another route which we have not yet considered.

5.3.2 Si effects on intermetallics: Microstructure characterization and discussion

The XRD results in **Fig. 5.4** show some peaks for Al_3Ti regardless of the Si content, although there were no clear peaks for ternary Al-Ti-Si phases, potentially due to peak overlap. SEM analysis of the samples found any amount of Si addition causes a change in the intermetallic 2D morphology from solid needles to branching or armed structures. Compare the intermetallics formed in the 1 wt% Si alloy in **Fig. 5.11** to those formed in the absence of Si (**Fig. 4.7a**, blue arrows). The intermetallics seem to be consistent between the 1, 4, and 7 wt% Si samples, which indicates that whatever phase is formed is stable in a wide range of Al and Si concentrations. An EDS map of one structure from an Al-7Si sample (**Fig. 5.11d**) shows a positive signature of Si within the intermetallic, and spot EDS (**Table 5.1**) further explains the makeup of the intermetallic as $(Al,Si)_2Ti$.

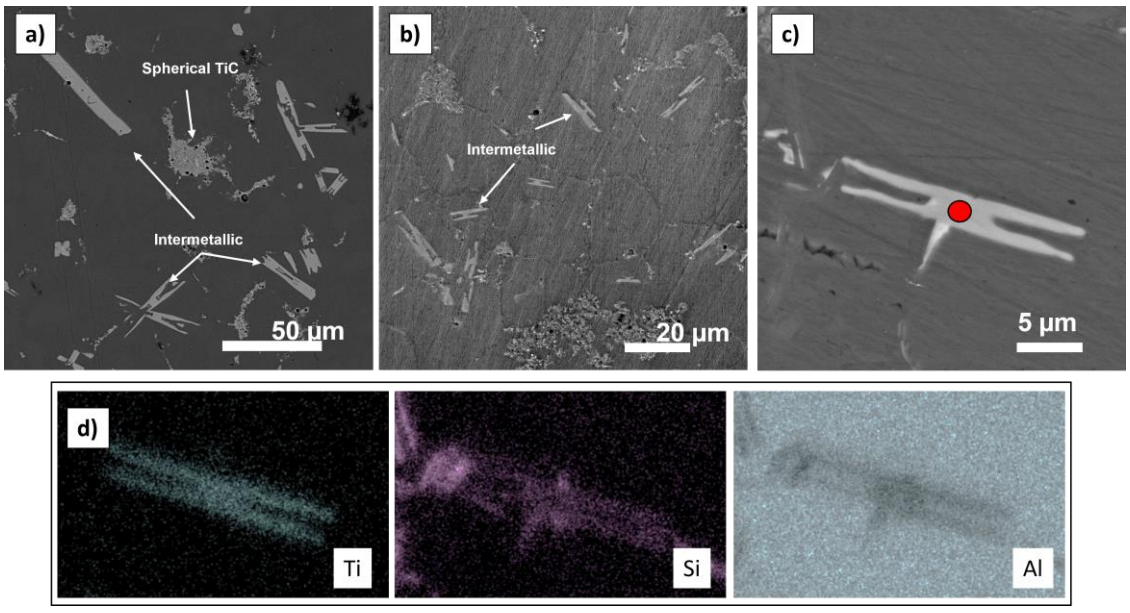

Figure 5.11 Representative microstructure and intermetallics in (a) Al-1Si, (b) Al-4Si, and (c) A magnified image of the an intermetallic in Al-7Si (d) An EDS map for Ti, Si, and Al of c)

Table 5.1 EDS analysis from the red point in Fig. 5.11c

Element	Weight %	Atomic %
AlK	27.94	42.15
SiK	10.89	15.78
TiK	32.07	27.25

A few interesting results came from the TEM analysis of the Al-7Si composite (**Fig. 5.12**). First, diffraction and a line EDS scan identify the intermetallic phase as $Ti(Al,Si)_2$ (see **Figs. 5.12c** and **5.12d**, respectively). What's more, there are clear Si regions adjacent to and butting up against the intermetallic. The atomic resolution of the intermetallic shows clear alternating layers of the Ti and (Al,Si) planes (**Fig. 5.12d**). The crystal structure of Al_3Ti and $TiSi_2$ can be compared in **Fig. 5.13** (made in CrystalMaker with data from [291, 292]).

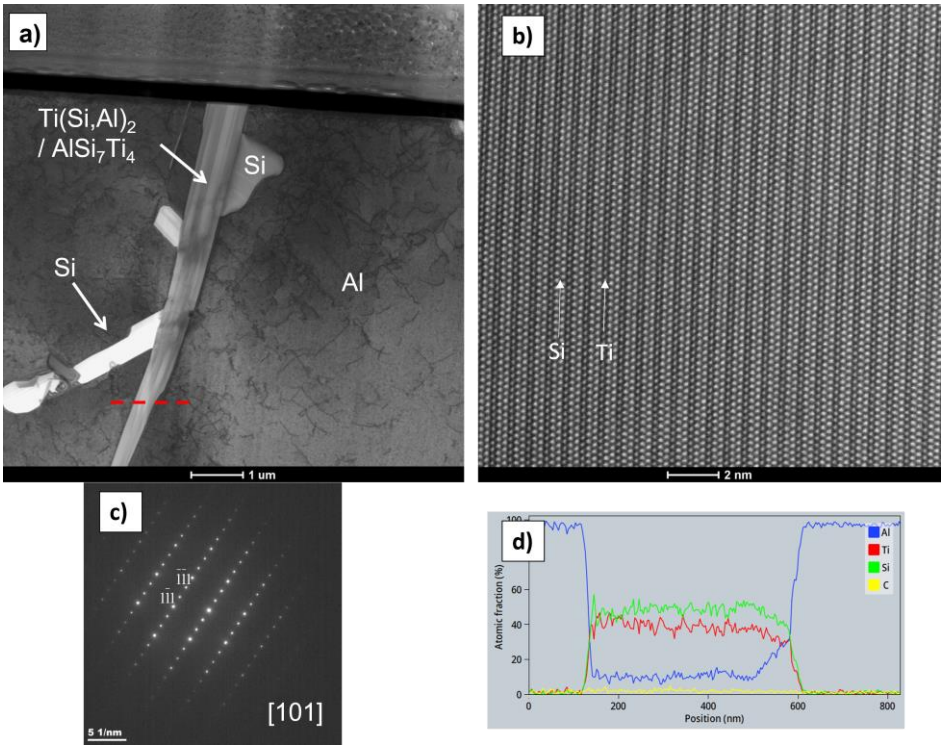

Figure 5.12 (a) TEM of the Al-7Si sample showing $Ti(Si,Al)_2$, Al matrix, and Si (b) HRTEM showing the atomic planes of Si and Ti in the intermetallic, (c) A diffraction pattern from the $Ti(Si,Al)_2$ intermetallic, and (d) A chemical line scan from a) showing the amount of Al, Ti, Si, and C in the phase

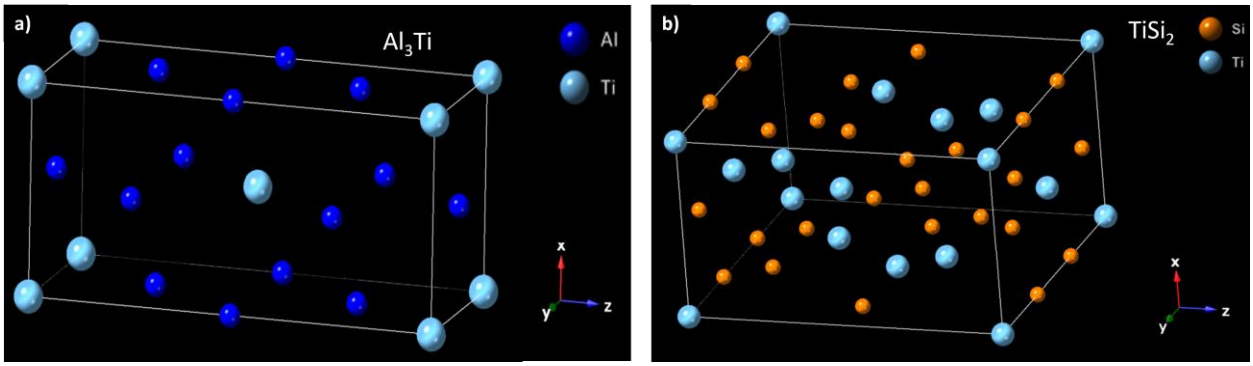

Figure 5.13 Crystal structure for (a) Al_3Ti and (b) $TiSi_2$

Looking through the TXM data we found a few phases similar to what was seen in Chapter 4, but only in the Al-1Si/TiC MMNC. A 3D visualization of orthogonal plates from the Al-1Si sample is shown in **Fig. 5.13**, although unlike the orthogonal plates found in the pure Al samples this one shows a crevice where the plates intersect as well as what appears to be residual step-growth along the plates. As discussed in Section 5.1, Al_3Ti has a certain amount of Si solubility, so it is possible that the presence of Si within the structure has some effect on its growth. Another familiar morphology can be found in the large blocks shown in **Fig. 5.15**. For visual clarity the TiC particles are not displayed in **Fig. 5.1c**. These large blocks are similar to those

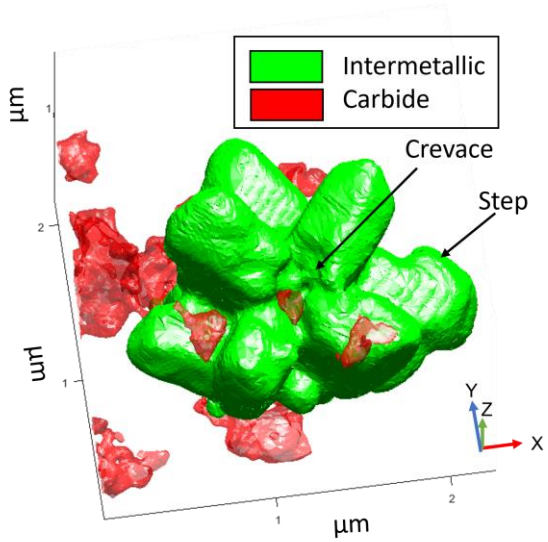

Figure 5.14 3D visualization of orthogonal plates of Al3Ti in the Al-1Si MMNC

shown in **Fig. 4.9** and are indicative of a region of the sample which cooled slowly. This section of the TXM data had two other features of interest, a residual flux phase and some porosity,

which are displayed in purple and dark blue respectively. The identity of the residual flux phase is likely $KAlF_4$, as that is a known byproduct of the salt-flux reaction, and the intensity values more closely match those of $KAlF_4$ and K_2AlF_6 (see Table 4.X) than any Si-rich binary or ternary (see **Table 5.3**).

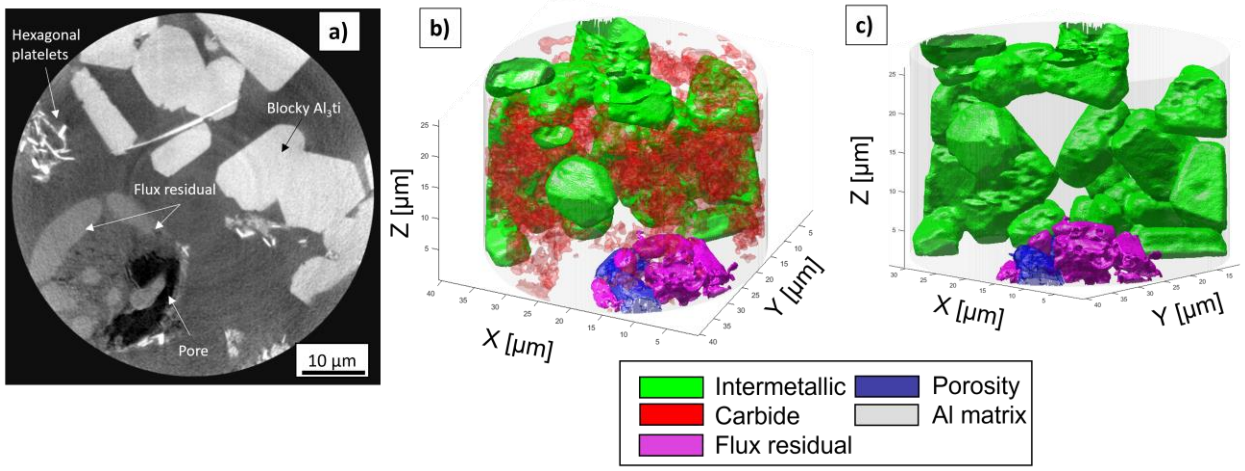

Figure 5.15 (a) Reconstructed slice of the Al-1Si MMNC, (b) 3D visualization of blocky Al3Ti showing the carbides (c) 3D visualization not showing the carbides

While a few of the intermetallic structures in the Al-1Si sample were similar to those made in pure Al, they were exceedingly rare and the majority of the intermetallics showed a branched or dendritic morphology, seen in **Fig. 5.16**. This morphology matches well with what was seen in SEM (**Fig. 5.11**) and TEM (**Fig. 5.12**), where in 2D the arms of the dendrite appear as H-shaped structures or hollow needles. Similarly, the intermetallics in the Al – 4Si and Al – 7 Si were all dendritic. Between the TXM, SEM and TEM data we can conclude that this dendritic structure is $Ti(Al,Si)_2$, which implies that any MMNCs made via salt-flux reaction synthesis in an Al-Si alloy will have far more $Ti(Al,Si)_2$ than Al_3Ti or other intermetallics. Important questions related to this conclusion are: 1. How does the formed intermetallic affect the mechanical properties of the MMNC, and is one better than the other, and 2. What is the formation mechanism of the $Ti(Al,Si)_2$, and why does it form so readily in the presence of Si, even as low as 1 wt%?

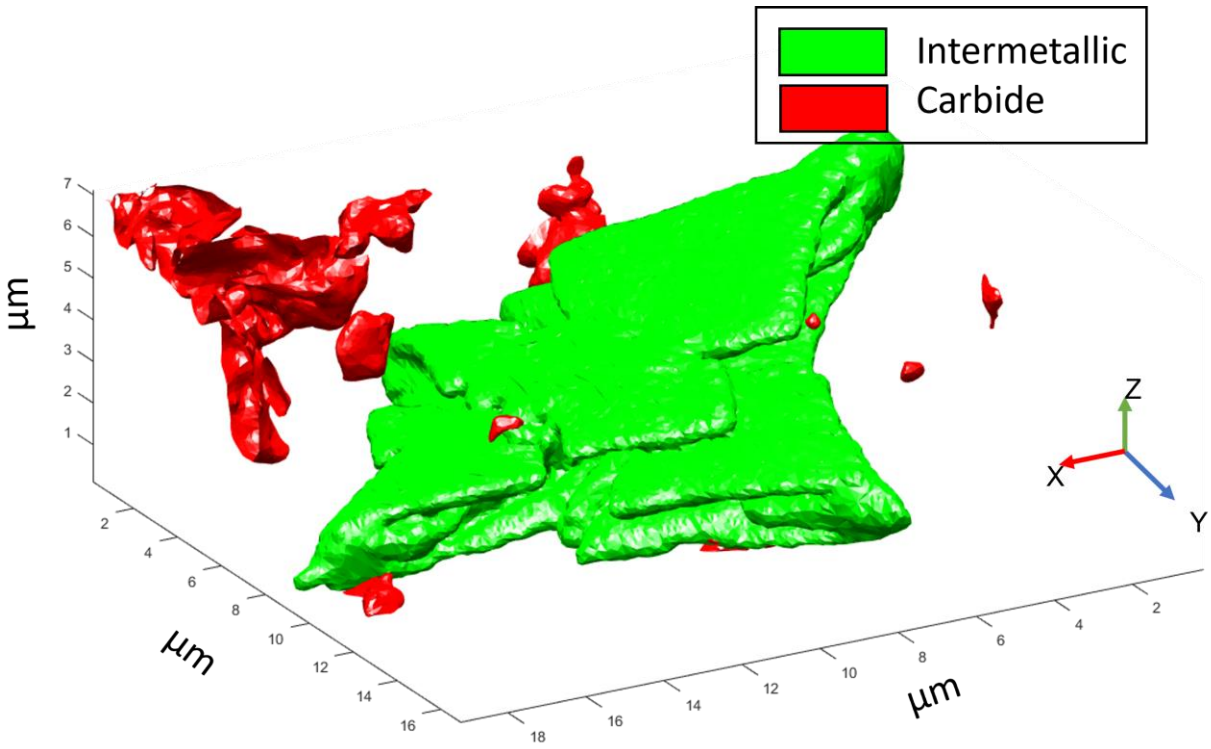

Figure 5.16 3D visualization of dendritic $Ti(Al,Si)_2$ intermetallic

As a start to answering the first question, the results from the nanomechanical testing are discussed in Section 5.3.3, although they are far from being conclusive on this matter. For the second question we can turn to literature. Thermodynamically we found that $Ti(Al,Si)_2$ can be formed through two different pathways, a quasi-peritectic reaction at 595 °C (**Eqn. 5.1**) or a eutectic reaction at 575 °C (**Eqn. 5.2**) [269, 293]

$$L + TiAl_3 \rightarrow \tau_2 + fcc(Al) \text{ at T} = 595\ ^\circ\text{C} \quad (5.1)$$

$$L \rightarrow \tau_2 + fcc(Al) + fcc(Si) \text{ at T} = 575\ ^\circ\text{C} \quad (5.2)$$

Where τ_2 is used as a general term for $Ti(Al,Si)_2$, $AlSi_7Ti_4$, and $AlSi_3Ti_2$. This brings up the question of if the phase is formed indirectly through a reaction with Al_3Ti (**Eqn. 5.1**) or directly from the liquid during the *in situ* reaction (**Eqn. 5.2**), and how we could best control its formation, similar to our discussion for forming TiC. Ma *et al*. found evidence in their work for indirect formation via Si diffusing into the Al3Ti intermetallic and substituting for Al (see **Fig.**

5.3) [270, 272, 273], and proposed the following pathways, which are reminiscent of **Eqn. 4.1** but with the addition of forming Al_3Ti.

$$3K_2TiF_6 + 13Al \rightarrow 3Al_3Ti + 3KAlF_4 + K_3AlF_6 \quad (5.3)$$

$$Al_3Ti + 3xSi \rightarrow (Al_{1-x}Si_x)_3Ti \quad (5.4)$$

Another possibility is the effect of cooling rate on the formed phases; we already discussed how cooling rate affects the morphology of Al_3Ti (see Section 4.3.1), but the rate of solidification likely plays a big role in forming these ternary intermetallics as well. Saheb *et al.* found that quenching an Al – 4 Ti – 17 Si alloy formed $AlSi_2Ti$, which they claim has a different structure than both Al_3Ti and $TiSi_2$, compounds and led to increased microhardness [294].

More work needs to be done to identify the pathway of formation of the Si-rich ternary phases, especially if they are formed through Si-enrichment (i.e. solute segregation), a kinetic effect during nucleation or growth, or if there is a solid state transformation occurring, and how their presence in the composite either benefits or is detrimental to its performance.

5.3.3 Mechanical properties

The results from the nanomechanical testing are shown in the histograms of **Figs. 5.17.** While stiffness was measured directly by the equipment, the Youngs modulus (E) had to be calculated from the reduced modulus (E_r) measured by the machine. The Youngs modulus was calculated following the method outlined in Oliver and Pharr's 1992 paper [295] using Eqn. 5.1.

$$\frac{1}{E_R} = \frac{1-\nu^2}{E} + \frac{1-\nu_i^2}{E_i} \quad (5.1)$$

Where E, E_i, ν, and ν_i are the modulus of the test material, modulus of the indenter, Poisson's ratio of the test material, and Poisson's ratio of the indenter, respectively. Specifications from the equipment list $E_i = 1140$ GPa and $\nu_i = 0.07$. For simplicity we chose to use the Poisson's ratio of pure Al ($\nu = 0.33$) for all calculations.

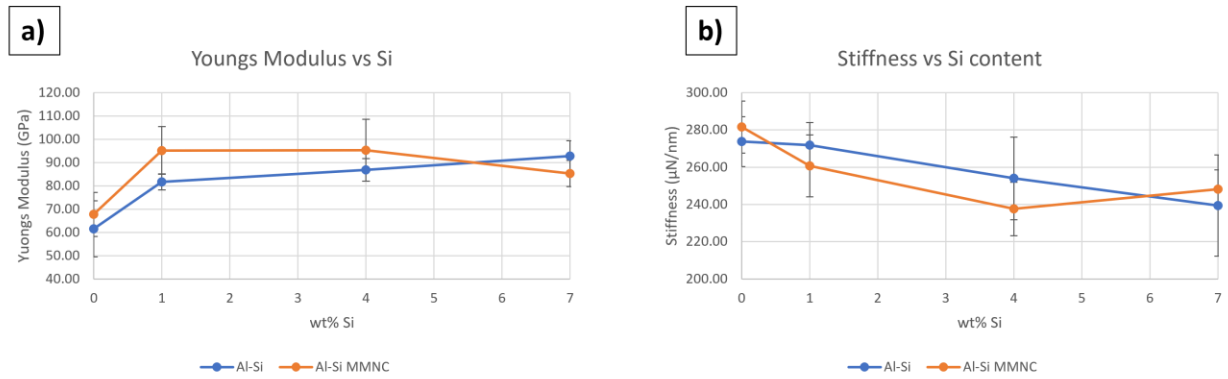

Figure 5.17 Results of the nanomechanical testing (a) Youngs modulus vs wt% Si with for Al-Si alloys (blue) and Al-Si MMNCs (orange) (b) Stiffness vs Si content for Al-Si alloys (blue) and Al-Si MMNCs (orange)

The samples showed a consistent increase in Youngs modulus upon the addition of Si compared with pure Al, and the MMNC samples showed further increase in modulus than the binary Al-Si alloys. While the modulus of the binary alloy continues to increase with additional Si content, the modulus of the MMNCs levels off between 1 and 4 wt% Si, then decreases for the Al-7Si MMNC even below that of Al-7Si binary alloy. This decrease in modulus could be indicative of the effect of the reinforcement changing primarily from TiC in 0-4 wt% Si to Ti_3SiC_2 in the 4 and 7 wt% Si MMNCs, although further tests need to be conducted to get a broader range of Si content (e.g. 5-10 wt% Si) to thoroughly investigate this hypothesis. The data plotted in **Fig. 5.17** is numerically listed in **Tables 5.2** and **5.3**.

Another takeaway from these experiments is that for some amount of Si stiffness of the MMNCs decreases compared with the binary alloys. The 0 and 7 wt% Si MMNCs have higher stiffnesses than the binary alloys, but stiffness of the 1 and 4 wt% MMNCs are lower than that of the binary alloy. This decrease could be resulting from the change in intermetallic formed via

SFRS, be it Al_3Ti or $(Al, Si)_2Ti$, as we saw that the intermetallic is more susceptible to changes from lower Si content than the carbide. However, $(Al, Si)_2Ti$ is reportedly stiffer than Al_3Ti, ($E_{TiSi_2} = 259\ GPa$ [296], $E_{Al_3Ti} = 216\ GPa$ [297]), and Si is far stiffer than Al ($E_{Si} = 165$, $E_{Al} = 68\ MPa$) so there is clearly a more complex reason behind this softening effect which we will not go into in this work. Increasing the amount of Al-Si alloys (e.g. 3, 5, 8, 10 wt%) would greatly inform if the changes in mechanical properties are truly caused by the Si changing the microstructure formed via SFRS.

Table 5.3 Youngs modulus calculated from nanomechanical testing

Youngs Modulus (Gpa)					
Material	**Avg**	**SD**	**% from Pure Al**	**% from $Al_{(1-x)}Si_{(x)}$**	**No.**
Al	61.5	12.0	n/a	n/a	12
Al TiC	67.7	9.4	10%	10%	14
Al1Si	81.7	3.5	33%	n/a	15
Al1Si TiC	95.2	10.2	55%	17%	12
Al4Si	86.8	4.9	41%	n/a	14
Al4Si TiC	95.3	13.3	55%	10%	15
Al7Si	92.7	6.6	51%	n/a	13
Al7Si TiC	85.3	5.6	39%	-8%	15

Table 5.4 Stiffness calcualted from nanomechanical testing

Stiffness (μN/nm)					
Material	**Avg**	**SD**	**% from Pure Al**	**% from Al(1-x)Si(x)**	**No.**
Al	273.7	13.4			12
Al TiC	281.6	14.0	3%	3%	14
Al1Si	271.8	12.1	-1%		15
Al1Si TiC	260.7	16.6	-5%	-4%	12
Al4Si	254.0	22.2	-7%		14
Al4Si TiC	237.6	14.4	-13%	-6%	15
Al7Si	239.4	27.2	-13%		13
Al7Si TiC	248.3	10.2	-9%	4%	15

5.4 Conclusions

In this chapter we investigated the effect of adding silicon (0, 1, 4, and 7 wt%) to the aluminum matrix for prior to the generation of MMNCs via the salt-flux reaction synthesis. We analyzed the microstructure and the formed phases using 2D (TEM, SEM, XRD) and 3D (TXM) techniques. We found that spherical TiC particles were found in all the samples, but noticed a transition point when 4 wt% or more Si was added to the matrix that Ti_3SiC_2 hexagonal platelets were formed as well as spherical TiC particles. We discussed the potential of how the hexagonal plates are formed in parallel with the TiC (i.e. both nucleating from the reaction) or how the TiC may evolve into the ternary carbide by Si substituting into the C-vacancies within the sub-stoichiometric TiC.

We also looked into the effect of Si on the intermetallics which formed. Previously seen morphologies (e.g. orthogonal plates and blocks) were found in the 1 wt% Si sample, likely because solid solubility of Si in Al_3Ti, where Si substitutes for Al, allows for the retention of this phase. We also found a majority of the intermetallics do be dendritic structures and identified this phase as $Ti(Al,Si)_2$, an intermetallic sharing the same structure of $TiSi_2$. Theory and possible routes of formation for this new intermetallic phase were also discussed.

Finally, we performed nanomechanical testing and found that increasing Si content increases Youngs modulus while decreases stiffness for both the MMNCs and the binary alloy samples, but the MMNCs tended to have higher Youngs modulus than their similar Si-containing binary.

CHAPTER 6
Summary, Preliminary Particle-Solidification Front Experiments, Suggestions for Future Work

6.1 Dissertation summary

Metal matrix nanocomposites (MMNCs) continue to be a promising route for improving lightweight materials via enhanced mechanical properties at ambient and elevated temperatures. MMNCs are typically made via *ex situ* processing, where pre-manufactured reinforcing particles are incorporated into the Al matrix. These routes of MMNC production have a few main issues including the cost of the reinforcing nanopowders, reinforcement contamination, and undesirable particle-matrix interface reactions, which make particle incorporation and large-scale processing difficult. In contrast, *in situ* MMNC processing methods generate particles directly in the melt via a reaction between precursors and have shown improved particle-matrix interface stability and easier particle incorporation with the matrix. However, there is much work to be done to reliably control key particle characteristics, such as particle size, dispersion, and volume fraction, when creating *in situ* MMNCs. The work in this dissertation sought to investigate the processing-microstructure-properties relationships and formation mechanisms for multiple *in situ* Al-based MMNCs to better inform their use and production in the future.

In Chapter 2 we reviewed relevant literature for MMNC production, with a focus on *in situ* approaches of production. We compared the advantages and disadvantages of *ex situ* and *in situ* processing methods and gave more in depth information for the *in situ* methods studied in

the following chapters. This chapter also reviewed the strengthening mechanisms of MMNCs and the key particle characteristics whose control is needed for optimal MMNC performance. This review provided a framework for the work studied in Chapters 3, 4, and 5 of this dissertation.

In Chapter 3 we investigated the processing-properties relationships of MMNCs made via metal-based polymer pyrolysis (MBPP). This investigation started with the analysis of commercially available polymer precursors and how they thermally degrade into ceramics. Next, we used these precursors to generate Al-MMNCs and tested processing controls such as the precursor used, volume fraction of polymer added, and how it was incorporated into the Al matrix. We demonstrated that MBPP is a possible *in situ* approach for forming Al-MMNCs and also briefly investigated using other metal matrices (Cu, Mg, Sn, Zn).

Chapter 4 was a detailed investigation into MMNCs made via salt-flux reaction synthesis, using 2D and 3D microstructural analysis. The data and analysis clarify the formation mechanisms of TiC during the salt-flux reaction and better inform the size distribution of the particles. There was also significant discussion on how the intermetallic Al_3Ti is affected by processing parameters, such as cooling rate and Ti-concentration, as well as investigation into a novel Al_3Ti morphology of orthogonal plates. We found that the orthogonal plates of Al_3Ti nucleate on TiC particles, and that smaller particles affect the growth and cause the arms of the intermetallic to split.

Chapter 5 was continued investigation into the salt-flux reaction synthesis using 2D and 3D microstructural analysis. The experiments conducted in this chapter focused on the effects of adding varying amounts of Si to the Al matrix prior to conducting the *in situ* reaction. We found that at 4 or more weight percent Si hexagonal plates of Ti_3SiC_2 form along with spherical TiC

particles. We also found that any addition of Si led to the formation of dendritic $(Al, Si)_2Ti$, an intermetallic following the structure of $TiSi_2$, formed while only a minimal amount of Al_3Ti formed. We performed nanomechanical tests on these MMC samples and compared the results with the equivalent Al-Si binary alloys.

The work covered in this dissertation can have a significant impact on the use and production of metal matrix composites. The work in Chapter 3 opens the possibility of using Metal-Based Polymer Pyrolysis to create Al-based MMCs, a feat which had only been done in Cu and Mg previously. Chapters 4 and 5 add a significant amount of understanding and knowledge to what is known about salt-flux reaction synthesis, and its sensitivity to processing parameters. Perhaps the most important takeaway from these chapters is that the TiC particles form prior to the Al_3Ti intermetallics, and that the Al_3Ti do not play any role in the TiC formation. Knowing that the carbides form first, and form directly, is the key takeaway: clarity in the TiC formation mechanism will allow future scientists to have more successful experiments that focus on TiC formation, dispersion, and size, and on limiting the formation of Al_3Ti. Since the intermetallic is now known as a superfluous phase it can be removed by careful process control and parameter testing, thus leading to a more efficient process and a better final material.

6.2 Suggestions for future work and research directions

The following sections cover suggestions for future work and directions based on the results presented in the previous chapters. We will also present some preliminary work on watching particle and solidification front interactions *in situ* using synchrotron-based X-ray radiography and nanotomography that we were unable to complete over the course of the work presented here.

6.2.1 Improved polymers for metal-based polymer pyrolysis

As shown in Chapter 3 metal-based polymer pyrolysis remains a unique and generally unexplored manner to form *in situ* metal matrix composites. Although our results show the method is possible for Al matrices, the reported results relied on using metal powder which would be unreasonable for any amount of medium or large-scale production. We showed some results for adding polymers to a bulk Al melt, but the process may be improved by cross-linking the polymers into a resin and sputter-coating a layer onto the resin powder for improved wettability with the melt. Furthermore, adding some amount of melt-processing such as mechanical stirring and degassing would improve the particle dispersion and reduce the porosity caused by the pyrolysis. A very long term solution for MBPP could be the collaboration between a melt-processing lab and a polymer-derived ceramics lab to generate a new, specialized precursor designed specifically for MBPP.

6.2.2 The effects of other processing parameters on salt-flux reaction synthesis

As mentioned in Chapter 2 the final microstructure and properties of an *in situ* metal matrix composite are highly dependent on the processing parameters involved in its creation, and in that regard salt-flux reaction synthesis is no different than other *in situ* techniques. While we discussed some effects of cooling rate in Chapter 4 and the effects of Si addition in Chapter 5, there are many more parameters which could be studied.

The effects of melt processing parameters such as reaction temperature, holding time, adding mechanical or ultrasonic mixing, and cooling rate could all have large impacts in the formation of MMNCs. Holding time as well as the effect of remelting and diluting a master alloy are key parameters as it has been shown that TiC is unstable in liquid Al below 850 ºC and is more likely to decompose in the presence of Si, forming $TiAl_xSi_y$ and Al_4C_3 caused by the out-

diffusion of C and incursion of Si and Al, along with the possibility of Si diffusing into the Al3Ti intermetallics [270, 272, 273, 288, 289, 298-302].

On top of these parameters one could focus on the effects of the materials used for the salt-flux experiments, including a study on different metal-bearing fluxes or a review of how the carbon source affects the formed carbides. Furthermore, a wide range of elements are added to Al in commercial alloys, the most common being Cu, Mg, and Zn, and their effect on the salt-flux reaction should be looked into for a better understanding of how applicable the technique can be to industrial-scaled processing. Similarly, a better understanding of the effects of Si during the production of TiC, Ti_3SiC_2, Al_3Ti, and $(Si,Al)_2Ti$ must be conducted.

6.2.3 High temperature mechanical testing

A large reason for using MMNCs is their improved mechanical properties at elevated temperatures, but unfortunately the work in this dissertation was only able to test the samples at ambient temperatures. To facilitate elevated temperature tests, one could use the high temperature tensile rig set up in the S.M. Wu Manufacturing Research Center or use the high temperature stage for the Hysitron TI-950 triboindenter at the Michigan Center for Materials Characterization.

6.2.4 Particle/melt interactions during solidification

While there is much work done on the mechanisms by which MMNCs are created, particle dispersion is a key problem which all MMNC systems must overcome to achieve their desired properties. For improved dispersion an improved understanding of the particle-solidification front interactions must be attained. While many models have been proposed over the years to try and predict particle-solidification front interactions [280-282, 303-306] there

remains a large gap between the models and the experimental observations, particularly due to the complexity of watching nano-sized particles *in situ*.

In general, when the solidification front approaches a second-phase solid particle the particle can either be engulfed, also termed as captured, trapped by growing dendrite arms, or pushed, also known as rejected [303, 307], see **Fig. 6.1**. The most ideal method of incorporation

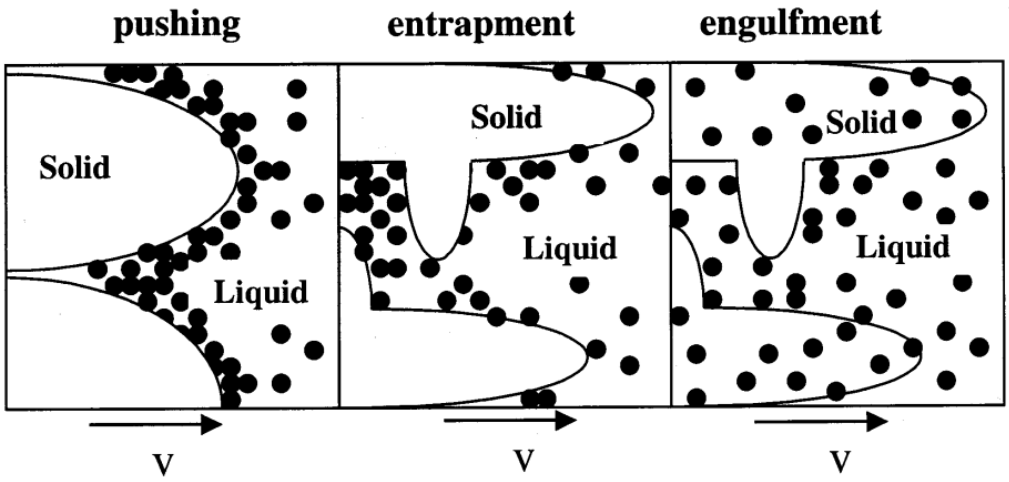

Figure 6.1 A schematic showing the possible interactions between a dendritic solidification front and dispersed solid particles, from [307]

as it leads to distribution of particles within grains across the material, while particles which are trapped or pushed tend to agglomerate in grain boundaries. While more complex models continue to be developed, they often relay on a variety of simplifying assumptions, including spherical particles which have no size variation, chemically inert particles that do not as nucleation sites, limited particle motion in 1D (i.e. toward/away from the front, so side to side or Brownian motion is ignored), and a dispersion of particles to ensure no solid-solid interactions. More recent work models have incorporated additional parameters to improve their accuracy, including the effects of Brownian motion [308], the shape of the nanoparticles [309], solute diffusion between the interface and particle [310], other solute concentration effects including melt viscosity [281, 311, 312], varied interface shape [304, 313, 314], and particle-melt

interfacial surface energies [282, 303]. In general, the models calculate a critical velocity that the solidification front must be moving to facilitate the capture of solid particles, which tends to increase with decreasing particle size.

The problem of particle-front interactions becomes even more complex when considering matrices that consist of multiple elements, e.g. alloys. On one hand, constitutional undercooling can affect the local thermal gradient near the solidification front, and thus change the growth velocity, but on the other hand, recalescence provides local heating during solidification due to the latent heat being liberated from solidification. It has been shown that in general the presence of solute reduces the critical velocity compared with pure liquid, leading to easier engulfment, although if the particle is highly reactive with the solute then the critical velocity increases with the amount of solute in the melt [280, 311]. If the particle is reactive with the solute it can act as a solute sink, incorporating large amounts of solute into the particle. In addition to the considerations of particle engulfment by the advancing solidification front, nanoparticles may modify the matrix solidification behavior, such acting as grain nucleation sites [24, 249, 315].

A large amount of work is required to better understand the interactions between nanoparticles and the solidification front. In the following section we will go over some preliminary results from NSLS-II focused on watching the interactions of TiC nanoparticles and the solidification front of an Al-2Cu matrix in real time using synchrotron-based X-ray nanoradiography.

6.2.5 Preliminary results of watching real-time particle/solidification front

It is clear that particle dispersion and particle/solidification front interactions remain a key area of research for improved MMNC properties and production abilities. We conducted preliminary solidification experiments using synchrotron-based X-ray radiography (XRR) to watch the interactions between the solidification front and particles in real time, and used TXM to compare the 3D microstructure and particle dispersion before and after the remelting. Samples were made by alloying previously made Al/TiC MMNCs with either Cu or Zn to give contrast between the solidification front and the liquid regions.

Table 6.1 Sample information of Al/TiC MMNCs used for solidification experiments, from [272]

Alloy	SHS Sample Name	TiC diameter [nm]	TiC Vol%
Al	L3	392	0.74
Al-2Cu	S4	638	2
Al-2Cu	S5	767	2.08
Al	S6	388	2.05
Al-15Zn	S6	388	2.05
Al	S7	578	1.79
Al-15Zn	S7	578	1.79
Al-25Zn	S8	908	2.09

The original MMNCs were made using self-propagating high-temperature synthesis (SHS). To create the pellets for SHS experiments, powders of Al (~30 µm, 99.5% purity), Ti (~20 µm or ~44 µm, 99.7% purity), C (100nm or 9 µm, 99% purity), and CuO (<10 µm, 98% purity) were mixed in composition ratios of 1.5 mol Al, 1 mol Ti, 1 mol C, and 0.1 mol CuO. The powder mixtures were pressed into pellets then added to 500 g of molten Al (99.99% purity) that was held at 850 °C for the SHS process to occur and precipitate TiC particles. More information on the SHS process and the samples can be found at [277]. Data regarding the original MMNCs and what we alloyed them with can be found in **Table 6.1**.

After alloying the SHS MMNCs with Cu or Zn we prepared the XRR and TXM samples by first cutting 1 mm rods from the bulk samples as described in Section 4.2.2, then the samples were thinned to a <100 µm point using the approach explained in Section 4.2.3, and finally

milled into their final shapes using the PFIB as described in Section 4.2.2. Unlike previous work these samples were FIBed into a variety of shapes for improved structural integrity of the specimen during the melt experiments. The samples were either rectangular micropillars (40 μm wide by 20 μm thick), cylindrical micropillars (40 μm diameter), or pillars with thinned out "windows" where the thinned section was roughly 40 μm wide by 20 μm thick.

XRR and TXM experiments were conducted at the beamline 18-ID at the National Synchrotron Light Source II (NSLS-II) in Brookhaven National Laboratory (Upton, NY). Samples were placed into an boron nitride holder attached to a kinematic mount then coated with boron nitride paste to reduce oxidation when heating up and for improved structural stability at high temperatures. Once the samples were centered and aligned, we introduced them to the furnace and began to heat the samples very quickly (20-50 °C/min) until they were near the melting temperature, then slowed the heating rate to 2-5 °C/min until we saw evidence of melting (i.e. particle movement, movement of liquidus line, disappearance of internal structure). Upon melting we cooled the samples at from 1-10 °C/min depending on the sample. A few samples were melted and solidified a number of times to determine if the melt-freeze cycling led to significant microstructural changes. The furnace used was a single-zone furnace so we had the ability to control the heating or cooling rates but could not adjust the thermal gradient within the furnace. Images were collected using an exposure time of 50 ms and an operating energy of 9-9.5 keV. A TXM scan was taken of each sample prior to heating it, then images were recorded as the sample approached its melting point and through solidification, and finally a TXM scan was taken after the sample had resolidified.

We found that watching the liquidus and solidification front was more challenging than expected due to the presence and interference of the particles. Furthermore, the samples were

able to withstand temperatures far exceeding their melt temperature prior to collapsing, one sample was brought to nearly 200 °C above its melt temperature prior to collapsing. Furthermore, there was far less particle movement than expected, only a fraction of particles would move despite many being present, so we hypothesized that the TiC particles along with the Al oxide skin were forming an internal structure that supported the MMNC to extremely high temperature. Analysis of data from these experiments is ongoing, and will serve as a benchmark for future solidification experiments at NSLS-II.

Since running these experiments, we have found multiple methods to improve future particle/solidification front experiments. First, there are some ways we could change future samples to ensure the particles have minimal contact with one another and prevent them forming an internal structure holding them in place. This change could be done by producing samples at a lower particle loading, quenching the samples faster to create smaller grains and thus more dispersed particles (assuming they are in the grain boundaries), or by mechanically altering the as-made samples to break up the particle agglomerates. Following the last idea, rolling the material would have the dual benefits of mechanically breaking up the agglomerates of particles and creating columnar grains that could act as particle-free regions for the melt/solidification to occur in. Second, there has been a significant upgrade in the hardware at the 18-ID beamline. Our work was conducted using a single zone furnace that had a set temperature gradient of 6 °C/cm. While this equipment worked well for general heating, there was no way to adjust the temperature gradient and experiments were done by controlling the heating or cooling rate alone. Since these experiments there has been a new two-zone furnace installed into the beamline. It follows the same geometry as the previous furnace and allows for greatly enhanced temperature controls. Each zone operates independently, with 0.1 °C precision, and it can operate in an

isothermal state or reach a maximum gradient of 20 °C/cm. Using this furnace will allow for improved melting and solidification experiments since now the thermal gradient can be controlled, the gradient can be much larger than the previous model, and the temperature settings will be more accurate than the previous model. With this furnace micropillar samples can be held just above melting temperature in order to conduct the experiment, and the large thermal gradient can be used to keep their base as solid material, thus reducing the possibility of sample collapse and greatly increasing the viability of these types of experiments.

APPENDIX

APPENDIX A – Helpful MATLAB Functions

This section is meant to highlight MATLAB functions that can be helpful for segmenting and working with data. It is by no means a complete list of what is available, and the order is arbitrary. The function descriptions are provided by the Mathworks website (Mathworks.com) and readers are prompted to look into their documentation for more information.

- Bwconncomp(), find and count connected components in a binary image
- Edge(), finds edges in 2-D grayscale images
- Entropyfilt(), local entropy of grayscale image
- Medfilt2(), 2-D median filtering
- Medfilt3(), 3-D median filtering
- Volshow(), display a volume
- Imshow(), display an image
- Labeloverlay(), Overlay label matrix regions on 2-D image
- Smoothpatch(), smooth a triangulated mesh or patch [222]
- Bwareaopen(), Remove small objects from binary image
- Imdilate(), dilate an image
- Imerode(), erode an image
- Strel(), create a morphological structuring element
- Imbinarize(), Binarize 2-D grayscale image or 3-D volume by thresholding
- Isosurface(), Extract isosurface data from volume data
- Patch(), Plot one or more filled polygonal regions
- Reducepatch(), Reduce number of patch faces
- Imquantize(), Quantize image using specified quantization levels and output values
- Regionprops3(), Measure properties of 3-D volumetric image regions
- Imresize(), resize an image
- Imresize3(), resize 3-D volumetric intensity image
- Export_fig(), multipurpose saving feature improved over MATLAB's standard saving for figures [316]

BIBLIOGRAPHY

[1] J. Motavalli, For lightweight cars, a materials race, The New York Times, 2012.
[2] R. Geng, F. Qiu, Q.-C. Jiang, Reinforcement in al matrix composites: A review of strengthening behavior of nano-sized particles, Advanced Engineering Materials 20(9) (2018).
[3] A.V. Muley, S. Aravindan, I.P. Singh, Nano and hybrid aluminum based metal matrix composites: An overview, Manufacturing Review 2 (2015).
[4] S.L. Pramod, S.R. Bakshi, B.S. Murty, Aluminum-based cast in situ composites: A review, Journal of Materials Engineering and Performance 24(6) (2015) 2185-2207.
[5] A. Mortensen, J. Llorca, Metal matrix composites, Annual Review of Materials Research 40 (2010) 243-270.
[6] Ø. Ryen, O. Nijs, E. Sjolander, B. Holmedal, H.-E. Ekstrom, E. Nes, Strengthening mechanisms in solid solution aluminum alloys, Metall. Mater. Trans. A 37A (2006) 1999-2006.
[7] C.B. Fuller, D.N. Seidman, D.C. Dunand, Mechanical properties of al(sc,zr) alloys at ambient and elevated temperatures, Acta Mater 51(16) (2003) 4803-4814.
[8] J.K. Kim, H.K. Kim, J.W. Park, W.J. Kim, Large enhancement in mechanical properties of the 6061 al alloys after a single pressing by ecap, Scripta Materialia 53(10) (2005) 1207-1211.
[9] D. Weiss, Improved high-temperature aluminum alloys containing cerium, J. Mater. Eng. Perform. 28 (2019) 1903-1908.
[10] I. Anza, Synthesis of aluminum-titanium carbide nanocomposites by the rotating impeller gas-liquid in-situ method, Material Science and Engineering, Worcester Polytechnic Institute, 2016.
[11] Z. Guo, W. Sha, Quantification of precipitation hardening and evolution of precipitates, Mater. Trans. 43(6) (2002) 1273-1282.
[12] L. Ceschini, A. Dahle, M. Gupta, A.E.W. Jarfors, S. Jayalakshmi, A. Morri, F. Rotundo, S. Toschi, R.A. Singh, Metal matrix nanocomposites: An overview, Aluminum and magnesium metal matrix nanocomposites2017, pp. 1-17.
[13] L. Ceschini, A. Dahle, M. Gupta, A.E.W. Jarfors, S. Jayalakshmi, A. Morri, F. Rotundo, S. Toschi, R.A. Singh, Ex situ production routes for metal matrix nanocomposites, Aluminum and magnesium metal matrix nanocomposites2017, pp. 19-40.
[14] Y. Yang, J. Lan, X. Li, Study on bulk aluminum matrix nano-composite fabricated by ultrasonic dispersion of nano-sized sic particles in molten aluminum alloy, Materials Science and Engineering: A 380(1-2) (2004) 378-383.
[15] T.W. Clyne, An introduction to metal matrix composites, 1 ed., Cambridge University Press 1993.
[16] C. Borgonovo, D. Apelian, Aluminum nanocomposites via gas assisted processing, Materials Science Forum 690 (2011) 187-191.

[17] C. Borgonovo, Synthesis of aluminum-aluminum nitride nanocomposites by gas-liquid reactions, 2013.
[18] C. Borgonovo, M.M. Makhlouf, Synthesis of aluminum–aluminum nitride nanocomposites by a gas–liquid reaction ii. Microstructure and mechanical properties, Metallurgical and Materials Transactions A 47(4) (2016) 1818-1827.
[19] C. Borgonovo, M.M. Makhlouf, Synthesis of aluminum-aluminum nitride nanocomposites by gas-liquid reactions i. Thermodynamic and kinetic considerations, Metallurgical and Materials Transactions A 47(10) (2016) 5125-5135.
[20] I. Anza, M.M. Makhlouf, Synthesis of aluminum-titanium carbide micro and nanocomposites by the rotating impeller in-situ gas–liquid reaction method, Metallurgical and Materials Transactions B 49(1) (2017) 466-480.
[21] I.A. Ibrahim, F.A. Mohamed, E.J. Lavernia, Particulate reinforced metal matrix composites - a review, Journal of Materials Science 26 (1991) 1137-1156.
[22] R. Casati, M. Vedani, Metal matrix composites reinforced by nano-particles—a review, Metals 4(1) (2014) 65-83.
[23] D.K. Das, P.C. Mishra, S. Singh, S. Pattanaik, Fabrication and heat treatment of ceramic-reinforced aluminium matrix composites - a review, International Journal of Mechanical and Materials Engineering 9 (2014) 1-15.
[24] Z.Y. Xu, C.J. Li, K.R. Li, J.H. Yi, J.J. Tang, Q.X. Zhang, X.Q. Liu, R. Bao, X. Li, Carbon nanotube-reinforced aluminum matrix composites enhanced by grain refinement and in situ precipitation, Journal of Materials Science 54(11) (2019) 8655-8664.
[25] J. Hashim, L. Looney, M.S.J. Hashmi, The wettability of sic particles by molten aluminium alloy, Journal of Materials Processing Technology 119 (2001) 324-328.
[26] F.L. Matthews, R.D. Rawlings, Composite materials: Engineering and science, Woodhead Publishing Limited, Cambridge, England, 1999.
[27] V.I. Kostikov, V.S. Kilin, Metal matrix composites, 2011.
[28] L. Ceschini, M. Gupta, S. Jayalakshmi, F. Rotundo, A. Dahle, A.E.W. Jarfors, A. Morri, S. Toschi, R.A. Singh, Aluminum and magnesium metal matrix nanocomposites, Springer Nature2017.
[29] D. Zhou, F. Qiu, H. Wang, Q. Jiang, Manufacture of nano-sized particle-reinforced metal matrix composites: A review, Acta Metallurgica Sinica (English Letters) 27(5) (2014) 798-805.
[30] S.Y. Oh, J.A. Cornie, K.C. Russell, Wetting of ceramic particulates with liquid aluminum alloys: Part ii. Study of wettability, Metall. Mater. Trans. A 20(3) (1989) 533.
[31] F. Delannay, L. Froyen, A. Deruyttere, The wetting of solids by molten metals and its relation to the preparation of metal-matrix composites, J. Mater. Sci. 22 (1987) 1-16.
[32] R. Casati, M. Amadio, C.A. Biffi, D. Dellasega, A. Tuissi, M. Vedani, Al/al₂o₃ nanocomposite produced by ecap, Materials Science Forum 762 (2013) 457-464.
[33] A. Manoylov, V. Bojarevics, K. Pericelous, Modeling the break-up of nano-particle clusters in aluminum- and magnesium-based metal matrix nano-composites, Metall. Mater. Trans. A 46A (2015) 2893-2907.
[34] X.-H. Chen, H. Yan, Solid-liquid interface dynamics during solidification of al 7075-al2o3np based metal matrix composites, Materials and Design 94 (2016) 148-158.
[35] A.D. Hamedan, M. Shahmiri, A new model for the solidification of metal matrix nanocomposites: Wet cluster engulfment of nanoparticles by the solidification front, J. Compos. Mater. 51(20) (2017) 2913-2932.

[36] M. Karbalaei Akbari, H.R. Baharvandi, K. Shirvanimoghaddam, Tensile and fracture behavior of nano/micro tib2 particle reinforced casting a356 aluminum alloy composites, Materials & Design (1980-2015) 66 (2015) 150-161.
[37] R. Casati, A. Fabrizi, G. Timelli, A. Tuissi, M. Vedani, Microstructural and mechanical properties of al-based composites reinforced with in-situ and ex-situ al 2 o 3 nanoparticles, Advanced Engineering Materials 18(4) (2016) 550-558.
[38] M. Ciurdas, D. Alina Necsulescu, R. Marina Solea, Interface characterization of al/sicp compacts, IOP Conference Series: Materials Science and Engineering 1190(1) (2021).
[39] B.S.S. Daniel, V.S.R. Murthy, G.S. Murty, Metal-ceramic composites via in-situ methods, Journal of Materials Processing Technology 68 (1997) 132-155.
[40] S.C. Tjong, Novel nanoparticle-reinforced metal matrix composites with enhanced mechanical properties, Advanced Engineering Materials 9(8) (2007) 639-652.
[41] S.C. Tjong, Z.Y. Ma, Microstructural and mechanical characteristics of in situ metal matrix composites, Journal of Materials Science and Engineering A 29 (2000) 49-113.
[42] N. Chawla, K.K. Chawla, Metal matrix composites, Second ed., Springer Science2013.
[43] R.F. Shyu, C.T. Ho, In situ reacted titanium carbide-reinforced aluminum alloys composite, Journal of Materials Processing Technology 171(3) (2006) 411-416.
[44] R.F. Shyu, F.T. Weng, C.T. Ho, In situ reacted titanium nitride-reinforced aluminum alloy composite, Journal of Materials Processing Technology 122(2-3) (2002) 301-304.
[45] R. Casati, A. Fabrizi, G. Timelli, A. Tuissi, M. Vedani, Microstructural and mechanical properties of al-based composites reinforced with in-situ and ex-situ al ₂ o ₃ nanoparticles, Advanced Engineering Materials 18(4) (2016) 550-558.
[46] C. Borgonovo, M.M. Makhlouf, Synthesis of aluminum-aluminum nitride nanocomposites by gas-liquid reactions i. Thermodynamic and kinetic considerations, Metallurgical and Materials Transactions A: Physical Metallurgy and Materials Science 47(10) (2016) 5125-5135.
[47] B.S.S. Daniel, V.S.R. Murthy, G.S. Murty, Metal-ceramic composites via in-situ methods, Journal of Materials Processing Technology 68(2) (1997) 132-155.
[48] H. Nath, A.P. Amosov, Shs amidst other new processes for in-situ synthesis of al-matrix composites: A review, International Journal of Self-Propagating High-Temperature Synthesis 25(1) (2015) 50-58.
[49] C. Wang, H. Gao, Y. Dai, X. Ruan, J. Shen, J. Wang, B. Sun, In-situ technique for synthesizing fe-tin composites, Journal of Alloys and Compounds 490(1-2) (2010) 2009-2011.
[50] A.K. P, R. Raj, S.V. Kailas, A novel in-situ polymer derived nano ceramic mmc by friction stir processing, Materials & Design 85 (2015) 626-634.
[51] C. Borgonovo, D. Apelian, Manufacture of aluminum nanocomposites: a critical review, Materials Science Forum 678 (2011) 1-22.
[52] N. Gangil, A.N. Siddiquee, S. Maheshwari, Aluminium based in-situ composite fabrication through friction stir processing: A review, Journal of Alloys and Compounds 715 (2017) 91-104.
[53] R. Geng, F. Qiu, Q.C. Jiang, Reinforcement in al matrix composites: A review of strengthening behavior of nano-sized particles, Advanced Engineering Materials 20(9) (2018) 1-13.
[54] A. Kumar, P. Kumar, A review on the mechanical properties, tribological behavior and the microstructural characterization of aluminium metal matrix composites (ammcs). International Journal of Scientific & Engineering Research 6(6) (2015) 1234-1245.

[55] J. Menghani, N.R. Rathod, A consequence of reinforcements in aluminum-based metal matrix composites: A literature review, Metallurgical and Materials Engineering 25(3) (2019) 195-208.
[56] R.R. Mishra, A. Panda, A.K. Sahoo, R. Kumar, Research progress on nano-metal matrix composite (nmmc) fabrication method: A comprehensive review, Materials Today: Proceedings (2021).
[57] H. Nath, A.P. Amosov, Shs amidst other new processes for in-situ synthesis of al-matrix composites: A review, International Journal of Self-Propagating High-Temperature Synthesis 25(1) (2016) 50-58.
[58] R.J. Peterson, Literature review of polymer derived ceramics, Los Alamos National Laboratory, 2016, pp. 1-9.
[59] B.S.B. Reddy, K. Das, S. Das, A review on the synthesis of in situ aluminum based composites by thermal, mechanical and mechanical–thermal activation of chemical reactions, Journal of Materials Science 42(22) (2007) 9366-9378.
[60] A. Sharma, J. Paul, A review on the fabrication of in situ metal matrix composite during friction stir welding, Materials Science Forum 978 (2020) 191-201.
[61] S. Ullah Khan, D. Wanwu, Q. Ullah Khan, S. Khan, A. Alam, A. Ullah, H. Ullah, An analysis of in-situ synthesized al 6061 alloy metal matrix composites: Review, European Journal of Materials Science and Engineering 6(4) (2021) 220-233.
[62] M. Lenz Leite, G. Barroso, M. Parchovianský, D. Galusek, E. Ionescu, W. Krenkel, G. Motz, Synthesis and characterization of yttrium and ytterbium silicates from their oxides and an oligosilazane by the pdc route for coating applications to protect si3n4 in hot gas environments, Journal of the European Ceramic Society 37(16) (2017) 5177-5191.
[63] B. Gardelle, S. Duquesne, C. Vu, S. Bourbigot, Thermal degradation and fire performance of polysilazane-based coatings, Thermochimica Acta 519(1-2) (2011) 28-37.
[64] L. Jun, Q. Yulin, Z. Ping, X. Yinchang, C. Zhihai, Synthesis of sic ceramics from polysilazane by laser pyrolysis, Surface and Coatings Technology 321 (2017) 491-495.
[65] M. Günthner, K. Wang, R.K. Bordia, G. Motz, Conversion behaviour and resulting mechanical properties of polysilazane-based coatings, Journal of the European Ceramic Society 32(9) (2012) 1883-1892.
[66] M. Günthner, A. Schütz, U. Glatzel, K. Wang, R.K. Bordia, O. Greißl, W. Krenkel, G. Motz, High performance environmental barrier coatings, part i: Passive filler loaded sicn system for steel, Journal of the European Ceramic Society 31(15) (2011) 3003-3010.
[67] K. Wang, M. Günthner, G. Motz, R.K. Bordia, High performance environmental barrier coatings, part ii: Active filler loaded sioc system for superalloys, Journal of the European Ceramic Society 31(15) (2011) 3011-3020.
[68] Y. Wang, W. Fei, Y. Fan, L. Zhang, W. Zhang, L. An, Silicoaluminum carbonitride ceramic resist to oxidation/corrosion in water vapor, Journal of Materials Research 21(7) (2006) 1625-1628.
[69] P. Furtat, M. Lenz-Leite, E. Ionescu, R.a.F. Machado, G. Motz, Synthesis of fluorine-modified polysilazanes via si–h bond activation and their application as protective hydrophobic coatings, Journal of Materials Chemistry A 5(48) (2017) 25509.
[70] A. Horcher, K. Tangermann-Gerk, W. Krenkel, S. Schafföner, G. Motz, Advanced ceramic coatings on aluminum by laser treatment of filled organosilazane-based composites, Ceramics International (2022).

[71] M. Lenz Leite, P. Schlesinger, M. Sheridan, M. Zahedtalaban, D. Seitz, S. Schafföner, G. Motz, Hybrid copper(ii)acrylate/silazane thin coatings with hydrophobic and germicidal properties, Progress in Organic Coatings 166 (2022) 106791.
[72] J.W. Kemp, Processing of preceramic polymers for direct-ink writing, Mechanical Engineering, University of Tennessee, Knoxville, TN, 2021.
[73] L. Hagelüken, P.V.W. Sasikumar, H.-Y. Lee, D. Di Stadio, Y. Chandorkar, M. Rottmar, K. Maniura-Weber, G. Blugan, J. Brugger, Multiscale 2d/3d microshaping and property tuning of polymer-derived sicn ceramics, Journal of the European Ceramic Society 42(5) (2022) 1963-1970.
[74] J. Wang, D. Kober, G. Shao, J.D. Epping, O. Görke, S. Li, A. Gurlo, M.F. Bekheet, Stable anodes for lithium-ion batteries based on tin-containing silicon oxycarbonitride ceramic nanocomposites, Materials Today Energy 26 (2022) 100989.
[75] S. Sarkar, J. Zou, J. Liu, C. Xu, L. An, L. Zhai, Polymer-derived ceramic composite fibers with aligned pristine multiwalled carbon nanotubes, ACS Appl Mater Interfaces 2(4) (2010) 1150-6.
[76] R. Anand, B.B. Nayak, S.K. Behera, Coarsening kinetics of nanostructured zro2 in zr-doped sicn ceramic hybrids, Journal of Alloys and Compounds 811 (2019).
[77] M.P. De Beer, H.L. Van Der Laan, M.A. Cole, R.J. Whelan, M.A. Burns, T.F. Scott, Rapid, continuous additive manufacturing by volumetric polymerization inhibition patterning, Journal of Physics A: Mathematical and Theoretical 52(3) (2019).
[78] D. Yang, Y. Yu, X. Zhao, Y. Song, E. Lopez-Honorato, P. Xiao, D. Lai, Fabrication of silicon carbide (sic) coatings from pyrolysis of polycarbosilane/aluminum, Journal of Inorganic and Oganometallic Polymers and Materials 21 (2011) 534-540.
[79] Y. Li, E. Kroke, R. Riedel, C. Fasel, C. Gervais, F. Babonneau, Thermal cross-linking and pyrolytic conversion of poly(ureamethylvinyl)silazanes to silicon-based ceramics, Applied Organometallic Chemistry 15(10) (2001) 820-832.
[80] R.M. Laine, A. Sellinger, Si-containing ceramic precursors, 2003.
[81] K. Kim, H. Ju, J. Kim, Pyrolysis behavior of polysilazane and polysilazane-coated-boron nitride for high thermal conductive composite, Composites Science and Technology 141 (2017) 1-7.
[82] Y.C. Song, Y. Zhao, C.X. Feng, Y. Lu, Synthesis and pyrolysis of polysilazane as the precursor of si3n4/sic ceramic, JOURNAL OF MATERIALS SCIENCE 29 (1994) 5745-5756.
[83] N.M. Chelliah, H. Singh, R. Raj, M.K. Surappa, Processing, microstructural evolution and strength properties of in-situ magnesium matrix composites containing nano-sized polymer derived sicno particles, Materials Science and Engineering: A 685 (2017) 429-438.
[84] N.M. Chelliah, H. Singh, R. Raj, M.K.K. Surappa, Processing, microstructural evolution and strength properties of in-situ magnesium matrix composites containing nano-sized polymer derived sicno particles, Materials Science and Engineering: A 685(January) (2017) 429-438.
[85] R.M. Laine, F. Babonneau, Preceramic polymer routes to silicon carbide, Chemistry of Materials 5(3) (1993) 260-279.
[86] P. Colombo, A. Martucci, O. Fogato, P. Villoresi, Silicon carbide films by laser pyrolysis of polycarbosilane, Journal of the American Ceramic Society 84(1) (2001) 224-226.
[87] K. Jakubenas, H.L. Marcus, Silicon carbide from laser pyrolysis of polycarbosilane, 1994 (1995) 2263-2266.
[88] J. Liu, Y.L. Qiao, P. Zhang, Y.C. Xue, Z. Cai, Synthesis of sic ceramics from polysilazane by laser pyrolysis, Surface and Coatings Technology 321 (2017) 491-495.

[89] J.C. Pivin, P. Colombo, G.D. Sorarù, Comparison of ion irradiation effects in silicon-based preceramic thin films, Journal of the American Ceramic Society 83(4) (2004) 713-720.
[90] Sudarshan, M.K. Surappa, D. Ahn, R. Raj, Nanoceramic–metal matrix composites by in-situ pyrolysis of organic precursors in a liquid melt, Metallurgical and Materials Transactions A 39 (2008) 3291-3297.
[91] A.K. P, D. Yadav, C.S. Perugu, S.V. Kailas, Influence of particulate reinforcement on microstructure evolution and tensile properties of in-situ polymer derived mmc by friction stir processing, Materials and Design 113 (2017) 99-108.
[92] M. Surappa, D. Ahn, R. Raj, Nanoceramic–metal matrix composites by in-situ pyrolysis of organic precursors in a liquid melt.
[93] A.K. P., R. Raj, S.V. Kailas, A novel in-situ polymer derived nano ceramic mmc by friction stir processing, Materials & Design 85 (2015) 626-634.
[94] E. Castellan, G. Ischia, A. Molinari, R. Raj, A novel in situ method for producing a dispersion of a ceramic phase into copper that remains stable at 0.9t m, Metallurgical and Materials Transactions A 44 (2013) 4734-4742.
[95] E. Castellan, S.V. Kailas, S. Madayi, R. Raj, Low-wear high-friction behavior of copper matrix composites dispersed with an in situ polymer derived ceramic, Journal of Tribology 137 (2015) 024501.
[96] Sudarshan, K. Terauds, A.R. Anilchandra, R. Raj, Polymer-derived in-situ metal matrix composites created by direct injection of a liquid polymer into molten magnesium, Metallurgical and Materials Transactions A: Physical Metallurgy and Materials Science 45 (2013) 551-554.
[97] W. Liu, C. Cao, J. Xu, X. Wang, X. Li, Molten salt assisted solidification nanoprocessing of al-tic nanocomposites, Materials Letters 185 (2016) 392-395.
[98] C. Cao, W. Liu, A. Javadi, H. Ling, X. Li, Scalable manufacturing of 10 nm tic nanoparticles through molten salt reaction, Procedia Manufacturing 10 (2017) 634-640.
[99] A.R. Kennedy, A.E. Karantzalis, The incorporation of ceramic particles in molten aluminum and the relationship to contact angle data, Mater. Sci. Eng. A 264(1-2) (1999) 122-129.
[100] C. Cao, H. Ling, N. Murali, X. Li, In-situ molten salt reaction and incorporation of small (10 nm) tic nanoparticles into al, Materialia 7 (2019).
[101] Y. Birol, Response to thermal exposure of al/k2tif6/c powder blends, Journal of Alloys and Compounds 455(1-2) (2008) 164-167.
[102] Y. Birol, Analysis of the response to thermal exposure of al/k2tif6 powder blends, Journal of Alloys and Compounds 478(1-2) (2009) 265-268.
[103] J. Fjellstedt, A.E.W. Jarfors, On the precipitation of tib2 in aluminum melts from the reaction with kbf4 and k2tif6, Mater. Sci. Eng. A 413 (2005) 527-532.
[104] S. Agrawal, A.K. Ghose, I. Chakrabarty, Effect of rotary electromagnetic stirring during solidification of in-situ al-tib2 composites, Materials and Design 113 (2017) 195-206.
[105] R. Venkatesh, D. Sethi, V. Kolli, B.S. Roy, Experimental investigation of aluminium matrix composite production and joining, Materials Today: Proceedings 18 (2019) 5276-5285.
[106] P. Senthil Kumar, V. Kavimani, K. Soorya Prakash, V. Murali Krishna, G. Shanthos Kumar, Effect of tib2 on the corrosion resistance behavior of in situ al composites, International Journal of Metalcasting 14(1) (2020) 84-91.
[107] Y. Birol, In situ synthesis of al–ticp composites by reacting k2tif6 and particulate graphite in molten aluminium, Journal of Alloys and Compounds 454(1-2) (2008) 110-117.
[108] P. Baumli, J. Sytchev, G. Kaptay, Perfect wettability of carbon by liquid aluminum achieved by a multifunctional flux, Journal of Materials Science 45(19) (2010) 5177-5190.

[109] P. Baumli, J. Sychev, I. Budai, J.T. Szabo, G. Kaptay, Fabrication of carbon fiber reinforced aluminum matrix composites via a titanium-ion containing flux, Composites Part A: Applied Science and Manufacturing 44 (2013) 47-50.
[110] K. Rane, N. Dhokey, On the formation and distribution of in situ synthesized tib2 reinforcements in cast aluminium matrix composites, Journal of Composites Science 2(3) (2018).
[111] X. Wang, A. Jha, R. Brydson, In situ fabrication of al3ti particle reinforced aluminium alloy metal–matrix composites, Materials Science and Engineering: A 364(1-2) (2004) 339-345.
[112] G.-R. Li, H.-M. Wang, Y.-T. Zhao, D.-B. Chen, G. Chen, X.-N. Cheng, Microstructure of in situ al3ti/6351al composites fabricated with electromagnetic stirring and fluxes, Transactions of Nonferrous Metals Society of China 20(4) (2010) 577-583.
[113] Y. Birol, Production of al-b alloy by heating al/kbf4 powder blends, J. Alloys and Compd. 481(1-2) (2009) 195-198.
[114] S. Ma, X. Wang, Mechanical properties and fracture of in-situ al 3 ti particulate reinforced a356 composites, Materials Science and Engineering A 754(March) (2019) 46-56.
[115] G.R. Li, H.M. Wang, Y.T. Zhao, D.B. Chen, G. Chen, X.N. Cheng, Microstructure of in situ al3ti/6351al composites fabricated with electromagnetic stirring and fluxes, Transactions of Nonferrous Metals Society of China (English Edition) 20(4) (2010) 577-583.
[116] C.W. Reese, A. Gladstein, P. Shevchenko, X. Xiao, A.J. Shahani, A.I. Taub, Real-time visualization of particle evolution during reactive flux-assisted processing of aluminum melts, Scripta Materialia 201 (2021).
[117] H. Ding, X. Fan, K. Chu, X. Zhang, X. Liu, The influence of carbon vacancies on the stacking fault energy of tic, Journal of the European Ceramic Society 34(7) (2014) 1893-1897.
[118] L. Tsetseris, S.T. Pantelides, Vacancies, interstitials and their complexes in titanium carbide, Acta Materialia 56(12) (2008) 2864-2871.
[119] X. Tang, R. Salehin, G.B. Thompson, C.R. Weinberger, Statistical study of vacancy diffusion in tic and tac, Physical Review Materials 4(9) (2020).
[120] K.E. Tan, A.M. Bratkovsky, R.M. Harris, A.P. Horsfield, D. Nguyen-Manh, D.G. Pettifor, A.P. Sutton, Carbon vacancies in titanium carbide, Modelling and Simulation in Materials Science and Engineering 5 (1997) 187-198.
[121] W. Sun, H. Ehteshami, P.A. Korzhavyi, Structure and energy of point defects in tic: An *ab initio* study, Physical Review B 91 (2015) 134111.
[122] B.-X. Dong, H.-Y. Yang, F. Qiu, Q. Li, S.-L. Shu, B.-Q. Zhang, Q.-C. Jiang, Design of tic nanoparticles and their morphology manipulating mechanisms by stoichiometric ratios: Experiment and first-principle calculation, Materials & Design 181 (2019).
[123] D. Zhang, H. Liu, L. Sun, F. Bai, Y. Wang, J. Wang, Shape-controlled ticx particles fabricated by combustion synthesis in the cu-ti-c system, Crystals 7(7) (2017).
[124] L. Ceschini, A. Dahle, M. Gupta, A.E.W. Jarfors, S. Jayalakshmi, A. Morri, F. Rotundo, S. Toschi, R.A. Singh, Mechanical behavior of al and mg based nanocomposites, Aluminum and magnesium metal matrix nanocomposites2017, pp. 95-137.
[125] J.B. Ferguson, B.F. Schultz, D. Venugopalan, H.F. Lopez, P.K. Rohatgi, K. Cho, C.-S. Kim, On the superposition of strengthening mechanisms in dispersion strengthened alloys and metal-matrix nanocomposites: Considerations of stress and energy, Metals and Materials International 20(2) (2014) 375-388.
[126] A. Sanaty-Zadeh, Comparison between current models for the strength of particulate-reinforced metal matrix nanocomposites with emphasis on consideration of hall-petch effect, Materials Science and Engineering A 531 (2012) 112-118.

[127] F.A. Mirza, D.L. Chen, A unified model for the prediction of yield strength in particulate reinforced metal matrix nanocomposites, Materials 8 (2015) 5138-5153.
[128] W.S. Miller, F.J. Humphreys, Strengthening mechanisms in particulate metal matrix composites, Scr. Mater. 25(33) (1991).
[129] N. Ramakrishnan, An analytical study on strengthening of particulate reinforced metal matrix composites, Acta Mater 44(69) (1996).
[130] F. Ahmadi, M. Farzin, M. Mandegari, Effect of grain size on ultrasonic softening of pure aluminum, Ultrasonics 63 (2015) 111-7.
[131] Z. Zhang, D.L. Chen, Contribution of orowan strengthening effect in particulate-reinforced metal matrix nanocomposites, Materials Science and Engineering: A 483-484 (2008) 148-152.
[132] P. Shen, Y. Wang, L. Ren, S. Li, Y. Liu, Q. Jiang, Influence of sic surface polarity on the wettability and reactivity in an al/sic system, Applied Surface Science 355 (2015) 930-938.
[133] X.S. Cong, P. Shen, Y. Wang, Q. Jiang, Wetting of polycrystalline sic by molten al and al−si alloys, Applied Surface Science 317 (2014) 140-146.
[134] A.S. Mukasyan, C.E. Shuck, Kinetics of shs reactions: A review, International Journal of Self-Propagating High-Temperature Synthesis 26(3) (2017) 145-165.
[135] J. Nuechterlein, Production of ceramic nanoparticles through self-propagating high-temperature synthesis (shs) and their introduction into a metallic matrix to form metal matrix composites (mmc), Metallurgical and Materials Engineering, Colorado School of Mines, 2013.
[136] Kgaa, 214049 durazane$^{(r)}$ 1800 technical datasheet, EMD Performance Materials, Darmstadt, Germany.
[137] C. Li, J. Wei, M. Chen, X. Guan, X. Yang, Z. Li, C. Ma, X. Ye, Ultralow-temperature fabrication of chromium-free zinc-aluminum coatings based on polysilazane, Materials Chemistry and Physics 278 (2022) 125608.
[138] K. Kim, S. Ryu, J. Kim, Melt-processable aggregated boron nitride particle via polysilazane coating for thermal conductive composite, Ceramics International 43(2) (2017) 2441-2447.
[139] A. Horcher, K. Tangermann-Gerk, W. Krenkel, M. Schmidt, R.K. Bordia, G. Motz, Laser pyrolyzed organosilazane-based al/zro
2
composite coating on stainless steel: Resulting microstructure and mechanical properties, International Journal of Applied Ceramic Technology 19(2) (2021) 856-865.
[140] A. Horcher, K. Tangermann-Gerk, G. Barroso, M. Schmidt, G. Motz, Laser and furnace pyrolyzed organosilazane-based glass/zro2 composite coating system—a comparison, Journal of the European Ceramic Society 40(7) (2020) 2642-2651.
[141] A.H. Tavakoli, R. Campostrini, C. Gervais, F. Babonneau, J. Bill, G.D. Sorarù, A. Navrotsky, J.C. Mauro, Energetics and structure of polymer-derived si-(b-)o-c glasses: Effect of the boron content and pyrolysis temperature, Journal of the American Ceramic Society 97(1) (2014) 303-309.
[142] A.H. Tavakoli, J.A. Golczewski, J. Bill, A. Navrotsky, Effect of boron on the thermodynamic stability of amorphous polymer-derived si(b)cn ceramics, Acta Materialia 60(11) (2012) 4514-4522.
[143] Y.-L. Li, E. Kroke, R. Riedel, C. Fasel, C. Gervais, F. Babonneau, Thermal cross-linking and pyrolytic conversion of poly(ureamethylvinyl)silazanes to silicon-based ceramics, Applied Organometallic Chemistry 15(10) (2001) 820-832.
[144] Starpcs^{tm} smp-10, silicon carbide matrix precursor, Starfire Systems.

[145] Starpcs^{tm} smp-500, polycarbosilane precursor, StarFire Systems.
[146] Starpcs^{tm} smp-730, polycarbosilane precursor, Starfire Systems.
[147] Flexalite safety data sheet, Tethon 3D.
[148] Genesis safety data sheet, Tethond 3D.
[149] A. Qazzazie-Hauser, K. Honnef, T. Hanemann, Crosslinking behavior of uv-cured polyorganosilazane as polymer-derived ceramic precursor in ambient and nitrogen atmosphere, Polymers (Basel) 13(15) (2021) 2424.
[150] N.M. Chelliah, Sudarshan, L. Kraemer, H. Singh, M.K. Surappa, R. Raj, Stress–rupture measurements of cast magnesium strengthened by in-situ production of ceramic particles, Journal of Magnesium and Alloys 5(2) (2017) 225-230.
[151] H.Q. Ly, R. Taylor, R.J. Day, F. Heatley, Conversion of polycarbosilane (pcs) to sic-based ceramic part ii. Pyrolysis and characterisation, JOURNAL OF MATERIALS SCIENCE 36 (2001) 4045– 4057.
[152] H.Q. Ly, R. Taylor, R.J. Day, F. Heatley, Conversion of polycarbosilane (pcs) to sic-based ceramic part 1. Characterisation of pcs and curing products, JOURNAL OF MATERIALS SCIENCE 36 (2001) 4037-4043.
[153] R.M. Laine, A. Sellinger, Si-containing ceramic precursors, in: Z. Rappoport, Y. Apeloig (Eds.), The chemistry of organic silicon compounds, John Wiley & Sons, Ltd.1998, pp. 2245 - 2316.
[154] Ir spectrum table & chart. https://www.sigmaaldrich.com/US/en/technical-documents/technical-article/analytical-chemistry/photometry-and-reflectometry/ir-spectrum-table. 2022).
[155] E. Castellan, G. Ischia, A. Molinari, R. Raj, A novel in situ method for producing a dispersion of a ceramic phase into copper that remains stable at 0.9t m, Metallurgical and Materials Transactions A 44(10) (2013) 4734-4742.
[156] X. Wang, F. Schmidt, D. Hanaor, P.H. Kamm, S. Li, A. Gurlo, Additive manufacturing of ceramics from preceramic polymers: A versatile stereolithographic approach assisted by thiol-ene click chemistry, Additive Manufacturing 27 (2019) 80-90.
[157] D. Yang, Y. Yu, X. Zhao, Y. Song, E. Lopez-Honorato, P. Xiao, D. Lai, Fabrication of silicon carbide (sic) coatings from pyrolysis of polycarbosilane/aluminum, Journal of Inorganic and Organometallic Polymers and Materials 21(3) (2011) 534-540.
[158] M. Lodhe, N. Babu, A. Selvam, M. Balasubramanian, Synthesis and characterization of high ceramic yield polycarbosilane precursor for sic, Journal of Advanced Ceramics 4(4) (2015) 307-311.
[159] P. Hernández-Rodríguez, E. López-Honorato, Polymer derived sic environmental barrier coatings with superwetting properties, Ceramics International 43(14) (2017) 11289-11295.
[160] M. Monthioux, Delverdier, Thermal behavior of (organosilicon) polymerderived ceramics. V: Main facts and trends, Journal of the European Ceramic Society 16 (1995) 721-737.
[161] M.A. El Khakani, M. Chaker, A. Jean, S. Boily, J.C. Kieffer, M.E. O'hern, M.F. Ravet, F. Rousseaux, Hardness and young's modulus of amorphous a-sic thin films determined by nanoindentation and bulge tests, Journal of Materials Research 9(1) (1994) 96-103.
[162] G.M. Renlund, S. Prochazka, R.H. Doremus, Silicon oxycarbide glasses: Part ii. Structure and properties, J. Mater. Res. 6(12) (1991) 2723-2734.
[163] G.M. Renlund, S. Prochazka, R.H. Doremus, Silicon oxycarbide glasses: Part i. Preparation and chemistry, J. Mater. Res. 6(12) (1991) 2716-2722.

[164] R.M. Laine, F. Babonneau, Preceramic polymer routes to silicon carbide, Chemistry of Materials 5(3) (2002) 260-279.
[165] P. Colombo, G. Mera, R. Riedel, G.D. Sorarù, Polymer-derived ceramics: 40 years of research and innovation in advanced ceramics, Journal of the American Ceramic Society (2010) no-no.
[166] E. Bernardo, L. Fiocco, G. Parcianello, E. Storti, P. Colombo, Advanced ceramics from preceramic polymers modified at the nano-scale: A review, Materials (Basel) 7(3) (2014) 1927-1956.
[167] J.V. Ryan, P. Colombo, J.A. Howell, C.G. Pantano, Tribology-structure relationships in silicon oxycarbide thin films, International Journal of Applied Ceramic Technology 7(5) (2009) 675-686.
[168] D.R. Gaskell, Appendices a: Selected thermodynamic and thermochemical data in: R. H.Bedford (Ed.), Introduction to the thermodynamics of materials 4e, Taylor & Francis, New York, NY, 2009, pp. 703-710.
[169] M. H.C, S.V. Kailas, Fabrication of localised aluminium foam by a novel polymeric blowing agent, Materials Characterization 142 (2018) 340-351.
[170] E.V. Bongio, S.L. Lewis, D.R. Welson, W.J. Sherwood, Polymer derived ceramic matrix composites for friction applications, Advances in Applied Ceramics 108(8) (2013) 483-487.
[171] E. Castellan, S.V. Kailas, S. Madayi, R. Raj, Low-wear high-friction behavior of copper matrix composites dispersed with an in situ polymer derived ceramic, Journal of Tribology 137(2) (2015).
[172] A.K. P, D. Yadav, C.S. Perugu, S.V. Kailas, Influence of particulate reinforcement on microstructure evolution and tensile properties of in-situ polymer derived mmc by friction stir processing, Materials & Design 113 (2017) 99-108.
[173] N.M. Chelliah, H. Singh, M.K. Surappa, Microstructural evolution and strengthening behavior in in-situ magnesium matrix composites fabricated by solidification processing, Materials Chemistry and Physics 194 (2017) 65-76.
[174] N.M. Chelliah, P. Pambannan, M.K. Surappa, Effects of processing conditions on solidification characteristics and mechanical properties of in situ magnesium metal matrix composites derived from polysilazane precursor, Journal of Composite Materials 53(26-27) (2019) 3741-3755.
[175] N.M. Chelliah, P. Padaikathan, M.K. Surappa, Deformation mechanisms and texture evolution of in-situ magnesium matrix composites containing polymer derived sicno dispersoids during hot compression, Materials Science and Engineering: A 720 (2018) 49-59.
[176] Sudarshan, K. Terauds, A.R. Anilchandra, R. Raj, Polymer-derived in-situ metal matrix composites created by direct injection of a liquid polymer into molten magnesium, Metallurgical and Materials Transactions A 45(2) (2013) 551-554.
[177] Sudarshan, M.K. Surappa, D. Ahn, R. Raj, Nanoceramic–metal matrix composites by in-situ pyrolysis of organic precursors in a liquid melt, Metallurgical and Materials Transactions A 39(13) (2008) 3291-3297.
[178] Q. Zhang, B.L. Xiao, W.G. Wang, Z.Y. Ma, Reactive mechanism and mechanical properties of in situ composites fabricated from an al–tio2 system by friction stir processing, Acta Materialia 60(20) (2012) 7090-7103.
[179] Q. Zhang, B.L. Xiao, D. Wang, Z.Y. Ma, Formation mechanism of in situ al3ti in al matrix during hot pressing and subsequent friction stir processing, Materials Chemistry and Physics 130(3) (2011) 1109-1117.

[180] R. Yang, Z. Zhang, Y. Zhao, G. Chen, Y. Guo, M. Liu, J. Zhang, Effect of multi-pass friction stir processing on microstructure and mechanical properties of al3ti/a356 composites, Materials Characterization 106 (2015) 62-69.
[181] S. Salunkhe, N. Dilip Raja, R. Naren Shankar, S. Guessasma, V. Naranje, Optimization of friction stir welded aa6061 + sicp metal matrix composite to increase joint tensile strength and reduce defects, International Journal for Simulation and Multidisciplinary Design Optimization 12 (2021).
[182] N. Chawla, C. Andres, J.W. Jones, J.E. Allison, Effect of sic volume fraction and particle size on the fatigue resistance of a 2080 al/sicp composite, Metallurgical and Materials Transactions A 29A (1998) 2843-2854.
[183] J. Liu, X. Huang, K. Zhao, Z. Zhu, X. Zhu, L. An, Effect of reinforcement particle size on quasistatic and dynamic mechanical properties of al-al2o3 composites, Journal of Alloys and Compounds 797 (2019) 1367-1371.
[184] Z. Hu, M. Pozuelo, M. Sokoluk, S. Mathaudhu, C. Roach, X. Li, J.-M. Yang, Micro-mechanical properties of homogeneous- and inhomogeneous-structured pillars in al–tic nanocomposite: An in-situ study, J. Mater. Sci. Eng. A 762 (2019).
[185] W. Zhai, W. Zhou, S.M.L. Nai, Grain refinement and strengthening of 316l stainless steel through addition of tic nanoparticles and selective laser melting, J. Mater. Sci. Eng. A 832 (2022).
[186] A. Wagih, A. Fathy, D. Ibrahim, O. Elkady, M. Hassan, Experimental investigation on strengthening mechanisms in al-sic nanocomposites and 3d fe simulation of vickers indentation, Journal of Alloys and Compounds 752 (2018) 137-147.
[187] J. Qin, G. Chen, B. Wang, N. Hu, F. Han, Z. Du, Formation of in-situ al3ti particles from globular ti powders and al alloy melt under ultrasonic vibration, Journal of Alloys and Compounds 653 (2015) 32-38.
[188] Z. Liu, N. Cheng, Q. Zheng, J. Wu, Q. Han, Z. Huang, J. Xing, Y. Li, Y. Gao, Processing and tensile properties of a356 composites containing in situ small-sized al3ti particulates, J. Mater. Sci. Eng. A 710 (2018) 392-399.
[189] Z.W. Liu, Q. Han, J.G. Li, Formation of small blocky al3ti particles via direct reaction between solid ti powders and liquid al, Metallurgical and Materials Transactions A 43(12) (2012) 4460-4463.
[190] Q. Guo, Y. Han, D. Zhang, Interface-dominated mechanical behavior in advanced metal matrix composites, Nano Mater. Sci. 2 (2020) 66-71.
[191] C.W. Reese, A. Gladstein, P. Shevchenko, X. Xiao, A.J. Shahani, A.I. Taub, Real-time visualization of particle evolution during reactive flux-assisted processing of aluminum melts, Scripta Mater. 201 (2021) 113978.
[192] C.W. Reese, A. Gladstein, J.M. Fedors, V. De Andrade, B. Mishra, A.J. Shahani, A.I. Taub, In situ al-tic composites fabricated by self-propagating high-temperature reaction: Insights on reaction pathways and their microstructural signatures, Metallurgical and Materials Transactions A 51(7) (2020) 3587-3600.
[193] S. Chatterjee, A. Ghosh, A. Basu Mallick, Understanding the evolution of microstructural features in the in-situ intermetallic phase reinforced al/al 3 ti nanocomposite, Materials Today: Proceedings 5(3) (2018) 10118-10130.
[194] I. Anza, M.M. Makhlouf, Synthesis of aluminum-titanium carbide micro and nanocomposites by the rotating impeller in-situ gas–liquid reaction method, Metallurgical and Materials Transactions B 49B (2018) 466-480.

[195] H. Ding, W. Miao, W. Chu, Q. Liu, J. Wang, K. Chu, N. Glandut, C. Li, The reaction pathway of ti-sic system in cu melts, Journal of Alloys and Compounds 818 (2020) 152860.
[196] X. Wang, A. Jha, R. Brydson, In situ fabrication of al3ti particle reinforced aluminium alloy metal–matrix composites, J. Mater. Sci. Eng. A 364(1-2) (2004) 339-345.
[197] V. Auradi, S.A. Kori, Influence of reaction temperature for the manufacturing of al–3ti and al–3b master alloys, Journal of Alloys and Compounds 453(1-2) (2008) 147-156.
[198] N. El-Mahallawy, M.A. Taha, A.E.W. Jarfors, H. Fredriksson, On the reaction between aluminium, k2tif and kbf4, Journal of Alloys and Compounds 292 (1999) 221-229.
[199] M.S. Lee, B.S. Terry, Effects of processing parameters on aluminide morphology in aluminium grain refining master alloys, Materials Science and Technology 7(7) (1991) 608-612.
[200] Y. Birol, Effect of the salt addition practice on the grain refining efficiency of al–ti–b master alloys, Journal of Alloys and Compounds 420(1-2) (2006) 207-212.
[201] H. Ding, X. Liu, L. Yu, G. Zhao, The influence of forming processes on the distribution and morphologies of tic in al–ti–c master alloys, Scripta Materialia 57(7) (2007) 575-578.
[202] P. Baumli, J. Sytchev, G. Kaptay, Perfect wettability of carbon by liquid aluminum achieved by a multifunctional flux, J. Mater. Sci. 45 (2010) 5177-5190.
[203] Y.-H. Cho, J.-M. Lee, S.-H. Kim, Al-tic composites fabricated by a thermally activated reaction process in an al melt using al-ti-c-cuo powder mixtures. Part i: Microstructural evolution and reaction mechanism, Metallurgical and Materials Transactions A 45(12) (2014) 5667-5678.
[204] R. Daudin, S. Terzi, P. Lhuissier, J. Tamayo, M. Scheel, N.H. Babu, D.G. Eskin, L. Salvo, Particle-induced morphological modification of al alloy equiaxed dendrites revealed by sub-second in situ microtomography, Acta Materialia 125 (2017) 303-310.
[205] E. Guo, S. Shuai, D. Kazantsev, S. Karagadde, A.B. Phillion, T. Jing, W. Li, P.D. Lee, The influence of nanoparticles on dendritic grain growth in mg alloys, Acta Materialia 152 (2018) 127-137.
[206] E. Guo, A.B. Phillion, Z. Chen, H. Kang, T. Wang, P.D. Lee, In situ tomographic observation of dendritic growth in mg/al matrix composites, Light metals 20192019, pp. 1561-1567.
[207] J.W. Pegues, M.A. Melia, M.A. Rodriguez, T.F. Babuska, B. Gould, N. Argibay, A. Greco, A.B. Kustas, In situ synchrotron x-ray imaging and mechanical properties characterization of additively manufactured high-entropy alloy composites, Journal of Alloys and Compounds 876 (2021).
[208] S. Li, B. Cai, R. Duan, L. Tang, Z. Song, D. White, O.V. Magdysyuk, M.M. Attallah, Synchrotron characterisation of ultra-fine grain tib2/al-cu composite fabricated by laser powder bed fusion, Acta Metall. Sin. 35(1) (2021) 78-92.
[209] W. Mirihanage, W. Xu, J. Tamayo-Ariztondo, D. Eskin, M. Garcia-Fernandez, P. Srirangam, P. Lee, Synchrotron radiographic studies of ultrasonic melt processing of metal matrix nano composites, Materials Letters 164 (2016) 484-487.
[210] M. Schöbel, G. Requena, G. Fiedler, D. Tolnai, S. Vaucher, H.P. Degischer, Void formation in metal matrix composites by solidification and shrinkage of an alsi7 matrix between densely packed particles, Composites Part A: Applied Science and Manufacturing 66 (2014) 103-108.
[211] P.J. Withers, X-ray nanotomography, Materials Today 10(12) (2007) 26-34.
[212] W.-K. Lee, R. Reininger, W. Loo, R. Gambella, S. O'hara, Y.S. Chu, Z. Zhong, J. Wang, Fxi: A full-field imaging beamline at nsls-ii, Proceedings of SPIE, San Diego, CA, 2015, p. 959209.

[213] Asm alloy phase diagram database, 2022. https://matdata-asminternational-org.proxy.lib.umich.edu/apd/index.aspx.
[214] B.L. Henke, E.M. Gullikson, J.C. Davis, X-ray interactions: Photoabsorption, scattering, transmission, and reflections at e = 50-30000 ev, z = 1-92, Atomic Data and Nuclear Data Tables 54(2) (1993) 181-342.
[215] D. Gursoy, F.D. Carlo, X. Xiao, C. Jacobsen, Tomopy: A framework for the analysis of synchrotron tomographic data, Journal of Synchrotron Radiation 21 (2014) 1188–1193.
[216] Projectjupyter, Jupyterlab documentation, 2018. https://jupyterlab.readthedocs.io/en/stable/index.html.
[217] N.T. Vo, R.C. Atwood, M. Drakopoulos, Superior techniques for eliminating ring artifacts in x-ray micro-tomography, Opt. Express 26(22) (2018) 28396-28412.
[218] B.A. Dowd, G.H. Campbell, R.B. Marr, V.V. Nagarkar, S.V. Tipnis, L. Axe, D.P. Siddons, Developments in synchrotron x-ray computed microtomography at the national synchrotron light source, Proceedings of SPIE, Denver, CO, 1999.
[219] Mathworks, Edge, 2022. https://www.mathworks.com/help/images/ref/edge.html.
[220] Mathworks, Entropyfilt, 2022. https://www.mathworks.com/help/images/ref/entropyfilt.html#d123e95801.
[221] Mathworks, Isosurface, 2022. https://www.mathworks.com/help/matlab/ref/isosurface.html#d123e791380.
[222] D.-J. Kroon, Smooth triangulated mesh, 2022. https://www.mathworks.com/matlabcentral/fileexchange/26710-smooth-triangulated-mesh.
[223] R. Shi, J.M. Meier, A.A. Luo, Controlling particle/metal interactions in metal matrix composites during solidification: The role of melt viscosity and cooling rate, Metall. Mater. Trans. A 50A (2019) 3736-3747.
[224] V. Auradi, S. Amarappa Kori, Effect of processing temperature on the microstructure of al-7ti master alloy and on refinement of α-al dendrites in al-7si alloys Advanced Materials Letters 6(3) (2015) 252-259.
[225] J.A. Dantzig, M. Rappaz, Solidification, 2009.
[226] R.F. Sekerka, Role of instabilities in determination of the shapes of growing crystals, Journal of Crystal Growth 128 (1993) 1-12.
[227] R.F. Sekerka, Theory of crystal growth morphology, in: G. Muller, J.-J. Metois, P. Rudolph (Eds.), Crystal growth - from fundamentals to technology2004.
[228] W. Ding, T. Xia, W. Zhao, Performance comparison of al–ti master alloys with different microstructures in grain refinement of commercial purity aluminum, Materials 7 (2014) 3663-3676.
[229] D.H.S. John, L.M. Hogan, Metallography and growth crystallography of ah ti in al-ti alloys up to 5 wt% ti, J. Cryst. Growth 46 (1979) 387-398.
[230] L. Arnberg, L. Bäckerud, H. Klang, Intermetallic particles in al–ti–b–type master alloys for grain refinement of aluminium, Metals Technology 9(1) (1982) 7-13.
[231] M. Yousefi, H. Doostmohammadi, R. Raiszadeh, The effect of melt composition and cooling rate on al3ti morphology in al-al3ti composite, Advances in Metallurgical Prosses and Materials, Ukraine, Lviv, 2018.
[232] J. Zhao, T. Wang, J. Chen, L. Fu, J. He, Effect of cooling rate on morphology of tial3 particles in al-4ti master alloy, Mater. 10(3) (2017).
[233] R. Ghomashchi, The evolution of altisi intermetallic phases in ti-added a356 al–si alloy, Journal of Alloys and Compounds 537 (2012) 255-260.

[234] N.W. Blake, Nucleation in aluminium melts, Metallurgical Engineering, Queen's University, Ontario, Canada, 1982.
[235] A. Majumdar, B.C. Muddle, Microstructure in rapidly solidified a1-ti alloys, Journal of Materials Science and Engineering: A 169 (1993) 135-147.
[236] K.B. Hyde, A.F. Norman, P.B. Prangnell, The effect of cooling rate on the morphology of primary al3sc intermetallic particles in al–sc alloys, Acta Materialia 49 (2001) 1327-1337.
[237] K. Yan, Z.W. Chen, Y.N. Zhao, C.C. Ren, W.J. Lu, A.W. Aldeen, Morphological characteristics of al3sc particles and crystallographic orientation relationships of al3sc/al interface in cast al-sc alloy, Journal of Alloys and Compounds 861 (2021).
[238] J. Zhao, J. He, Q. Tang, T. Wang, J. Chen, Grain refinement efficiency in commercial-purity aluminum influenced by the addition of al-4ti master alloys with varying tial(3) particles, Mater. 9(11) (2016).
[239] V.V. Podolinsky, Non-reciprocal heterogeneous nucleation in eutectic systems, Journal of Crystal Growth 98 (1989) 838-842.
[240] Y. Cui, D.J.M. King, A.P. Horsfield, C.M. Gourlay, Solidification orientation relationships between al3ti and tib2, Acta Materialia 186 (2020) 149-161.
[241] F. Wang, D. Eskin, J. Mi, T. Connolley, J. Lindsay, M. Mounib, A refining mechanism of primary al3ti intermetallic particles by ultrasonic treatment in the liquid state, Acta Materialia 116 (2016) 354-363.
[242] H. Sato, Y. Watanabe, Three-dimensional microstructural analysis of fragmentation behavior of platelet al3ti particles in al-al3ti composite deformed by equal-channel angular pressing, Materials Characterization 144 (2018) 305-315.
[243] M. Yamaguchi, Y. Umakoshi, T. Yamane, Plastic deformation of the intermetallic compound al3ti, Philosophical Magazine A 55(3) (1987) 301-315.
[244] R.M. German, P. Suri, S.J. Park, Review: Liquid phase sintering, Journal of Materials Science 44(1) (2009) 1-39.
[245] J.W. Cahn, J.E. Taylor, A unified approach to motion of grain boundaries, relative tangential translation along grain boundaries, and grain rotation, Acta Materialia 52(16) (2004) 4887-4898.
[246] M. Ebner, F. Marone, M. Stampanoni, V. Wood, Visualization and quantification of electrochemical and mechanical degradation in li ion batteries, Science 342(6159) (2013) 716-720.
[247] B.X. Dong, F. Qiu, Q. Li, S.L. Shu, H.Y. Yang, Q.C. Jiang, The synthesis, structure, morphology characterizations and evolution mechanisms of nanosized titanium carbides and their further applications, Nanomaterials (Basel) 9(8) (2019).
[248] S.A. Reavley, A.L. Greer, Athermal heterogeneous nucleation of freezing: Numerical modelling for polygonal and polyhedral substrates, Philosophical Magazine 88(4) (2008) 561-579.
[249] A.L. Greer, A.M. Bunn, A. Tronche, P.V. Evans, D.J. Bristow, Modelling of inoculation of metallic melts: Application to grain refinement of aluminium by al±ti±b, Acta Materialia 48 (2000) 2823-2835.
[250] T. Fujinaga, Y. Shibuta, Molecular dynamics simulation of athermal heterogeneous nucleation of solidification, Computational Materials Science 164 (2019) 74-81.
[251] D.C. Dunand, Reactive synthesis of aluminide intermetallics, Materials and Manufacturing Processes 10(3) (1995) 373-403.

[252] D. Wearing, A.P. Horsfield, W. Xu, P.D. Lee, Which wets tib2 inoculant particles: Al or al3ti?, J. Alloys Compd. 664 (2016) 460-468.
[253] Pdf card no.: 04-007-1546, in: P.I.X.-r.p.d. software (Ed.) Rigaku, 2022.
[254] L. Yu, X. Liu, Ti transition zone on the interface between tic and aluminum melt and its influence on melt viscosity, Journal of Materials Processing Technology 182(1-3) (2007) 519-524.
[255] S. Agrawal, A.K. Ghose, I. Chakrabarty, Effect of rotary electromagnetic stirring during solidification of in-situ al-tib2 composites, Materials & Design 113 (2017) 195-206.
[256] P.S. Kumar, P.S. Chithirai, D.A. Prabu, G.S. Prakash, V.M. Krishna, J.Y. Mohammed, Analyzing the cooling rate and its effect on distribution of pattern and size of the titanium diboride particles forme, Advances in Materials Science and Engineering 2021 (2021).
[257] R. Bauri, Synthesis of al-tic in situ composites: Effect of processing temperature and ti:C ratio, Transactions of the Indian Institute of Metals 62(4-5) (2009) 391-395.
[258] Z. Liu, N. Cheng, Q. Zheng, J. Wu, Q. Han, Z. Huang, J. Xing, Y. Li, Y. Gao, Processing and tensile properties of a356 composites containing in situ small-sized al3ti particulates, Materials Science and Engineering: A 710 (2018) 392-399.
[259] R. Gupta, G.P. Chaudhari, B.S.S. Daniel, Effect of in-situ formed al3ti particles on the microstructure and mechanical properties of 6061 al alloy, IOP Conference Series: Materials Science and Engineering 330 (2018).
[260] Z. Liu, M. Rakita, X. Wang, W. Xu, Q. Han, In situ formed al3ti particles in al alloy matrix and their effects on the microstructure and mechanical properties of 7075 alloy, Journal of Materials Research 29(12) (2014) 1354-1361.
[261] A.D. Prokopets, P.M. Bazhin, A.S. Konstantinov, A.P. Chizhikov, P.A. Stolin, Structure and mechanical characteristics of a laminated ti3alc2 max phase-based composite material prepared by a free self-propagating high-temperature synthesis compression method, Inorganic Materials 57(9) (2021) 937-941.
[262] G. Liu, Y. Li, L. Fan, M. Nath, Y. Xu, J. Liu, Formation mechanism of ti3alc2 in tio2–al–c/tic systems at high temperatures, Ceramics International 48(2) (2022) 2614-2624.
[263] S.-B. Li, J.-X. Xie, L.-T. Zhang, L.-F. Cheng, In situ synthesis of ti3sic2/sic composite by displacement reaction of si and tic, Materials Science and Engineering: A 381(1-2) (2004) 51-56.
[264] M. Akhlaghi, S.A. Tayebifard, E. Salahi, M. Shahedi Asl, G. Schmidt, Self-propagating high-temperature synthesis of ti3alc2 max phase from mechanically-activated ti/al/graphite powder mixture, Ceramics International 44(8) (2018) 9671-9678.
[265] Q. Tan, W. Zhuang, M. Attia, R. Djugum, M. Zhang, Recent progress in additive manufacturing of bulk max phase components: A review, Journal of Materials Science & Technology 131 (2022) 30-47.
[266] M. Dahlqvist, B. Alling, J. Rosén, Stability trends ofmaxphases from first principles, Physical Review B 81(22) (2010).
[267] A. Hendaoui, D. Vrel, A. Amara, P. Langlois, M. Andasmas, M. Guerioune, Synthesis of high-purity polycrystalline max phases in ti–al–c system through mechanically activated self-propagating high-temperature synthesis, Journal of the European Ceramic Society 30(4) (2010) 1049-1057.
[268] S. Hashimoto, N. Nishina, K. Hirao, Y. Zhou, H. Hyuga, S. Honda, Y. Iwamoto, Formation mechanism of ti2alc under the self-propagating high-temperature synthesis (shs) mode, Materials Research Bulletin 47(5) (2012) 1164-1168.
[269] P. Perrot, Aluminium – silicon – titanium, Landolt-börnstein.

[270] S. Ma, Y. Wang, X. Wang, The in-situ formation of al3ti reinforcing particulates in an al-7wt%si alloy and their effects on mechanical properties, Journal of Alloys and Compounds 792 (2019) 365-374.
[271] X.G. Chen, M. Fortier, Tialsi intermetallic formation and its impact on the casting processing in al–si alloys, Journal of Materials Processing Technology 210(13) (2010) 1780-1786.
[272] S. Ma, N. Li, C. Zhang, X. Wang, Evolution of intermetallic phases in an al–si–ti alloy during solution treatment, Journal of Alloys and Compounds 831 (2020).
[273] S. Ma, X. Wang, Mechanical properties and fracture of in-situ al3ti particulate reinforced a356 composites, Materials Science and Engineering: A 754 (2019) 46-56.
[274] P. Eckerlin, H. Kandler, 4.1 intermetallic phases, in: K.-H. Hellwege, A.M. Hellwege (Eds.), Structure data of elements and intermetallic phases, Springer Berlin, Heidelberg1971.
[275] J.C. Zhao, M.R. Jackson, L.A. Peluso, Mapping of the ti-si-al phase diagram using a diffusion multiple, Journal of Phase Equilibria and Diffusion (2003).
[276] P. Villars, Tisi2 crystal structure, Springer, Heidelberg, 2016.
[277] C. Reese, In situ metal matrix nanocomposites: Towards understanding formation mechanisms and microstructural control, Materials Science and Engineering, University of Michigan, 2020.
[278] Tic (mp-631), the Materials Project, 2021.
[279] Ti3sic2 (mp-5659), the Materials Project, 2021.
[280] Y. Tao, J.J. Derby, The engulfment of a precipitated particle in a saturated melt during solidification, Journal of Crystal Growth 577 (2022).
[281] R. Shi, J.M. Meier, A.A. Luo, Controlling particle/metal interactions in metal matrix composites during solidification: The role of melt viscosity and cooling rate, Metallurgical and Materials Transactions A 50(8) (2019) 3736-3747.
[282] J.Q. Xu, L.Y. Chen, H. Choi, X.C. Li, Theoretical study and pathways for nanoparticle capture during solidification of metal melt, J Phys Condens Matter 24(25) (2012) 255304.
[283] Q. Liu, F.G. Qi, X.L.Wang, H.M. Ding, Y. Shi, The interaction of stacking faults and the doping of si in tic, journal of ceramic science and technology 8(4) (2017) 493-498.
[284] S.-B. Li, W.-H. Xiang, H.-X. Zhai, Y. Zhou, Formation of tic hexagonal platelets and their growth mechanism, Powder Technology 185(1) (2008) 49-53.
[285] R. Yu, L.L. He, H.Q. Ye, Effects of si and al on twin boundary energy of tic, Acta Materialia 51(9) (2003) 2477-2484.
[286] R. Yu, Q. Zhan, L.L. He, Y.C. Zhou, H.Q. Ye, Si-induced twinning of tic and formation of ti3sic2 platelets, acta Mater 50 (2002) 4127-4135.
[287] H.M. Ding, T.J. Ci, K.Y. Chu, J.F. Wang, First-principles study of doping and distribution of si in tic, Materials Science-Poland 31(2) (2013) 259-263.
[288] H.-M. Ding, X.-F. Liu, Influence of si on stability of tic in al melts, Transactions of Nonferrous Metals Society of China 21(7) (2011) 1465-1472.
[289] H. Ding, K. Chu, J. Wang, Simulation study of influence of al, si and b on the growth of tic, Advanced Materials Letters 2(6) (2011) 425-428.
[290] Y. Zhou, Z. Sun, Crystallographic relations between ti3sic2 and tic, Materials Research Innovations 3(5) (2000) 286-291.
[291] Tisi2 (mp-2582), the Materials Project, 2021.
[292] Tial3 (mp-542915), the Materials Project, 2021.

[293] Q. Luo, Q. Li, J.-Y. Zhang, S.-L. Chen, K.-C. Chou, Experimental investigation and thermodynamic calculation of the al–si–ti system in al-rich corner, Journal of Alloys and Compounds 602 (2014) 58-65.
[294] N. Saheb, T. Laoui, A.R. Daud, R. Yahaya, S. Radiman, Microstructure and hardness behaviours of ti-containing al-si alloys, Philosophical Magazine A 82(4) (2002) 803-814.
[295] W.C. Oliver, G.M. Pharr, An improved technique for determining hardness and elastic modulus using load and displacement sensing indentation experiments, J. Mater. Res. 7(6) (1992) 1564-1583.
[296] G. Frommeyer, R. Rosenkranz, Structures and properties of the refractory silicides ti5si3 and tisi2 and ti-si-(al) eutectic alloys, in: O.N. Senko (Ed.), Metallic materials with high structural efficiency, Kluwer Academic Publishers, Netherlands, 2004, pp. 287-308.
[297] Z. Lu, N. Wei, P. Li, C. Guo, F. Jiang, Microstructure and mechanical properties of intermetallic al3ti alloy with residual aluminum, Materials & Design 110 (2016) 466-474.
[298] P.S. Mohanty, J.E. Gruzleski, Grain refinement mechanisms of hypoeutectic al-si alloys, Acta Mater 44(9) (1996) 3749-3760.
[299] D.H.S. John, L.M. Hogan, Thermal stability in the ai-ai,ti system, JOURNAL OF MATERIALS SCIENCE 15 (1980) 2369-2375.
[300] P.A. Korzhavyi, L.V. Pourovskii, H.W. Hugosson, A.V. Ruban, B. Johansson, Ab initio study of phase equilibria in tic(x), Phys Rev Lett 88(1) (2002) 015505.
[301] V.H. López, A. Scoles, A.R. Kennedy, The thermal stability of tic particles in an al7wt.%si alloy, Materials Science and Engineering: A 356(1-2) (2003) 316-325.
[302] A. Tronche, M. Vandyoussefi, A.L. Greer, Instability of tic particles in aluminium melts inoculated with an al-ti-c grain refiner, Materials Science and Technology 18(10) (2013) 1072-1078.
[303] G. Kaptay, Interfacial criterion of spontaneous and forced engulfment of reinforcing particles by an advancing solid/liquid interface, Metall. Mater. Trans. A 32A (2001) 993-1005.
[304] E.M. Agaliotis, C.E. Schvezov, M.R. Rosenberger, A.E. Ares, A numerical model study of the effect of interface shape on particle pushing, Journal of Crystal Growth 354(1) (2012) 49-56.
[305] Á. Borsik, K.K. Kelemen, G. Kaptay, A dynamic model of ceramic particle-solidification front interaction, Materials Science Forum 414-415 (2003) 371-376.
[306] Y. Tao, A. Yeckel, J.J. Derby, Steady-state and dynamic models for particle engulfment during solidification, Journal of Computational Physics 315 (2016) 238-263.
[307] G. Wilde, J.H. Perepezko, Experimental study of particle incorporation during dendritic solidification, Materials science and Engineering A 283 (2000) 25-37.
[308] J.B. Ferguson, G. Kaptay, B.F. Schultz, P.K. Rohatgi, K. Cho, C.-S. Kim, Brownian motion effects on particle pushing and engulfment during solidification in metal-matrix composites, Metallurgical and Materials Transactions A 45(10) (2014) 4635-4645.
[309] I.B. Ozsoy, G. Li, H. Choi, H. Zhao, Shape effects on nanoparticle engulfment for metal matrix nanocomposites, Journal of Crystal Growth 422 (2015) 62-68.
[310] J.K. Kim, P.K. Rohatgi, The effect of the diffusion of solute between the particle and the interface on the particle pushing phenomena, Acta Mater 46 (19978) 1115-1123.
[311] J.C.T. Kao, A.A. Golovin, S.H. Davis, Particle capture in binary solidification, Journal of Fluid Mechanics 625 (2009) 299-320.
[312] Y. Ma, L. Zheng, Directional solidification of metal matrix particulate composite materials, ASME Summer Heat Transfer Conference, San Francisco, CA, 2005.

[313] J.W. Garvin, H.S. Udaykumar, Particle–solidification front dynamics using a fully coupled approach, part i: Methodology, Journal of Crystal Growth 252(1-3) (2003) 451-466.
[314] J.W. Garvin, H.S. Udaykumar, Particle-solidification front dynamics using a fully coupled approach, part ii: Comparison of drag expressions, Journal of Crystal Growth 252(1-3) (2003) 467-479.
[315] T.E. Quested, A.L. Greer, The effect of the size distribution of inoculant particles on as-cast grain size in aluminium alloys, Acta Materialia 52(13) (2004) 3859-3868.
[316] Y. Altman, Export_fig, 2022. https://www.mathworks.com/matlabcentral/fileexchange/23629-export_fig.